EFFECTIVE ELASTIC PROPERTIES OF CRACKED SOLIDS

Mark Kachanov

Department of Mechanical Engineering, Tufts University
Medford, MA 02155, U.S.A.

ABSTRACT

The classical problem of effective elastic properties of cracked solids is critically reviewed. The predictions of the existing schemes are directly checked by computer experiments on a large number of sample arrays of interacting cracks. The main finding is that the approximation of non-interacting cracks (the simplest one) actually remains accurate at high crack densities and strong interactions. The underlying reason is that the competing interaction effects of shielding and amplification cancel each other (provided the mutual positions of cracks are random).

INTRODUCTION

This paper is a brief summary of the work presented in detail in [1,2].

The theory of effective elastic properties of cracked solids predicts degradation of stiffness, development of anisotropy, changes in wavespeeds caused by microcracking. Therefore, it is of obvious interest for solid mechanics, materials science, geophysics; it also constitutes a theoretical basis of various NDE techniques.

Most of the approaches to this problem have roots in the effective media theories of physics. For example, the approximation of *effective matrix* (a self-consistent scheme, in terminology of the mechanics of solids with inhomogeneities), in which a representative inhomogeneity is placed into the effective matrix, was first used in the problems of electrostatics in the XIX-th century. The method of *effective field*, and its simplest version - Mori-Tanaka's method - in which a representative inhomogeneity is embedded into the effective stress field, was first developed in 1940's - 1950's in connection with wave propagation problems.

At the same time, cracks constitute a distinctly special kind of inhomogeneities: they occupy no volume; stress fields generated by them are quite complex and have strong orientational dependence. As a result, cracked solids have many special features: the choice of crack density parameter is non-trivial; the effective properties are, generally, anisotropic; the approximation of non-interacting cracks has a wider than expected range of applicability. Many of the approximate methods, used in the mechanics of general two phase materials, degenerate and cannot be applied to a cracked solid. For example, bounds for the effective moduli, as a rule, cannot be established; Mori-Tanaka's method yields predictions coinciding with the approximation of non-interacting cracks.

Several approximate schemes for cracked solids have been suggested in literature. Their predictions are substantially different. A researcher or an engineer, trying to *use* the theory, may be confused by the choice of several models, yielding different results.

The present work attempts to introduce some clarity into this problem. We briefly review the simplest approach to the problem - the approximation of non-interacting cracks (developed as early as 1960, by Bristow[3]). We then present the results of extensive computer experiments, in which the problem was directly solved for a large number of sample arrays of cracks. The main finding is that the approximation of non-interacting cracks (the simplest one) actually remains accurate at high crack densities and strong interactions. The underlying reason is that the competing interaction effects of shielding and amplification cancel each other (provided the mutual positions of cracks are random).

THE APPROXIMATION OF NON-INTERACTING CRACKS

This simplest approximation, known since 1960, is briefly reviewed here.

In the assumption of non-interacting cracks (in the *isotropic* matrix material) the effective moduli can be found exactly, for an arbitrary crack orientation statistics, in both *2-D* and *3-D*. It is the simplest (and the only non-controversial) approximation to the problem; at the same time, it has a wider than expected range of applicability (see the results presented below). It is often called the approximation of small crack density (in fact, the two names are usually used as synonyms). We refrain, however, from using this term, since *these two assumptions are generally not equivalent* [1,2].

In the approximation of non-interacting cracks, each crack is regarded as an *isolated* one: it is embedded into the externally applied stress field σ and does not experience any influence of other cracks. Then the average crack opening displacement of each crack (COD) $\langle \mathbf{b} \rangle$ for each crack is expressed, in a simple way, in terms of $\mathbf{n}\cdot\sigma$ where $\mathbf{n}$ is a unit normal to the crack. Mutual positions of cracks do not matter in this approximation, hence averaging over a crack array is reduced to summation over orientations. Since the change in compliance $\Delta\mathbf{M}$ due to cracks is a sum of the isolated cracks' contributions, *the compliance is linear in crack density parameter*. Elastic *stiffnesses*, obtained by inversion of compliances, will, of course, be non-linear functions of the crack density, of the form $(1 + C\rho)^{-1}$. Linearization of this form corresponds to the assumption of small crack density. If, however, this form is left as it is, then, as seen below, the results remain accurate at high crack densities.

The problem of effective elastic moduli in the approximation of non-interacting cracks was first solved, for randomly oriented cracks, in both *2-D* and *3-D*, by Bristow (1960).

Since averaging is reduced simply to integration over orientations, such calculations are easily repeated for *an arbitrary* (non-random) *orientational distribution*. Such calculations were done by a number of authors, see [1,2] for a review. For the arbitrary orientational distribution of cracks, the results can be written, in the most general form, in terms of the *crack density tensor* α (introduced by Vakulenko and Kachanov,1971, Kachanov,1972, and, in the corrected and most general form, by Kachanov,1980; see reviews [1,2] for references):

$$\alpha = \frac{1}{A}\sum l^{(i)2}\,\mathbf{n}^i\mathbf{n}^i \qquad \text{(rectilinear cracks of lengths } 2l^i, A \text{ is the representative area)} \qquad (1)$$

The use of the crack density tensor yields, in a unified way, results for any orientational distribution of cracks, without averaging over orientations. It also establishes the symmetry of the effective properties: since α is a symmetric second rank tensor and it enters the elastic potential through a simultaneous invariant with the stress tensor, the effective properties are always *orthotropic* (rectangular symmetry), with the axes of orthotropy coinciding with the principal axes of α. Moreover, the orthotropy is of a special, simplified type [1,2]. This fact is exact in 2-D and approximate (with good accuracy) in *3-D*.

In the simplest cases of *randomly oriented* cracks (isotropic effective properties) and *parallel* cracks (transversely isotropic effective properties) the results, for a *2-D* solid, are as follows.

$$E = E_0(1 + \pi\rho)^{-1}; \qquad \nu = \nu_0(1 + \pi\rho)^{-1} \quad \text{(random orientations)} \qquad (2)$$

$$E_1 = E_0(1+2\pi\rho)^{-1}; \qquad G = G_0[1+(2\pi G_0/E_0)\,\rho\,]^{-1} \quad \text{(parallel cracks)} \qquad (3)$$

where E_0, G_0 and ν_0 denote the moduli of the matrix without cracks (Young's modulus, shear modulus and Poisson's ratio, respectively), and ρ is the conventional scalar crack density parameter introduced by Bristow [3]:

$$\rho = \frac{1}{A}\sum l^{(i)2} \qquad (4)$$

Note that ρ is the linear invariant of the crack density tensor α.

In the *3-D* case, the analysis is similar; a complicating factor is that the orthotropy of the effective properties holds only approximately, although with good accuracy [1,2].

The fact of orthotropy allows one to establish a "natural" coordinate system - principal axes of α - in which the matrix of elastic moduli has its simplest form (orthotropic in *2-D* and approximately orthotropic in *3-D*).

The effect of dimensionality should be mentioned: comparison of the stiffness reduction due to cracks in*2-D* and and *3-D* shows that, at the same crack density, the reduction is *substantially weaker in 3-D*.

ANALYSIS OF CRACK INTERACTIONS

Solutions for *deterministic* arrays of arbitrary geometry, in both *2-D* and *3-D*, can be produced, by relatively simple means and with good accuracy, using the method of analysis of crack interactions developed by Kachanov in 1985, 1987 (see [1,2] for details). This method is briefly outlined below in the *2-D* version

The problem of a linear elastic solid with N cracks subjected to stress σ at infinity is equivalent to the problem with crack faces loaded by tractions $\mathbf{n}^i \cdot \sigma$ ($i = 1,...,N$) and stresses vanishing at infinity. The latter problem can be represented as a superposition of N sub-problems, each containing only *one* crack, but loaded by *unknown* tractions, comprising, in addition to the σ- induced traction, extra tractions accounting for interactions (to be found). Thus, traction $\mathbf{t}^i$ in the i-th sub-problem is a sum of the σ -induced traction $\mathbf{n}^i \cdot \sigma$ and tractions induced by the other cracks in the remaining sub-problems along the line l^i

$$\mathbf{t}^i(\xi^i) = \mathbf{n}^i \cdot [\sigma + \sum_{j \neq i} \sigma^j(\xi^i)] \equiv \mathbf{t}^{i\,(o)} + \Delta\mathbf{t}^i(\xi^i) \qquad (5)$$

where ξ^i is a current point on l^i and σ^j is the j-th crack-generated stress.

The key simplifying assumption of our method is that σ^j is taken as generated by a *uniform average* traction $\langle \mathbf{t}^j \rangle$, yet unknown; the impact on the i-th crack of traction non-uniformities $\mathbf{t}^j - \langle \mathbf{t}^j \rangle$ along the j-th crack is neglected. Decomposing the average $\langle \mathbf{t}^j \rangle$ into a sum of normal and tangential averages, $\langle p^j \rangle$ and $\langle \tau^j \rangle$, we have

$$\mathbf{t}^i(\xi^i) = \mathbf{n}^i \cdot \sigma + \mathbf{n}^i \cdot \sum_{j \neq i} [\langle p^j \rangle \sigma_n^j(\xi^i) + \langle \tau^j \rangle \sigma_\tau^j(\xi^i)] \qquad (6)$$

where σ_n^j and σ_τ^j are the "standard" stress fields, generated (in an infinite solid) by a single j-th crack loaded by uniform tractions of unit intensity, normal and shear, correspondingly. These fields (expressed in elementary functions) are available in fracture mechanics literature.

The unknown quantities in (6) are the average tractions $\langle \mathbf{t}^j \rangle$ on cracks. They are found by averaging (6) along the i-th crack line and thus interrelating them by a system of N vectorial ($2N$ scalar) linear algebraic equations

$$\langle \mathbf{t}^i \rangle = \mathbf{n}^i \cdot \sigma + \sum_{j=1}^{N} (\Lambda^{(ji)} - \delta^{ji}\,\mathbf{I}) \cdot \langle \mathbf{t}^j \rangle \qquad (7)$$

where δ^{ji} is Kronecker's delta and the (tensorial) *transmission* Λ *- factors* characterize transmission of the average tractions from one crack onto another ($\Lambda^{(ji)} \cdot \langle \mathbf{t}^j \rangle$ is the average traction induced on a line l^i in a continuous material by the j-th crack loaded by a uniform traction $\langle \mathbf{t}^j \rangle$). The Λ - factors are expressed in terms of line integrals of elementary functions and are easily calculated.

Solving (7) for average tractions, one obtains:

$$\langle \mathbf{t}^i \rangle = \sum_{j=1}^{N} \Omega^{(ji)} \cdot \langle \mathbf{t}^j \rangle = \sum_{j=1}^{N} \Omega^{(ji)} \mathbf{n}^j : \sigma \qquad (8)$$

where $\Omega^{(ji)} = (2\delta^{ji}\mathbf{I} - \Lambda^{(ji)})^{-1}$. The case of non-interacting cracks is recovered by assuming $\Lambda^{(ji)} = \delta^{ji}\mathbf{I}$; then $\mathbf{t}^i = \mathbf{n}^i \cdot \sigma$.

Finding the average displacement discontinuity $\langle \mathbf{b}^i \rangle$ as approximately proportional to the average traction $\langle \mathbf{t}^i \rangle$ (Kachanov, 1987, see [1,2] for details) we obtain *an explicit expression for the effective compliancet ensor:*

$$\mathbf{M} = \mathbf{M}^0 + (2\pi/A\,E_o') \sum_{i,j=1}^{N} l^{(i)2}\, \Omega_{\{}^{(ij)} \mathbf{n}^i \mathbf{n}^j{}_{\}} \qquad (9)$$

where $\mathbf{M}^0$ is the compliance of the material without cracks and subscript braces denote all the appropriate symmetrizations (with respect to $p \leftrightarrow q$, $r \leftrightarrow s$, and $pq \leftrightarrow rs$ for M_{pqrs}). It incorporates information not only on the crack orientations and sizes, but, also, on their *mutual positions* (all these factors are reflected in Λ's, and, thus, in Ω's).

The method yields results for any given arrangements of cracks. Such results constitute direct computer experiments on sample arrays and can be used to verify various approximate schemes. The method is accurate up to quite close spacings between cracks so that the results are accurate up to high crack densities (as confirmed by smallness of corrections provided by the alternating technique).

COMPUTER EXPERIMENTS

Sample *2-D* crack arrays contained 25 cracks and were generated with the help of random number generator, as realizations of certain crack statistics.

Two *orientation statistics* were assumed: randomly oriented cracks and parallel cracks; for each of them, six crack densities were assumed: $\rho = 0.10$; 0.15; 0.20; 0.25; 0.30 and 0.35 (in *2-D*, the densities of 0.25-0.35 can be considered as quite high).

Fifteen sample arrays were considered for each density.

Locations of cracks within the representative area were random, i.e. positions of crack centers were uncorrelated. For *parallel* cracks, generation of such arrays was straightforward. For *randomly* oriented cracks, crack intersections had to be avoided; this was achieved by generating cracks successively and discarding the newly generated one if it intersects the already existing cracks and generating it again. Although such procedure, strictly speaking, violates the condition that crack centers are uncorrelated, we assume that it does not create errors of a *systematic* sign.

The sample arrays usually contained several cracks with spacings between them much smaller than the crack sizes. To ensure the accuracy of the results at such small spacings, the method outlined above was supplemented by the *alternating technique* (stress "feedbacks"), until the three digits accuracy for the effective moduli was reached. It actually produced only an insignificant correction (smaller than 3-4%) of the method's results, confirming the accuracy of the method.In order to limit the number of iterations in the alternating technique, the spacings between cracks were not allowed to be overly small. Namely, in the case of randomly oriented cracks, they were not smaller than 0.02 of the crack length; in the case of parallel cracks, they were not smaller than 0.15 of the crack length for those crack pairs that had a significant "overlap", and not smaller than 0.02 of the crack length otherwise.

In the case of randomly oriented cracks, each array was examined for *isotropy*: the effective Young's modulus was calculated in two perpendicular directions and only those arrays were kept for which the difference between these two moduli was smaller than 2%; the Young's modulus was then taken as the average over these two values. (Note that preferential orientations causing up to 5-7% variation of E with direction are usually not discernible by a "naked eye").

Fig.1 shows some of the generated arrays.

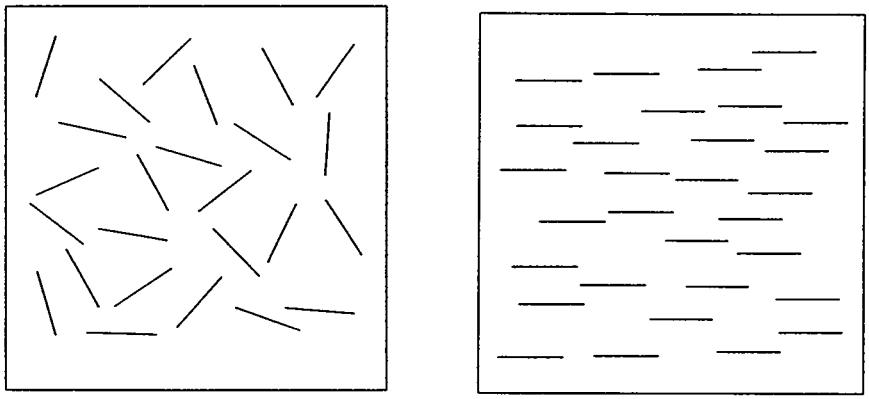

FIG.1. Two of the crack arrays examined (randomly oriented, $\rho = 0.25$ and parallel, $\rho = 0.30$).

The representative area A is assumed to constitute a part of a statistically homogeneous field of cracks (extending all the way to the external boundary) and stresses at the boundary Γ of A are assumed constant and equal to the remotely applied ones. This assumption is rigorously correct for non-interacting cracks, when cracks inside A do not experience any influence of those outside A. For *interacting* cracks, stresses fluctuate along Γ. The errors due to the mentioned assumption depend on the size of the sample. They cause *scatter* of results from one realization of the crack field statistics to another, but are not expected to produce errors of a *systematic* sign. Figs. 2 and 3 show that the scatter is relatively small.

RESULTS

Figs.2 and 3 show results for the Young's modulus for randomly oriented and parallel arrays. Vertical bars show scatter of the results from one sample to another.

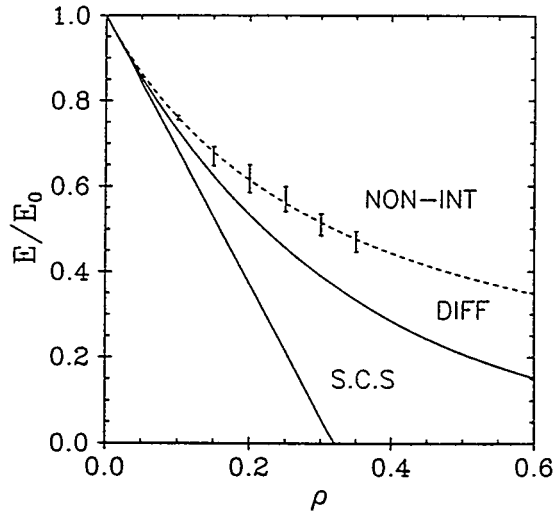

FIG.2. Effective Young's modulus, randomly oriented cracks: results for sample arrays vs predictions of the approximation of non-interacting cracks, self-consistent and differential schemes.

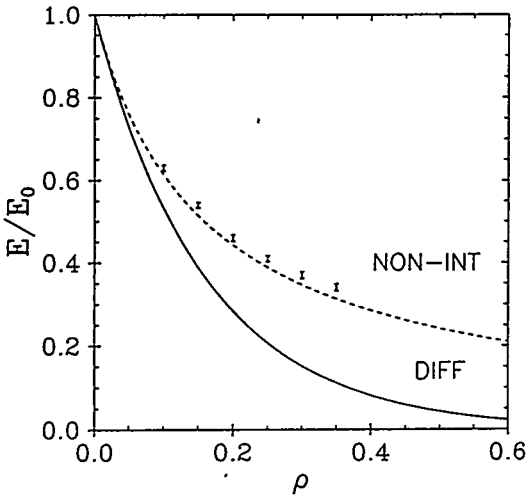

FIG.3. Effective Young's modulus, parallel cracks: results for sample arrays vs the approximation of non-interacting cracks and the differential scheme.

For *randomly oriented* cracks, the approximation of non-interacting cracks provides surprisingly good results, well into the domain of strong interactions where this approximation is usually considered inapplicable.

For *parallel* cracks, the approximation of non-interacting cracks still provides good results. However, there is a slight but distinguishable tendency for the stiffening overall effect of interactions, indicating a slight dominance of the shielding mode of interactions. The reason for this tendency is not fully clear. We suspect that the prohibition for spacings between substantially overlapping cracks to be smaller than 0.15 of the crack length (that made the sample arrays slightly non-random) may have created a slight "bias" in favour of shielding.

We also calculated the shear modulus for parallel crack arrays (for two arrays, $\rho = 0.15$ and 0.20). It differed from the predictions for non-interacting cracks by less than 1.5%.

Preservation of orthotropy for interacting cracks. As discussed above, for *non-interacting* cracks orthotropy (coaxial to α) is a rigorous result in *2-D*. Consistently with the fact that, due to cancellation of competing effects, the approximation of non-interacting cracks remains accurate at high crack densities, *orthotropy* can be expected to hold at high ρ.

We examined *deviation from orthotropy* in sample arrays of non-randomly oriented (but randomly *located*) cracks, by solving the interaction problem for two families of parallel cracks of equal density inclined at 30° to each other. At $\rho = 0.24$ (significant interactions) the deviation from orthotropy produced by interactions was very small: in the principal coordinate system of α the non-orthotropic compliances ΔM_{1112} and ΔM_{2212} were 10^{-3}- 10^{-4} of the orthotropic compliances, i.e. within the accuracy of the results.

This means that *characterization of crack arrays by the crack density tensor remains adequate even at high crack densities* when interactions are strong, and implies that the "natural" coordinate system (coaxial to α) remains the system of choice for calculation of the effective moduli.

DISCUSSION

The results show that, well into the interval of crack densities (ρ up to 0.35) where the interactions become significant, *the approximation of non-interacting cracks remains quite accurate.*

The underlying reason for this accuracy is *not* that the interactions can be neglected, but that the competing effects of stress shielding and stress amplification *cancel* each other.

This is a direct consequence of the fact that introduction of traction-free cracks does not change the average stress in the solid (provided *tractions* are prescribed on the boundary). Therefore, if a certain number of "new" cracks is introduced into the environment of the preexisting ones in a *random fashion*, these new cracks will, *on the average*, experience no effect of the preexisting cracks. In the language of stress superpositions, the additional tractions $\Delta \mathbf{t}^i$ will be of both amplifying and shielding nature on different cracks; on the average, their impacts will cancel each other.

We emphasize that this conclusion assumes the *absence of "bias"* in crack statistics towards either amplifying or shielding arrangements. Otherwise (in "ordered" arrays, for example) the impact of interactions can be very large, both in the direction of "softening" and "stiffening".

The reported results are for the *2-D* configurations. The approximation of non-interacting cracks will remain accurate in *3-D* as well, due to the same mechanism of cancellation of shielding and amplification effects. Moreover, we expect the scatter of the results to be smaller, since interactions are weaker in *3-D* (see [1,2]).

ACKNOWLEDGEMENT

This work was supported by the U.S. DOE, through grant to Tufts University.

REFERENCES

1. M.Kachanov, "Effective.Elastic Properties of Cracked Solids: Critical Review of Some Basic Concepts", *Appl.Mech. Rev.*, **45**(8), 304-335 (1992).
2. M.Kachanov, "Elastic Solids with Many Cracks and Related Problems", in *Advances in Appl. Mechanics* (J.Hutchinson and T,Wu, eds), **30**, 259-433(1993).
3. J.R.Bristow, "Microcracks and the Static and Dynamic Elastic Constants of Annealed and Heavily Cold-Worked Metals", *British J.Appl.Phys.*, **11**, 81-85 (1960).

POTENTIAL DROP CRACK GROWTH MONITORING IN HIGH TEMPERATURE BIAXIAL FATIGUE TESTS

B. P. Fitzgerald and E. Krempl
Mechanics of Materials Laboratory
Rensselaer Polytechnic Institute
Troy, New York 12180-3590

Abstract. The present work describes a procedure for monitoring crack growth in high temperature, biaxial, low cycle fatigue tests. The reversing DC potential drop equipment monitors smooth, tubular type 304 stainless steel specimens during fatigue testing. Electrical interference from an induction heater is filtered out by an analog filter and by using a long integration time. A Fourier smoothing algorithm and two spline interpolations process the large data set. The experimentally determined electrical potential drop is compared with the theoretical electrostatic potential that is found by solving Laplace's equation for an elliptical crack in a semi-infinite conducting medium. Since agreement between theory and experiment is good, the method can be used to measure crack growth to failure from the threshold of detectability.

TEST PROCEDURE

THE laboratory equipment consists of a computer-controlled MTS servohydraulic testing machine and a computerized DC potential drop system. The potential drop monitoring system was designed by the first author and consists of a constant current power supply, a passive RC filter bank, a multichannel digital voltmeter, solid state relays, and a 386 personal computer with a thermocouple board and a general purpose interface bus.

Testing is performed in strain control, using an MTS high temperature biaxial extensometer. Smooth type 304 stainless steel tubular specimens with an inside diameter of 15.1 mm and an outside diameter of 18.6 mm are tested. The wall thickness was reduced by 10% in the gauge section to promote crack initiation in that region. For the initial tests, a sinusoidal command signal with strain amplitude of $\epsilon_a = .005$ was used. In follow-on tests, shear strain control was slaved in-phase to the axial channel to achieve proportional loading, in which the axial and shear strain amplitudes were chosen so as to satisfy the relation

$$\epsilon^2_{a(eff)} = \epsilon^2_a + \frac{1}{3}\gamma^2_a, \quad \epsilon_{a(eff)} = .005.$$

Temperature is maintained at 538°C with a 10 kHz induction heater and controller. The use of thirteen type K thermocouples provides excellent coverage of the gauge section. Five thermocouples are located in the gauge section mid plane, four 12.7 mm above the mid plane, and four are located below. One thermocouple is used for heater control, two for auxiliary indication, nine for post-test compensation of the voltage data, and one for an installed ready spare. The desired temperature and temperature distribution is achieved by positioning two heating coils with a threaded reach rod system designed by the first author. To prepare for an experiment, a specimen is gripped and heated in manual control to 538°C, after which the heater is switched to automatic. The heater coils are adjusted both up, both down, together, or farther apart, as needed, using the reach rods, until a temperature distribution uniform within ±2.5°C of the desired temperature is achieved. Over the course of the test, oxidation decreases the material thermal conductivity, resulting in an axial shift in the temperature distribution; however, no channel changes by more than 3.5°C from its starting value.

A constant 12A direct current is passed through the specimen. The potential drop is measured across the gauge section with nine voltage probe pairs connected to a multichannel digital voltmeter, and stored on the 386 personal computer. The voltage probes consist of two 0.127 mm diameter chromel wires spot welded to the specimen surface (Figure 1). To allow for placement of the extensometer and the thermocouples, the potential drop leads are arranged in

three equally spaced groups of three. Electrical noise originating from the induction heater is largely eliminated by an RC filter bank and by using a long voltmeter integration time. Care is taken to electrically insulate the upper specimen grip from the load frame to eliminate DC current leakage. In order to compensate for the thermocouple potential arising from minor changes in gauge section temperature gradients, the current is reversed after every reading, using the solid state relays, and the voltages are remeasured. This is called the reversing DC electrical potential drop method [1]. After reversing the current, it is necessary to wait 0.5 s for the RC filter transient to decay before remeasuring the potential drop. Allowing time for passive filter decay and voltmeter integration, four seconds are required to obtain the positive and negative voltage readings. Mechanical test data (axial load, torque, axial and shear strain, and command signal), the cycle count, elapsed time, and thermocouple channel readings are recorded in synchronization with the potential drops. Approximately five samples are taken per cycle. To minimize the impact of aliasing on the data, the mechanical cycling frequency (0.04833 Hz) was selected so that the sampling frequency (0.25 Hz) is not an exact multiple.

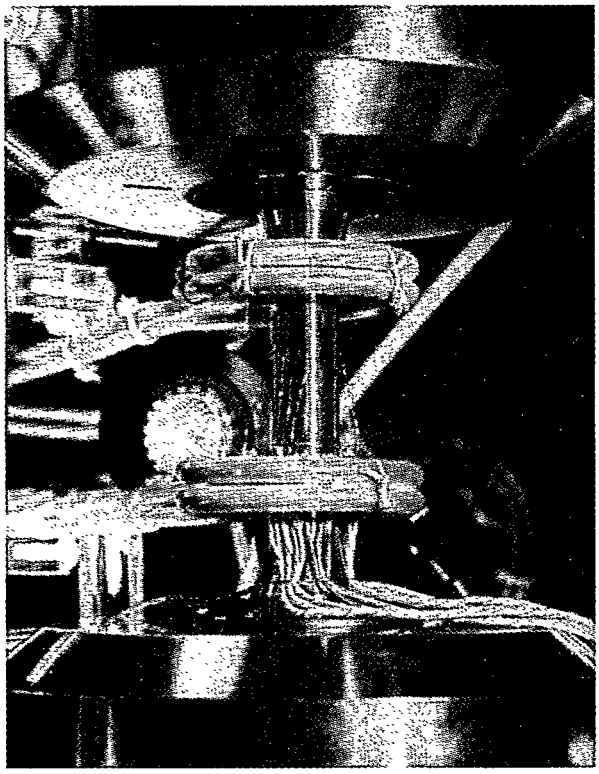

Figure 1: *View of potential drop leads and induction coil arrangement.*

To summarize, the data acquisition proceeds as follows: Mechanical data (load, strain, *etc.*) is read from the test controller and transferred to the 386 personal computer. The current is switched positive, the thermocouples are read, and following a delay, the potential drops are read. The current is switched negative and following a delay, the potential drops are reread. This cycle repeats continuously. Figure 2 (next page) shows the relationship of the test equipment and instrumentation.

During the test, the load (or torque) is plotted on an x-y flatbed plotter, and the cyclic load amplitude is checked frequently for a decrease that would warn of a crack formation. In addition, potential drop readings are displayed as they are read and a rough plot of potential drop *vs.* time is maintained by hand and checked for sudden changes. Finally, without interrupting the test, the specimen surface is visually inspected for cracks every 30 minutes using a portable 25× microscope. The test is stopped when a crack can be seen with the microscope, or with the unaided eye. However, the extensometer heat shield blocks complete visual coverage of the specimen surface. In all tests to date, the crack had grown very long before it could be seen. After the test has completed, the specimen is removed from the testing machine, and the crack length, depth and location are measured.

DATA ANALYSIS

The potential drop data consist of positive and negative values. By taking the difference between them, we compensate for changes in thermocouple emf's occurring in the potential drop leads. Also, a temperature correction is applied to compensate for specimen electrical resistivity changes due to temperature variation.

The voltage oscillates within a 150μV band (refer to subplot 1 of Figure 3). The periodic nature of the signal lends itself to standard signal processing methods [2]. First, we interpolate the data with respect to time using the low pass filter of Oetken [3], as shown in subplot 2 of Figure 3. Since we have sampled the signal at .25 Hz, which is well above the Nyquist frequency, the interpolation is accurate, and free of aliasing.

The signal oscillates within a 150μV range due to the cyclic specimen length change: In a cyclic test with a nonzero axial strain amplitude, the potential drop oscillates in phase with strain as a consequence of the standard resistance relation, $R = \rho l/A$, where l is the gauge length. The voltage oscillation dominates the signal, and makes the entire Fourier analysis possible, but is unrelated to crack size measurement, and must be accounted for. If a crack is present,

the maximum potential drop occurs at maximum crack extension; therefore we identify withing the interpolated data, the maximum per-cycle potential drop. Four such maxima are shown in subplot 3 of Figure 3. The maximum per-cycle potential drop for an entire test is shown in subplot 4 of the same figure.

The per-cycle potential drop maxima are then interpolated with respect to time using a piecewise cubic smoothing spline [4]. For a given voltmeter channel, the ratio of potential drop, $\Phi(t)$ to the starting value, $\Phi(0)$, is given by $\phi = \Phi(t)/\Phi(0)$, and is shown plotted in subplot 1 of Figure 4. The curves for the group of potential drop leads with the highest reading ϕ (probes 7, 8, and 9 in this case) are centered for clarity.

The ϕ values are interpolated again, this time with respect to time (t) and circumferential angular position (θ), accounting for the unequal potential drop lead spacing. The two dimensional tensor product spline of de Boor was used over a uniform output grid. The boundary conditions imposed on $\phi(\theta, t)$ are:

$$\phi(0, t) = \phi(2\pi, t),$$

$$\phi(\theta, 0) = \frac{d\phi}{dt}(\theta, 0) = 0.$$

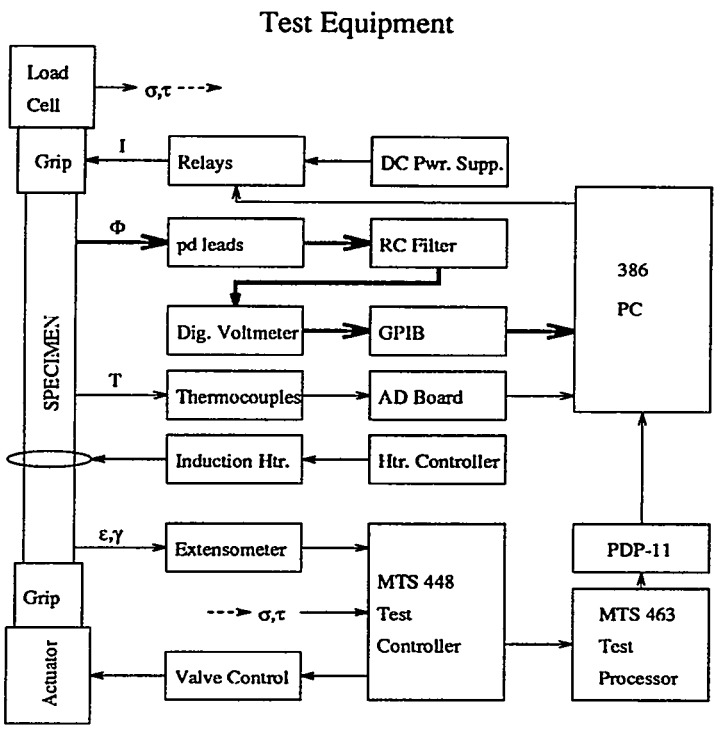

Figure 2: *Block diagram of test equipment.*

Initially, the potential drops measured on all channels remain nearly level, or rise together. The rate of increase rises gradually, but uniformly. The uniform rise in potential drop may be due to the increased electrical resistance resulting from progressive surface oxidation at high temperature. Other factors, including the dislocation density increase from hardening, the formation of many uniformly distributed small cracks, or other unknown chemical and physical changes also result in a uniform potential drop rise. Eventually, a crack grows large enough to be detected and the potential drop for the probe pair closest to the crack begins to rise faster than the others. However, the crack affects the potential drop far away, too, and all potential drop readings increase faster as a result (refer to subplot 1 of Figure 4).

Clearly, we need a way to separate the local rise in ϕ due to crack growth from the general rise in ϕ which is affected by many factors in unknown proportion. Therefore, we subtract the lowest ϕ from all the others. We define the incremental normalized potential drop at time t as, $\phi_{inc}(\theta, t) = \phi(\theta, t) - \min(\phi(\theta, t))$. A crack is "detectable" when a localized rise in ϕ_{inc} is noticeable. As the crack grows, the ϕ_{inc} curve around the crack broadens and grows higher (refer to subplot 2 of Figure 4). The highest curve is centered for clarity. The y axis is arbitrarily chosen to originate from the highest curve.

We note that for the longest test (refer to Figure 5) the time required to perform the Fourier interpolation was 7:49 (wall clock, in mm:ss) on a Sun Sparc 10 model 30 with fifty users logged in at the time. An IBM Powerstation 320H performs the calculations in about the same time. The smoothing spline required 3:11 and the tensor spline interpolation required 0:07. The raw data consisted of a 15607 x 37 double precision array requiring 4.6 MB (megabytes) of memory. The largest array used was for the interpolated voltages, and required 11.2 MB of memory. The total memory requirement for the process was 41.9 MB.

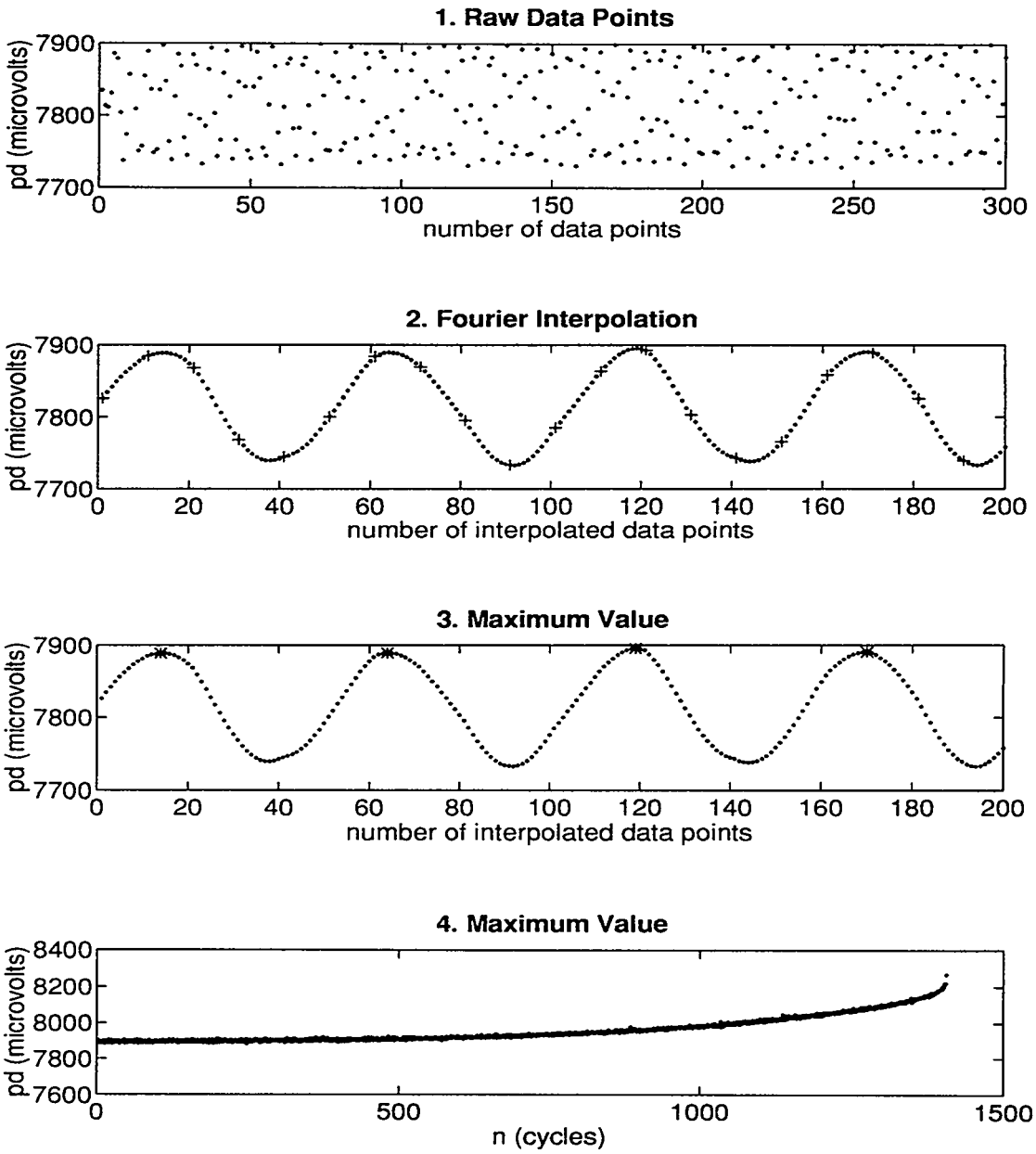

Figure 3: *Fourier analysis.* The procedure for performing the Fourier interpolation on one of nine potential drop (pd) channels is illustrated in this figure, for test c9. **1.** 300 raw data points (approximately 58 fatigue cycles) are shown. Note the false wave pattern. There appear to be five overlapping waves shown. This an artifact of the data collection method. **2.** Only 20 raw data points (+) are shown. The 10:1 Fourier interpolation is plotted with dots. **3.** The per-cycle maxima (∗) of the Fourier interpolation is plotted. **4.** Subplot 3 showed only four potential drop maxima. Subplot 4 shows an entire test ($N_f = 1464$).

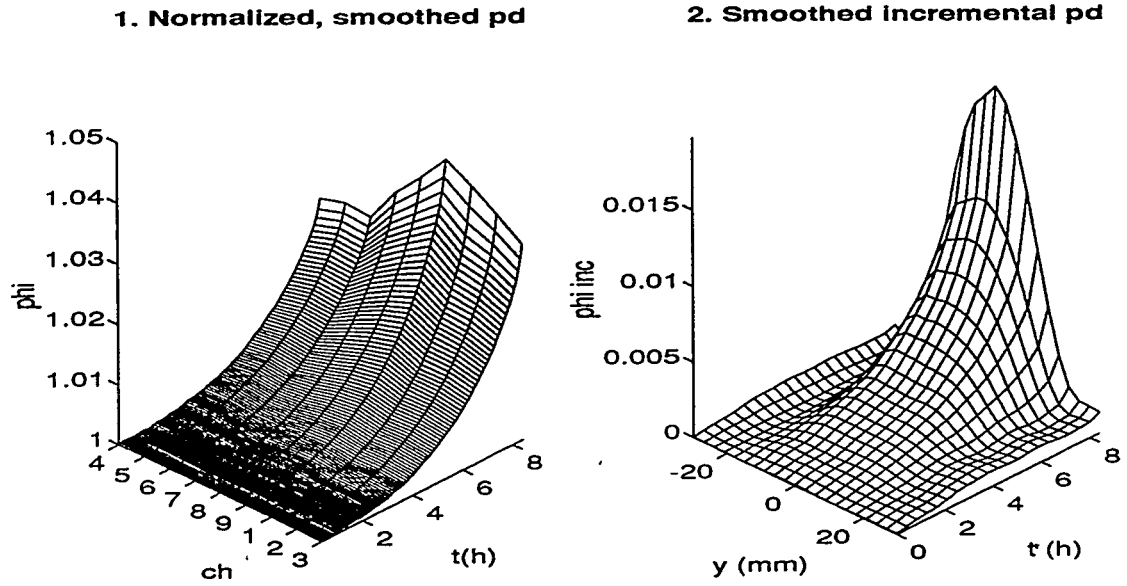

Figure 4: *Cubic spline interpolation procedure.* **1.** The pd maxima shown in subplot 4 of Figure 3 are smoothed, normalized, and interpolated at 101 time points, and plotted for all nine voltmeter channels (ch). **2.** The mesh points in subplot 1 are interpolated over a uniform mesh in two dimensions, time (t) and position (y). y is measured horizontally from the highest curve. The lowest φ per time step was subtracted to obtain ϕ_{inc}.

TEST RESULTS

A total of six experiments were performed and are summarized in Figure 5. Tests c6 and c7 were axial fatigue tests ($\gamma_a = 0$). The follow-on tests were proportional loading tests. In tests c8 and c9 the axial and shear strain amplitudes were both .0043 and in tests d0 and d1, the axial strain amplitude was .0025 and the shear strain amplitude was .0075. It appears that the cycles-to-failure (N_f) increases as ϵ_a decreases, as might be expected. In all tests, φ initially rises uniformly for all channels, and as a result, ϕ_{inc} remains close to zero. This is shown on all subplots in Figure 5 as a "plateau" for the initial portion of the test. Eventually, a "hill" appears on the plot and grows and broadens. The increase in ϕ_{inc} corresponds to crack growth. In all cases, the location of the hill corresponds to the position of the crack.

For test c6, the data is shown truncated after 1443 cycles (8.08 h). After this time, the crack had grown very large, and the ϕ_{inc} for those times is too high to plot on the same scale as the portion of the test shown. For the same reason, the c7 test data is shown truncated after 265 cycles (2.67 h).

Test c7 was intended to check the effect of introducing a defect of known geometry part way into the test. After 176 cycles a .54 mm diameter, .65 mm deep hole was drilled. The result was a slight rise in ϕ_{inc}, which appears as a small upward step at $(y, t) = (0, .97)$ in subplot c7 of Figure 5. After $t = .97$h, a crack formed at the hole and grew until the test was stopped. This corresponds to the rise and spread of the curve after .97 h in the plot.

THEORETICAL POTENTIAL DROP NEAR THE CRACK

In this section, we compute the potential drop predicted by electrostatic theory for the measured final crack geometry. We will compare our potential drop measurements with Tada'a solution to Laplace's equation for a semi-elliptical flat crack in a semi-infinite body [5] (refer to Figure 6). The potential at any point in the body is given by:

$$\Phi = zE_\infty \left\{ 1 + \frac{\lambda^2}{2E(k)} \int_{D^2}^{\infty} \frac{dt}{t\sqrt{t(t+1)(t+\lambda^2)}} \right\}, \tag{1}$$

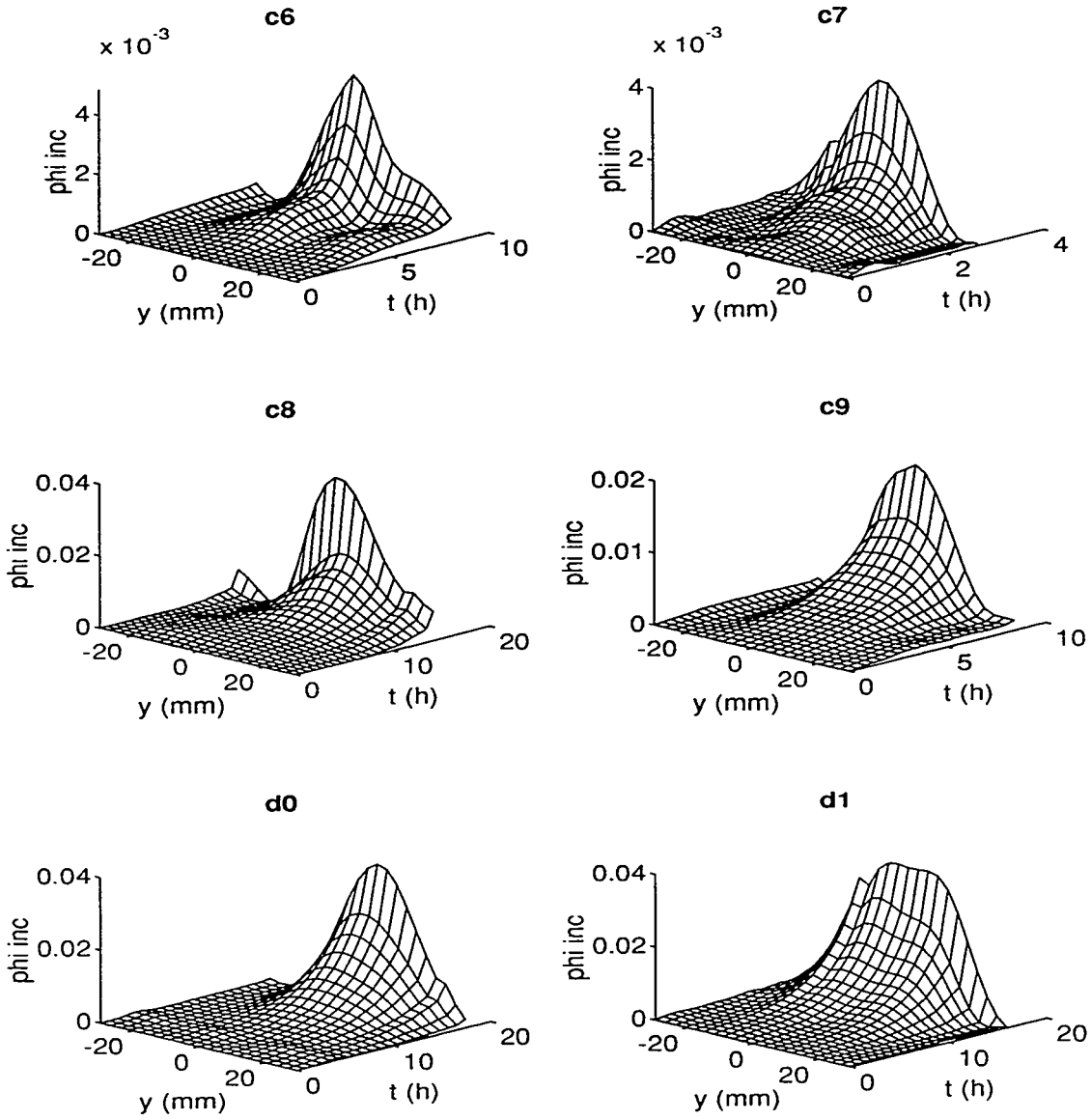

Test	ϵ_a	$\frac{1}{3}\gamma_a$	N_f	t_f (h)	$2a_f$ (mm)	ϕ_{inc}	Data file size (MB)	Number of data points
c6	.005	0	1461	8.2	37.2	4.9×10^{-3}†	1.7	7329
c7	.005	0	538	3.0	13.9	4.0×10^{-3}‡	0.7	2690
c8	.0043	0.0025	2249	13.7	19.3	3.9×10^{-2}	2.9	11640
c9	.0043	0.0025	1464	8.4	10.9	2.0×10^{-2}	1.8	7510
d0	.0025	0.0043	3021	17.5	26.1	3.9×10^{-2}	3.7	14310
d1	.0025	0.0043	2774	16.0	16.3	3.8×10^{-2}	3.4	14340

Figure 5: *Experimental results.* N_f = cycles to failure. t_f = time to failure. $2a_f$ = final crack size. ϕ_{inc} = final incremental normalized potential drop. Tests c6 and c7 were axial fatigue tests. Tests c8, c9, d0, and d1 were biaxial tests. †after 1443 cycles (8.08 h). ‡after 265 cycles (2.67 h). In test c7, a .54 mm diameter hole was drilled after 176 cycles (0.97 h) as a check on the sensitivity of the experimental technique.

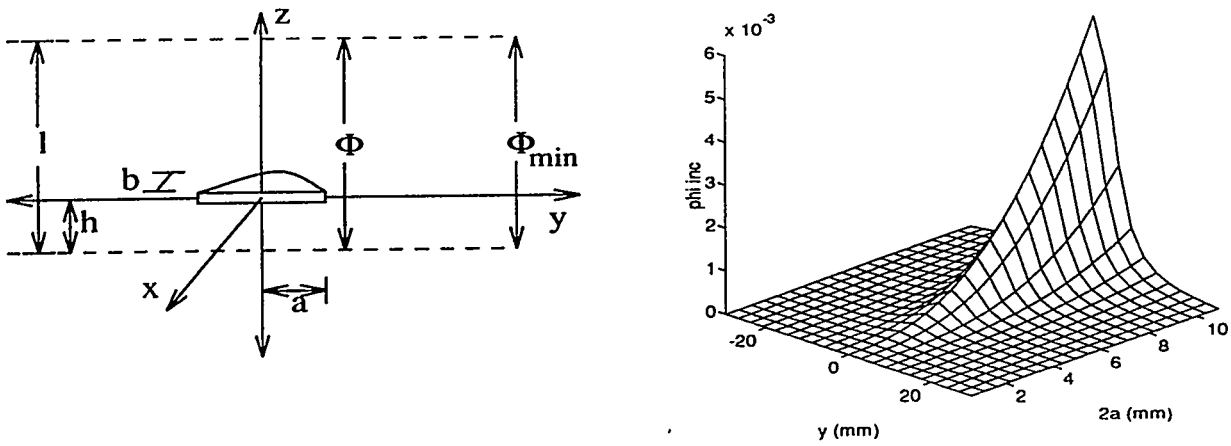

Figure 6: *Crack geometry and Tada's solution to Laplace's equation*

where E_∞ is the electric field strength at infinity, E is the complete elliptic integral of the second kind with modulus k, where $k = \sqrt{1-\lambda^2}$, λ is the crack "aspect ratio", given by $\lambda = b/a$, and D is the "effective distance" measured from the crack to the position (x, y, z), and is found by solving

$$\frac{X^2}{D^2+\lambda^2} + \frac{Y^2}{D^2+1} + \frac{Z^2}{D^2} = 1. \tag{2}$$

where $X = x/a$, $Y = y/a$, and $Z = z/a$. For surface potential measurements $x = 0$, and the solution to equation 2 is:

$$D(Y,Z) = \sqrt{\frac{Y^2+Z^2-1+\sqrt{(Y^2+Z^2-1)^2+4\cdot Z^2}}{2}}.$$

Equation 1 gives the normalized potential drop from a single voltage probe pair lead to the crack center, but a potential drop measurement is taken between *pairs* of leads. For a crack located at a distance h from the lower row of leads, the potential drop is

$$\Phi = hE_\infty \left\{ 1 + \frac{\lambda^2}{2E(k)} \int_{D^2_{y,h}}^{\infty} \frac{dt}{t\sqrt{t(t+1)(t+\lambda^2)}} \right\} + (l-h)E_\infty \left\{ 1 + \frac{\lambda^2}{2E(k)} \int_{D^2_{y,l-h}}^{\infty} \frac{dt}{t\sqrt{t(t+1)(t+\lambda^2)}} \right\}. \tag{3}$$

where $D_{y,h} = D\left(\frac{y}{a}, \frac{h}{a}\right)$ and $D_{y,l-h} = D\left(\frac{y}{a}, \frac{l-h}{a}\right)$. The observed potential drop should correspond to equation 3 only if the crack is the sole factor affecting electrical resistivity. However, it was mentioned in the Analysis section that there are many other factors that have a much greater influence on Φ than the crack does. The theoretical Φ of equation 3 includes the general rise noted on all channels, which we subtract to obtain the incremental value.

Let the minimum potential drop be Φ_{min}, calculated from equation 3 using $y = y_{max}$. In the cylindrical geometry, y_{max} is half the specimen circumference, or 14.5 mm in specimen c9, for example. If we subtract the minimum potential drop from any other potential drop, we obtain an "incremental" value. If we normalize this potential to the value that would be obtained if no crack were present, we predict:

$$\phi_{inc} = \frac{1}{l} \cdot \frac{\lambda^2}{E(k)} \left\{ h \int_{D^2_{y,h}}^{D^2_{y_{max},h}} \frac{dt}{t\sqrt{t(t+1)(t+\lambda^2)}} - (l-h) \int_{D^2_{y,l-h}}^{D^2_{y_{max},l-h}} \frac{dt}{t\sqrt{t(t+1)(t+\lambda^2)}} \right\}. \tag{4}$$

An approximate evaluation of equation 4 is plotted in Figure 6, using the measured final specimen crack geometry for test c9. In that test, a 10.9 mm crack formed 4.7 mm above the lower row of potential drop leads. The predicted ϕ for

a range of crack sizes from $2a = 0.545$ mm to the actual final value of $2a = 10.9$ mm is plotted, for a probe spacing of 25.4 mm. By the end of the test, the crack had completely breached the wall thickness (1.61 mm), so this value was used for the final semiminor axis, b, of the ellipse shown in Figure 6. A constant crack aspect ratio of $b/a = \lambda = 0.29$ was assumed for preparing the plot.

In test c9, the final experimentally determined peak value for ϕ_{inc} was 0.020 (refer to Figure 4). The peak value shown in Figure 6 is 0.006. We reconsider here the assumptions used to derive the theoretical value. A semi-infinite medium was assumed. For cracks much shorter than the specimen circumference, an infinite medium in the $\pm y$ directions is a reasonable assumption. Likewise, for cracks much shallower than the wall thickness, a semi-infinite medium in the $-x$ direction is reasonable. These assumptions would probably have been valid early in a test when the crack was small, but are poor at the end of a test because the crack is long compared to the circumference, and is completely through the wall.

CONCLUSIONS

There is qualitative agreement between the experimentally determined potential drop shown in Figure 4 and the theoretical value predicted by electrostatic theory, as shown in Figure 6. The experimentally determined ϕ_{inc} curve has the shape of a hill symmetric about the crack, and broadens and increases as the crack grows. The theoretical ϕ_{inc} has a similar shape, for crack geometry similar to the experimental one.

For the example test (c9) the final experimental ϕ_{inc} exceeds the theoretical by a factor of three because a semi-elliptical crack was assumed, but the actual final geometry was a through crack. Future work will include fitting the experimental data to other solutions to Laplace's equation, including a through crack [6]. More tests such as c7, in which a hole was drilled, will be performed. The measured potential drop will be compared to the theoretical value for the actual hole.

References

[1] W. R. Catlin, D. C. Lord, T. A. Prater, and L. F. Coffin. The reversing dc electrical potential method. In ASTM-STP877, pages 67–85, 1983.

[2] R. W. Hamming. *Digital Filters*. Prentice-Hall, Inc., Englewood Cliffs, New Jersey, 1983.

[3] G. Oetken, T. W. Parks, and H. W. Schüssler. A computer program for digital interpolator design. In *Programs for Digital Signal Processing*, chapter 8.1. IEEE Press, New York, 1979.

[4] C. de Boor. *A Practical Guide to Splines*. Springer-Verlag, New York, 1978.

[5] N. Tada. Monitoring of a surface crack in a finite body by means of electrical potential technique. *Int. J. Fract.*, 57:199–220, 1992.

[6] H. H. Johnson. Calibrating the electric potential method for studying slow crack growth. *Mater. Res. and Standards*, 5(9):442–445, 1965.

THE PREISACH MODEL WITH STOCHASTIC INPUT AS A MODEL FOR AFTEREFFECT

Isaak D. Mayergoyz
Department of Electrical Engineering
University of Maryland
College Park, MD 20742

Can E. Korman
Department of Electrical Engineering and Computer Science
The George Washington University
Washington, DC 20052

ABSTRACT

In previous papers [1]-[2], it has been suggested to use the Preisach model driven by stochastic inputs as a model for aftereffect. However, in these papers the stochastic inputs have been modeled by discrete time *i.i.d.* (independent identically distributed) random processes. Here, we further extend the aforementioned approach by modeling the stochastic inputs by continuous time diffusion processes. It is shown that the mathematical machinery of the "exit problem" is instrumental for calculations of time evolutions of the expected value of the output of the Preisach model.

INTRODUCTION

It is well-known that the physical origin of hysteresis is due to the multiplicity of metastable states. At equilibrium, large deviations of random thermal perturbations may cause a hysteretic system to move gradually from higher to lower energy metastable states. This phenomenon is generally referred to in the literature as "aftereffect," "viscosity," or "creep."

Traditionally, the modeling of hysteresis and viscosity has been pursued along two quite distinct lines. In phenomenological modeling of hysteresis the Preisach approach has been prominent, while the viscosity phenomenon has been studied by using thermal activation type models. It is desirable to develop the uniform approach to the modeling of both hysteresis and viscosity. Recently, it has been suggested to use the Preisach model driven by stochastic inputs as model for aftereffect (see [1]-[3]). However, in these publications, the stochastic inputs have been modeled by discrete time *i.i.d.*

(independent identically distributed) random processes. Below, this approach is further extended by modeling the stochastic inputs by continuous time diffusion processes. From the mathematical point of view, it makes the problem much more complicated. It is shown in the sequel that these difficulties can be largely overcome by using the mathematical machinery of the "exit problem."

TECHNICAL DISCUSSION

Consider a deterministic input $u(t)$ of the Preisach model which at time $t = 0$ assumes some value u_0 and remains constant thereafter. In a purely deterministic situation, the output would remain constant for $t \geq 0$ as well. To model the aftereffect, we assume that some noise is superimposed on the constant input. In other words, we assume that the Preisach model is driven by the process:

$$x_t = u_0 + X_t, \qquad \bar{X}_t = 0. \tag{1}$$

The noise X_t will be modeled by a (continuous time and continuous samples) diffusion process which is a solution to the Ito stochastic differential equation:

$$dX_t = b(X_t)dt + \sigma(X_t)dW_t \tag{2}$$

The output f_t of the Preisach model

$$f_t = \iint\limits_{\alpha \geq \beta} \mu(\alpha, \beta)\hat{\gamma}_{\alpha,\beta}x_t d\alpha d\beta \tag{3}$$

will be a random process as well, and we shall be interested in the time evolution of the expected value, $\bar{f}_t$, of this output process.

Since integration is a linear operation, from (3) we derive:

$$\bar{f}_t = \iint\limits_{\alpha \geq \beta} \mu(\alpha, \beta)E\{\hat{\gamma}_{\alpha,\beta}x_t\}d\alpha d\beta. \tag{4}$$

Thus, the problem is reduced to the evaluation of the expected value, $E\{\hat{\gamma}_{\alpha,\beta}x_t\}$.

Let

$$q_{\alpha,\beta}(t) = Prob\{\hat{\gamma}_{\alpha,\beta}x_t = +1\}. \tag{5}$$

Since $\hat{\gamma}_{\alpha,\beta}x_t$ may assume only two values $+1$ and -1, we find:

$$E\{\hat{\gamma}_{\alpha,\beta}x_t\} = 2q_{\alpha,\beta}(t) - 1 \tag{6}$$

In this way, the problem is reduced to the calculation of $q_{\alpha,\beta}(t)$. The last quantity can be expressed in terms of switching probabilities $P_k^+(t)$ and $P_k^-(t)$ which are defined as follows:

$$P_k^+(t) = Prob\left\{ \begin{array}{l} k \text{ switchings of } \hat{\gamma}_{\alpha,\beta} \text{ during} \\ \text{timeinterval } (0,t) \mid \hat{\gamma}_{\alpha,\beta}\ x_0 = +1 \end{array} \right\} \tag{7}$$

$$P_k^-(t) = Prob\left\{ \begin{array}{l} k \text{ switchings of } \hat{\gamma}_{\alpha,\beta} \text{ during} \\ \text{timeinterval } (0,t) \mid \hat{\gamma}_{\alpha,\beta}\ x_0 = -1 \end{array} \right\} \tag{8}$$

By using the above switching probabilities, we derive:

$$q_{\alpha,\beta}(t) = \left\{ \begin{array}{ll} \sum_{k=0}^{\infty} P_{2k}^+(t), & \text{if } \hat{\gamma}_{\alpha,\beta} x_0 = +1 \\ \sum_{k=0}^{\infty} P_{2k+1}^-(t), & \text{if } \hat{\gamma}_{\alpha,\beta} x_0 = -1. \end{array} \right. \tag{9}$$

The last expression is valid because occurrences of different numbers of switchings are nonintersecting (disjoint) events.

Next, we shall discuss the mechanism of switching. It is clear from Figure 1 that the first switching occurs at the moment when the stochastic process x_t starting from the point x_0 exits the semi-infinite interval (β, ∞). Then, the second switching occurs at the moment, when the process x_t starting from the point $x = \beta$ exits the semi-infinite interval $(-\infty, \alpha)$. The third switching takes place at the moment when the process x_t starting from the point $x = \alpha$ exists the semi-infinite interval (β, ∞). It is apparent that the mechanism of all subsequent even switchings is identical to the mechanism of the second switching, while all subsequent odd switchings occur in the same manner as the third switching. Thus, switchings of rectangular loops $\hat{\gamma}_{\alpha,\beta}$ are closely related to the exit problem for stochastic processes. This problem is one of the most studied problems in the theory of diffusion processes and the mathematical machinery developed for the solution of this problem will be utilized in the calculation of probabilities $P_k^{\pm}(t)$.

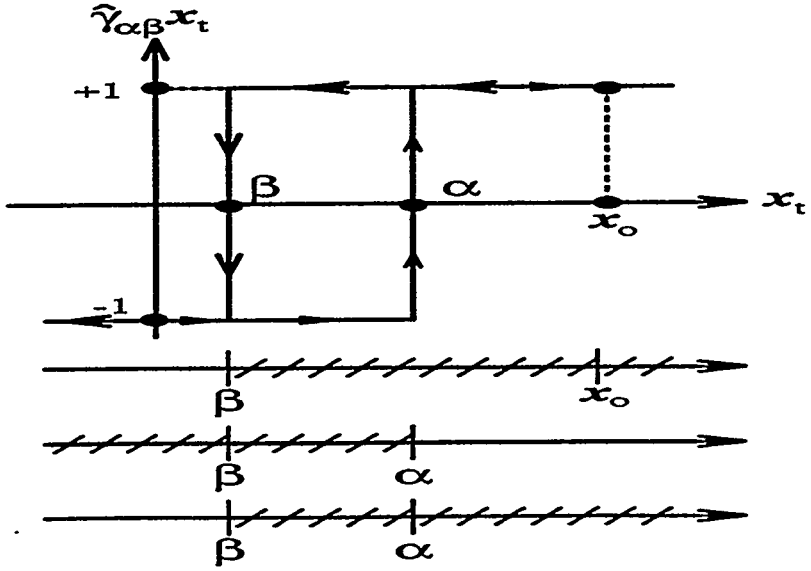

Figure 1: Mechanism of Switching

The exit problems described above can be characterized by exit times $\tau_x^{\pm}$ which are random variables. In the above notation for the exit times, subscript "x" means that process x_t starts from point x, while superscripts "$\pm$" mean that upward and downward switchings, respectively, occur at these exit times. Next, we introduce the functions:

$$v^{\pm}(t,x) = Prob\{\tau_x^{\pm} \geq t\}, \tag{10}$$

$$V^{\pm}(t,x) = e(t) - v^{\pm}(t,x), \tag{11}$$

where e(t) is a unit step-function. It is clear that,

$$V^{\pm}(t,x) = Prob\{\tau_x^{\pm} \leq t\}, \tag{12}$$

which means that $V^{\pm}(t,x)$ has the meaning of cumulative distribution function for the random variable $\tau_x^{\pm}$. This, in turn, implies that

$$\rho^{\pm}(t,x) = \frac{\partial V^{\pm}(t,x)}{\partial t} \tag{13}$$

is the probability density function for the random variable $\tau_x^{\pm}$.

It is apparent from (11) - (13) that $\rho^{\pm}(t,x)$ can be easily computed if $v^{\pm}(t,x)$ are somehow found. It turns out (and this is a well known result from the theory of stochastic processes) that $v^{\pm}(t,x)$ is the solution to the following initial-boundary value problem for the backward Kolmogorov equation:

$$\frac{\partial v^{\pm}}{\partial t} = \frac{\sigma^2(x)}{2}\frac{\partial^2 v^{\pm}}{\partial x^2} + b(x)\frac{\partial v^{\pm}}{\partial x}, \tag{14}$$

$$v(0,x) = 1, \quad v(t,c^{\pm}) = 0, \tag{15}$$

where $c^{\pm}$ are the exit points for the process.

Next, we shall show that switching probabilities $P_k^{\pm}(t)$ can be expressed in terms of $v^{\pm}(t)$ and $\rho^{\pm}(t)$. Note that, according to (11)-(13), $\rho^{\pm}(t)$ are related to $v^{\pm}(t)$ as follows:

$$\rho^{\pm}(t) = \frac{\partial}{\partial t}[e(t) - v^{\pm}(t)] \tag{16}$$

It is clear from the very definition of $v^{\pm}(t,x)$ that:

$$P_o^{\pm}(t) = v^{\pm}(t,0). \tag{17}$$

It is apparent from Figure 2 that the occurrence of exactly one downward switching is the union of the following disjoint elementary events: downward switching occurs in the time interval $(\lambda, \lambda+d\lambda)$

and then no upward switching occurs up to the time t. Due to the strong Markov property of X_t, the probability of the above elementary event is given by:

$$\rho^-(\lambda, 0)v^+(t-\lambda, \beta-u_o)d\lambda. \tag{18}$$

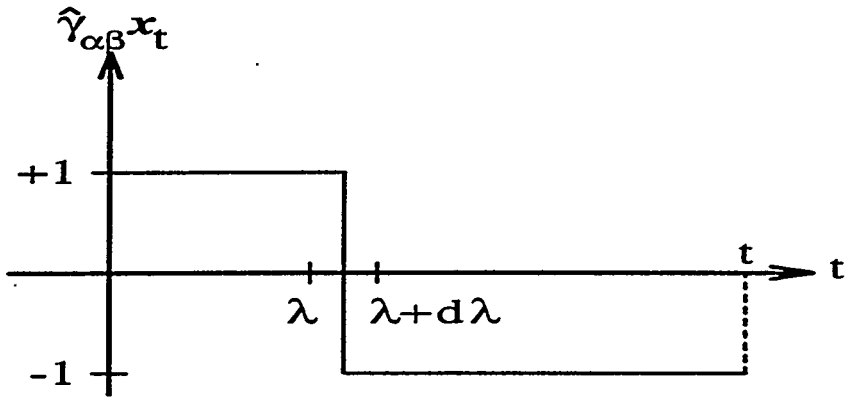

Figure 2: Occurrence of Exactly One Downward Switching

Now, the probability $P_1^+(t)$ of exactly one downward switching can be found by integrating (18) from 0 to t:

$$P_1^+(t) = \int_0^t \rho^-(\lambda, 0)v^+(t-\lambda, \beta-u_o)d\lambda. \tag{19}$$

In other words, $P_1^+(t)$ is the convolution of $\rho^-(t, 0)$ and $v^+(t, \beta-u_o)$:

$$P_1^+(t) = \rho^-(t, 0) * v^+(t, \beta-u_o). \tag{20}$$

By using similar reasoning, we can derive:

$$P_1^-(t) = \rho^+(t, 0) * v^-(t, \alpha-u_o) \tag{21}$$

Next, consider the probability $P_2^+(t)$ of the occurrence of exactly two switchings starting from the initial state $\hat{\gamma}_{\alpha\beta}x_o = 1$. According to Figure 3, this occurrence can be considered as the union of the following disjoint elementary events: downward switching occurs in the time interval $(\lambda, \lambda+d\lambda)$ and then exactly one upward switching occurs up to the time t. The probability of these elementary events is given by:

$$\rho^-(\lambda, 0)P_1^-(t-\lambda)d\lambda \tag{22}$$

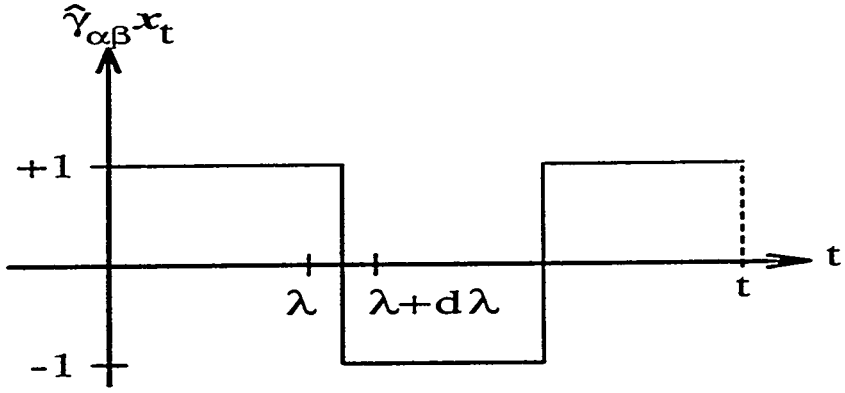

Figure 3: Occurrence of Exactly Two Switchings

Now, by integrating (22), we find:

$$P_2^+(t) = \int_0^t \rho^-(\lambda, 0) P_1^-(t, \lambda) d\lambda. \tag{23}$$

From (21) and (23) we obtain:

$$P_2^+(t) = \rho^-(t, 0) * \rho^+(t, \beta - u_o) * v^-(t, \alpha - u_o). \tag{24}$$

By using the same line of reasoning, we derive:

$$P_2^-(t) = \rho^+(t, 0) * \rho^-(t, \alpha - u_o) * v^+(t, \beta - u_o). \tag{25}$$

For the sake of conciseness, we introduce the notations:

$$\rho^{\pm}(t, 0) = \rho_o^{\pm}(t), \quad \rho^+(t, \beta - u_o) = \rho^+(t), \quad \rho^-(t, \alpha - u_o) = \rho^-(t), \tag{26}$$

$$v^{\pm}(t, 0) = v_o^{\pm}(t), \quad v^+(t, \beta - u_o) = v^+(t), \quad v^-(t, \alpha - u_o) = v^-(t). \tag{27}$$

Now, by using the same line of reasoning as before and the induction argument, we can easily derive the following expressions for the switching probabilities:

$$P_{2k}^+(t, u_o) = \rho_o^-(t) * \rho^+(t) * \overbrace{\rho^-(t) * \rho^+(t) * \cdots * \rho^-(t) * \rho^+(t)}^{2k-2 \ terms} * v^-(t), \tag{28}$$

$$P_{2k+1}^-(t, u_o) = \rho_o^+(t) * \overbrace{\rho^-(t) * \rho^+(t) * \cdots * \rho^-(t) * \rho^+(t)}^{2k \ terms} * v^-(t). \tag{29}$$

By substituting (28) and (29) into (9), we obtain the expression for $q_{\alpha\beta}(t)$ in terms of infinite series of iterated convolutions. These series can be reduced to geometric ones by employing Laplace transforms:

$$\tilde{\rho}(s) = \int_0^\infty \rho(t)e^{-st}dt, \qquad (\mathcal{R}e\ s > 0), \tag{30}$$

$$\tilde{v}(s) = \int_0^\infty v(s)e^{-st}dt. \tag{31}$$

It is clear that

$$|\ \tilde{\rho}(s)\ | < 1. \tag{32}$$

By using these Laplace transforms, from (17), (28), and (29) we obtain:

$$\tilde{P}_o^{\pm}(s) = \tilde{v}_o^{\pm}(s), \tag{33}$$

$$\tilde{P}_{2k}^{+}(s) = \tilde{\rho}_o^{-}(s)\tilde{\rho}^{+}(s)\tilde{v}^{-}(s)[\tilde{\rho}^{-}(s)\tilde{\rho}^{+}(s)]^{k-1}, \tag{34}$$

$$\tilde{P}_{2k+1}^{-}(s) = \tilde{\rho}_o^{+}(s)\tilde{v}^{-}(s)[\tilde{\rho}^{-}(s)\tilde{\rho}^{+}(s)]^{k}. \tag{35}$$

From (35) and (9), we derive:

$$\tilde{q}_{\alpha\beta}(s) = \frac{\tilde{\rho}_o^{+}(s)\tilde{v}^{-}(s)}{1-\tilde{\rho}^{-}(s)\tilde{\rho}^{+}(s)}, \quad if \quad \hat{\gamma}_{\alpha\beta}x_o = -1. \tag{36}$$

A similar expression can be derived for the case $\hat{\gamma}_{\alpha\beta}x_o = +1$.

According to (16)

$$\tilde{\rho}^{\pm}(s) = 1 - s\tilde{v}^{\pm}(s). \tag{37}$$

Thus, the problem of computing $\tilde{q}_{\alpha\beta}$ is reduced to the problem of determining $\tilde{v}^{\pm}(s)$. This can be accomplished by using the initial-boundary value problem (14)-(15). The complexity of this task will depend on the nature of the stochastic process X_t which models the noise in hysteretic systems. It is natural to require that the stochastic process which models the noise must be a stationary Gaussian Markov process. According to the Doob theorem, the only process which satisfies these requirements is the Ornstein-Uhlenbeck process. This process is the solution to the following Ito stochastic differential equation:

$$dX_t = -bX_t dt + \sigma dW_t, \tag{38}$$

where $\frac{1}{b}$ has the meaning of the correlation time. (This means that X_t and $X_{t'}$ are only significantly correlated if $\mid t - t' \mid \leq \frac{1}{b}$).

The backward Kolmogorov equation for the Ornstein-Uhlenbeck process has the form:

$$\frac{\partial v^{\pm}}{\partial t} = \frac{\sigma^2}{2}\frac{\partial^2 v^{\pm}}{\partial x^2} - bx\frac{\partial v^{\pm}}{\partial x}. \tag{39}$$

This equation should be considered jointly with initial and boundary conditions (15). By applying the Laplace transform to (39) and (15), we arrive at the following boundary value problem for $\tilde{v}^{\pm}(s)$:

$$\frac{\sigma^2}{2}\frac{d^2\tilde{v}^{\pm}(s,x)}{dx^2} - bx\frac{d\tilde{v}^{\pm}(s,x)}{dx} - s\tilde{v}^{\pm}(s,x) = -1, \tag{40}$$

$$\tilde{v}^{\pm}(s,c^{\pm}) = 0, \quad \tilde{v}^{\pm}(s,\infty) = \frac{1}{s}. \tag{41}$$

The solution to the boundary value problem (40) - (41) can be written in the form:

$$\tilde{v}^{\pm}(s,x) = \frac{1}{s}[1 - e^{\frac{x^2-(c^{\pm})^2}{4\lambda^2}}\frac{\mathcal{D}_{-\frac{s}{b}}(\frac{x}{\lambda})}{\mathcal{D}_{-\frac{s}{b}}(\frac{c^{\pm}}{\lambda})}], \tag{42}$$

where: $\mathcal{D}_{-\frac{s}{b}}(\frac{x}{\lambda})$ are parabolic cylinder functions, while $\lambda = \frac{\sigma}{\sqrt{2b}}$.

Expressions (36), (37), (42) jointly with (4) and (6) outline the main steps of the solution of the problem posed in this paper.

ACKNOWLEDGEMENT

This work was supported by the U.S. Department of Energy, Engineering Research Program.

REFERENCES

1. I.D. Mayergoyz, C.E. Korman, "Preisach Model with Stochastic Input as a Model for Viscosity," *J. Appl. Phys.* 69, 4, pp. 2128-2134 (1991).

2. I.D. Mayergoyz, C.E. Korman, "On a New Approach to the Modelling of Viscosity in Hysteretic Systems," *IEEE Trans. Magn.* 27, 6, pp. 4766-4768 (1991).

3. I.D. Mayergoyz, *Mathematical Models of Hysteresis*, Springer-Verlag, New York, NY (1991).

SMALL STRAIN HETEROGENEOUS DEFORMATION IN POLYCRYSTALS

By S.Shi[1], E.H. Jordan[1] and K.P. Walker[2]
[1]University of Connecticut
Storrs, Connecticut 06268
[2]Engineering Science Software, Inc.
315 Log Road, Smithfield, Rhode Island 02917

ABSTRACT

A program to study the micromechanics of polycrystalline deformation is outlined. The viscoplastic stress-strain behavior of a polycrystalline metal was successfully predicted from the measured single crystal properties of the same metal and the predictions were experimentally verified. Current research focuses on predicting the grain to grain heterogeneity of the mechanical response. This response has been predicted using both a self-consistent method and a more detailed method using an integral equation approach. The predicted response will be compared with a Moiré strain analysis and neutron diffraction experiments to be performed on a coarse grained sample of polycrystalline Hastelloy-X metal. The goal is to produce an experimentally verified model capable of realistically modeling the heterogeneous mechanical response due to orientation variation of the grains in the polycrystal.

INTRODUCTION

Engineering metals are made up of many randomly orientated singe crystal grains. This arrangement leads to locally heterogeneous deformation. A frequently pursued goal has been to successfully predict the average mechanical response of the polycrystalline aggregate from the properties of single crystal grains. Nearly all such efforts have utilized assumed single crystal properties to make predictions of the polycrystalline response. In the first part of this program both single crystal and polycrystal samples of the same alloy, Hastelloy-X, were tested so that actual single crystal viscoplastic properties could be used to make predictions of polycrystal behavior without having the freedom to choose "reasonable single crystal properties." In this real test of the predictive abilities of the self-consistent model it was found that very good predictions were possible. A representative prediction is shown in Fig. 1.

MICROMECHANICS MODELS

The self-consistent model is shown in Fig. 2. In this model the very complex three-dimensional geometry of randomly orientated grains is replaced by a spherical grain of single crystal material embedded in an isotropic effective medium, whose properties are obtained by angle averaging the constrained response of the embedded spherical grain. Because the isotropic properties depend on the response of the embedded grain, the self-consistent model is generally implicit. In the viscoplastic case, if a forward difference

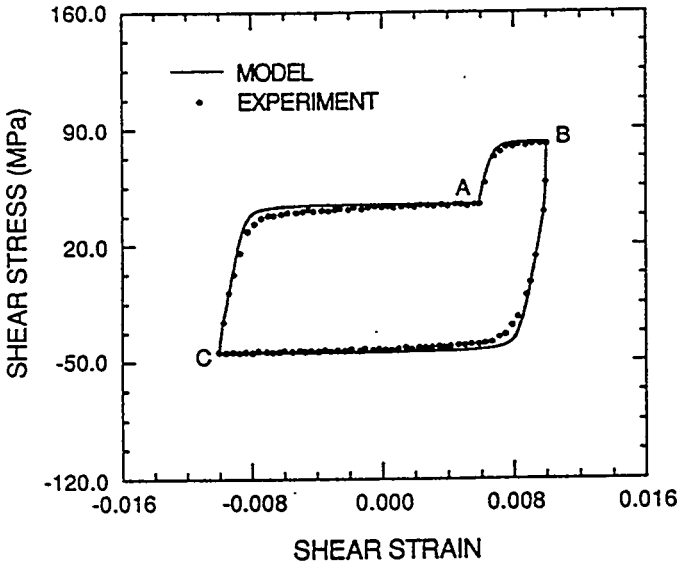

Fig. 1. Self-consistent prediction of polycrystal response.

SELF CONSISTENT METHOD

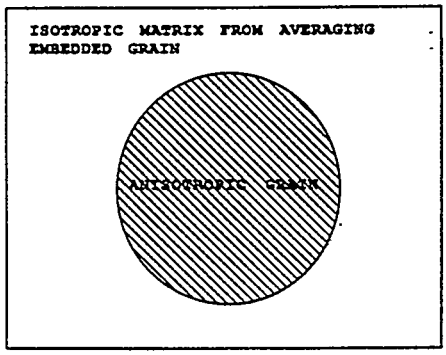

Fig. 2. Self-consistent grain embedded in effective medium.

IMPLICIT MODEL, ITERATION REQUIRED

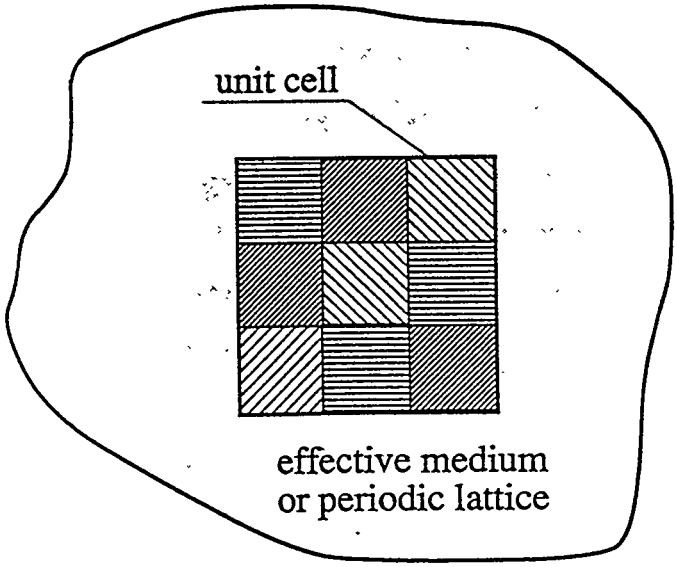

Fig. 3. Nine grains of random orientation in unit cell embedded in either an effective medium or an infinite periodic lattice.

incremental scheme is adopted, the method is explicit for all quantities except the effective isotropic elasticity tensor, D^0_{ijkl}. The self-consistent method which produced Fig. 1 is embodied in the following incremental equations [4]:

$$\Delta\sigma_{ij}(\eta,\beta,\phi) = D_{ijkl}(\eta,\beta,\phi)\left(\Delta\varepsilon^{\mathrm{T}}_{kl}(\eta,\beta,\phi) - \Delta\varepsilon^{\mathrm{P}}_{kl}(\eta,\beta,\phi)\right) \tag{1}$$

and

$$\begin{aligned}\Delta\varepsilon^{\mathrm{T}}_{ij}(\eta,\beta,\phi) = &\left[I_{ijmn} + S_{ijef}\left(D^0_{efpq}\right)^{-1}\left(D_{pqmn}(\eta,\beta,\phi) - D^0_{pqmn}\right)\right]^{-1} \times \\ &\times \left\{\Delta\varepsilon^0_{mn} + S_{mnkl}\left(\Delta\varepsilon^{\mathrm{P}}_{kl}(\eta,\beta,\phi) - \overline{\Delta\varepsilon^{\mathrm{P}}_{kl}}\right) + \right. \\ &\left. + S_{mnkl}\left(D^0_{kluv}\right)^{-1}\left(D_{uvrs}(\eta,\beta,\phi) - D^0_{uvrs}\right)\Delta\varepsilon^{\mathrm{P}}_{rs}(\eta,\beta,\phi)\right\},\end{aligned} \tag{2}$$

where S_{ijkl} are the Eshelby tensor components which are calculated from the components of the elasticity tensor, D^0_{ijkl}, for the effective medium in which the spherical grain is embedded. The tensor components $D_{ijkl}(\eta,\beta,\phi)$, $\Delta\varepsilon^{\mathrm{T}}_{ij}(\eta,\beta,\phi)$ and $\Delta\varepsilon^{\mathrm{P}}_{ij}(\eta,\beta,\phi)$ represent the elasticity tensor and the total and viscoplastic strain increments in the global coordinate system—to which strains in the polycrystal are referred—and (η,β,ϕ) are the Euler angles which locate the orientation of the grain's crystallographic axes with respect to the global system of the polycrystal. Finally, the components $\overline{\Delta\varepsilon^{\mathrm{P}}_{ij}}$ represent the angle average of the viscoplastic strain increment, viz.,

$$\overline{\Delta\varepsilon^{\mathrm{P}}_{ij}} = \left\langle\Delta\varepsilon^{\mathrm{P}}_{ij}(\eta,\beta,\phi)\right\rangle = \frac{1}{8\pi^2}\int_0^{\pi}\int_0^{2\pi}\int_0^{2\pi}\Delta\varepsilon^{\mathrm{P}}_{ij}(\eta,\beta,\phi)\,\sin\eta\,d\eta\,d\beta\,d\phi, \tag{3}$$

where the viscoplastic strain increment, $\Delta\varepsilon^{\mathrm{P}}_{ij}(\eta,\beta,\phi)$, is obtained by integrating a viscoplastic constitutive model [1,5] for the single crystal material based on crystallographic slip theory. The preceding equations allow the stress, strain and viscoplastic state variable histories in the grain to be updated after each load step. By equating the elastic and viscoplastic portions of the overall equation governing the constitutive behavior of the polycrystal, viz.,

$$\Delta\sigma^0_{ij} = D^0_{ijkl}\left(\Delta\varepsilon^0_{kl} - \overline{\Delta\varepsilon^{\mathrm{P}}_{kl}}\right), \tag{4}$$

we find that [4]

$$D^0_{ijkl} = \left\langle D_{ijrs}(\eta,\beta,\phi)\left[I_{rskl} + S_{rspq}\left(D^0_{pqmn}\right)^{-1}\left(D_{mnkl}(\eta,\beta,\phi) - D^0_{mnkl}\right)\right]^{-1}\right\rangle \tag{5}$$

and

$$\begin{aligned}\overline{\Delta\varepsilon^{\mathrm{P}}_{ij}} = &\left[D^0_{ijpq}\left(S_{pqrs} - I_{pqrs}\right)\right]^{-1}\left\langle D_{rsuv}(\eta,\beta,\phi)\times\right. \\ &\times\left[I_{uvgh} + S_{uvef}\left(D^0_{efmn}\right)^{-1}\left(D_{mngh}(\eta,\beta,\phi) - D^0_{mngh}\right)\right]^{-1}\times \\ &\left.\times\left(S_{ghkl} - I_{ghkl}\right)\Delta\varepsilon^{\mathrm{P}}_{kl}(\eta,\beta,\phi)\right\rangle,\end{aligned} \tag{6}$$

in which the angle brackets denote angle averaging according to equation (3). This model, which clearly idealizes the actual geometry, made excellent predictions of the average response as shown in Fig. 1. Further predictions are presented in [4] and [5].

In the second part of this project this model has been used to predict the grain to grain heterogeneity. Because neighboring grain effects are represented only in an average sense, it is expected that the self-consistent model will underestimate the degree of heterogeneity of the mechanical response. For that reason a second, more complex, model has also been developed.

The second model represents a finite number of individual two-dimensional grains explicitly. These grains may be embedded in either an effective medium or in a repeating periodic array of grain patches. This model is more completely described in several of the authors papers [7,8,9,11,29]. Two variants of the method have been developed: one based on Fourier series and a second variant based on Green's functions. The Green function method can be derived from the Fourier series method using a Poisson sum procedure. Figure 3 show a representative model of a group of randomly orientated grains that in this particular case are chosen to be square. The method starts with an exact integral equation based on known Green's functions. The equations are than solved approximately by dividing the body into subvoloumes. The strain increment in each subvolume is assumed to be constant. This constant strain increment is the volume averaged value of the exact strain field over the subvolume. In the resulting equations there appear geometric integrals which have been solved in closed form for squares, rectangles, and recently for triangles [11]. By using the known closed form representation of these integrals, the computational effort needed to calculate the stresses and strains in the unit cell has been much reduced. The complete details of the method are given in [7,8,9,11,29]. The key governing integral equation has the following form:

$$\Delta\varepsilon^{\mathrm{T}}_{kl}(\mathbf{r}) = \Delta\varepsilon^{0}_{kl} + \iiint_{V} U_{klmn}(\mathbf{r}-\mathbf{r}')\,\Delta\varepsilon^{*}_{rs}(\mathbf{r}')\,dV(\mathbf{r}') - \\ - \frac{1}{V_c}\iiint_{V_c} dV(\mathbf{r}) \iiint_{V} U_{klmn}(\mathbf{r}-\mathbf{r}')\,\Delta\varepsilon^{*}_{rs}(\mathbf{r}')\,dV(\mathbf{r}')\,, \tag{7}$$

in which the eigenstrain increment is defined by the relation

$$\Delta\varepsilon^{*}_{mn}(\mathbf{r}') = D^{\mathrm{m}}_{mnrs}\Delta\varepsilon^{\mathrm{P}}_{rs}(\mathbf{r}') - (D^{\mathrm{c}}_{mnrs} - D^{\mathrm{m}}_{mnrs})\left[\Delta\varepsilon^{\mathrm{T}}_{rs}(\mathbf{r}') - \Delta\varepsilon^{\mathrm{P}}_{rs}(\mathbf{r}')\right], \tag{8}$$

and where D^{c}_{mnrs} and D^{m}_{mnrs} denote the elasticity components of the crystal and an effective reference matrix material, respectively. The tensor components U_{klmn} involve the second spatial derivatives of the Green function for the reference matrix material.

This method has proven to be computationally efficient for small example problems. For example, the calculation of the transverse stresses in the 7×7 array of subvolumes shown in Fig. 6 takes only a few seconds on a Sun Sparc II workstation.

MEASURES OF HETEROGENEITY

The preceding models and the experimental techniques to be described next will be used to determine individual grain strains for grains of various orientations and with different near neighbor situations. We are interested in histograms of the stresses and in their extreme values. Extreme values are expected to govern the onset of fatigue and are of special interest. The stress in a grain is characterized by six independent components of the stress tensor. One must choose one or more specific measures of grain response when

plotting histograms. We have chosen to use stress and strain quantities volume averaged over each grain. We will later look at strain and stress variation within the grains. We have chosen to use two non-dimensional measures of individual grain strains as follows:

1. For uniaxial loading consider the stress (or strain) in the grain in the primary loading direction divided by the average applied stress (strain). We will call this the normalized pull stress.

2. For the case of crystallographic slip we may focus attention on the maximum resolved (Schmid) shear stress on potentially active slip systems divided by the average maximum principal shear stress. We will call this the normalized crystallographic shear stress.

We plan to compare computed and experimentally measured histograms of the two non-dimensional grain response measures and also to compare measured and calculated extreme values of these quantities.

PROPOSED EXPERIMENTS

Throughout this program a single phase, solution strengthened nickel base alloy, Hastelloy-X, has been used. This material was chosen because it was available not only in polycrystalline form, but also in large single crystals made specially for us by courtesy of Pratt & Whitney. In developing the single crystal constitutive model and in generating data to check our ability to predict the overall response, the tension-torsion test system built at the University of Connecticut was used. To enable individual grain strains to be measured, special large grained (1 to 2 mm) Hastelloy-X specimens have been made by growing grains from 0.02 mm up to about 2 mm in size via a 30 hour, 1240° C, heat treatment. This heat treatment was developed through a series of about a dozen trial heat treatments. The coarse grained material is now being machined into test specimens for use in the Moiré and neutron diffraction experiments.

Moiré strain analysis is a full field, high spatial resolution, strain measuring method capable of giving full field information about strains within the 2 mm grains of our sample. These experiments are to be performed at INEL by Dr. Epstein and Dr. Reuter. The data collected will allow a reasonable number of individual surface grain strains to be determined at room temperature for both elastic and plastic loadings. Histograms will be constructed for comparison with calculations.

Neutron diffraction experiments will also be carried out in which lattice parameters will be measured at various loads for both elastic and plastic conditions. These experiments will sample both surface grains and internal grains and will provide measures of the stress, rather than the strain, as obtained in the Moiré experiments. Accordingly, these experiments will complement the Moiré experiments. These novel and challenging experiments will be done by directing a pulsed neutron beam from the Argonne Pulsed Neutron Source (IPNS). This apparatus produces diffraction spectra from polyenergetic neutrons having a variety of DeBroglie wavelengths. The beam size is such that, typically, the spectra from five grains will be obtained simultaneously. The challenge will be to sort out the spectra unambiguously. Multiple detector banks are expected to aid in this process. These experiments will be conducted by Dr. Jordan (U. Conn) and Drs. Richardson and Kupperman of Argonne. These experiments will provide histograms of stress for comparison

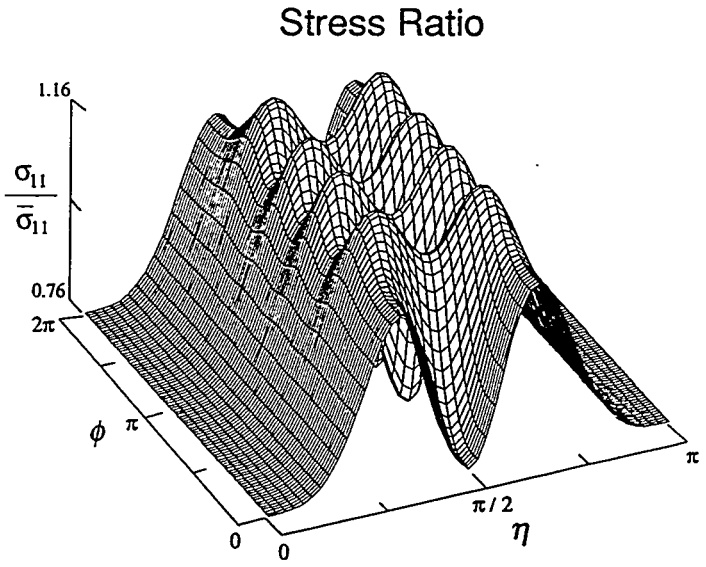

Fig. 4. Maximum and minimum stress ratio in self-consistent grains.

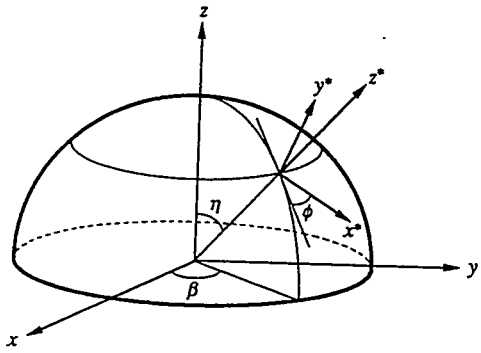

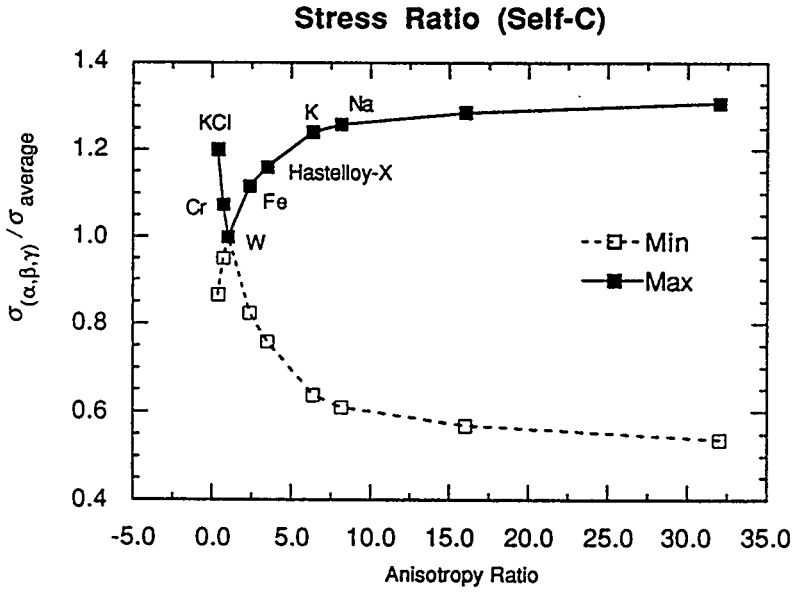

Fig. 5. Stress ratio for different materials versus Zener parameter.

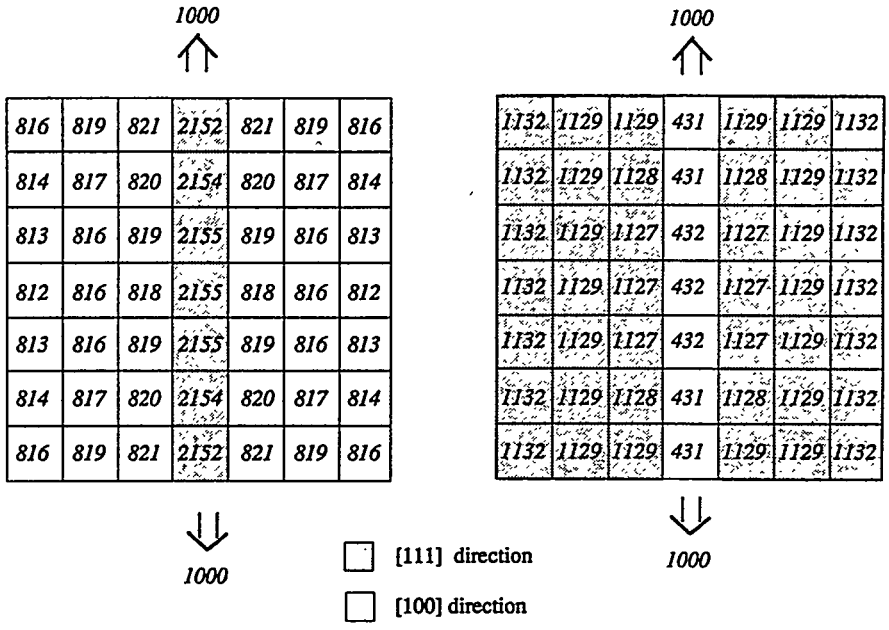

Figs 6a, 6b. Transverse stresses in a unit cell surrounded by eight nearest neighbors comprised of identical unit cells.

with calculation. Samples have just been successfully fabricated and the experiments will be conducted this summer.

COMPUTED RESULTS

The variation of normalized pull stress as a function of the Euler angles defining the grain orientation is shown in Fig. 4. For simple pull experiments only 2 of 3 possible Euler angles matter. Figure 5 shows the extreme value of normalized stress for various materials as a function of the Zener parameter, $(D_{1111} - D_{1122})/2D_{1212}$, which is a measure of the degree of anisotropy of the material.

The integral equation model has been run for elastic crystal arrays as shown in Fig. 3, in which only one subvolume per grain is used. Many cases have been run. Here we will mention two of the more interesting ones. Two thousand 7×7 grain arrays were run for a total of 100,000 grains and the extreme values of the normalized pull stress were retained. The values were found to be 1.5 and 0.7. For comparison, the special arrangement of Figs 6a and 6b were run, yielding normalized pull stress extreme values of 2.1 and 0.6. These values may be compared to the self-consistent spherical grain values of 1.2 and 0.8. This series of trials shows that the self-consistent model, as expected, underestimates the extreme values. The highly unlikely configuration of Fig. 6 shows that in discussing extreme values, very low probability arrangements—as in Fig. 6—yield extreme values. The numbers in Figs 6a and 6b represent the transverse stresses in a unit cell when the structure is loaded "at infinity" with an overall transverse stress, perpendicular to the two-dimensional grains, of 1000 kPa. The orientation of the single crystal grains with respect to the global axes are denoted by the clear and shaded regions in the figures.

CONCLUSIONS

1. The self-consistent model was able to accurately predict the overall average response of the polycrystal experiments from single crystal properties, using no adjustable parameters.

2. Prediction of heterogeneity using the self-consistent model significantly underestimates heterogeneity.

3. More extreme heterogeneity was produced by constructing a special, highly improbable, configuration of grains. This special configuration was significantly more extreme than the most extreme result from 100,000 random grains. These results support the notion that the histogram of normalized stresses has extreme values at very low probabilities.

WORK PUBLISHED UNDER DOE PROGRAM

The following papers/reports have been published and document the work performed under the DOE program on the title and allied subjects. Dr. Oscar P. Manley served as contract monitor.

1. "A Viscoplastic Model for Single Crystals," ASME J. Eng. Mat. Tech., Vol. 114, pp. 19–26, 1992.

2. "A Micromechanical Viscoplastic Stress-Strain Model," Proceedings of 8th Symposium on Energy Engineering Sciences, Micro/Macro Studies of Multiphase Media, May 9–11, Argonne National Laboratory, Report No. CONF–9005183, 1990.

3. "Critical Experiments on the Self-Consistent Model for Polycrystalline Hastelloy-X," **Modeling of the Deformation of Crystalline Solids**, Eds. T. Lowe, T. Rollett and P. Follansbee, TMS publications, p. 601, 1991.

4. "Self-Consistent Constitutive Modelling and Testing of Polycrystalline Hastelloy-X," Int. J. Solids Structures, Vol. 29, pp. 2623–2638, 1992.

5. "The Viscoplastic Behavior of Hastelloy-X Single Crystal," Int. J. of Plasticity, Vol. 9, pp. 119–139, 1993.

6. "Asymptotic Integration Algorithms for Nonhomogeneous, Nonlinear, First Order Ordinary Differential Equations," NASA TM 103793, 1991.

7. "Nonlinear Mesomechanics of Composites with Periodic Microstructure," NASA TM 102051, 1989.

8. "Equivalence of Green's Function and the Fourier Series Representation of Composites with Periodic Microstructure," pp. 535–558 of the book, **Micromechanics and Inhomogeneity. The Toshio Mura Anniversary Volume**, Springer-Verlag, 1990.

9. "Microstress Analysis of Periodic Composites," Composites Engineering, Vol. 1, No. 1, pp. 29–40, 1991.

10. "Steady State and Transient Zener Parameters in Viscoplasticity: Drag Strength Versus Yield Strength," Appl. Mech. Rev., Vol. 43, pp. S328–S337, 1990.

11. "Thermoviscoplastic Analysis of Fibrous Periodic Composites using Triangular Subvolumes," Composites Science & Technology, in press, 1993.

12. "Exponential Integration Algorithms for First Order Ordinary Differential Equations," NASA TM 104461, presented at the symposium COMPLAS III in Barcelona, Spain, 6–12 April, 1992.

13. "On the Thermodynamics of Stress Rate in the Evolution of Back Stress in Viscoplasticity," NASA TM 103794, 1991.

14. "Viscoplasticity with Creep and Plasticity Bounds," Int. J. Plasticity, Vol. 9, pp. 213–242, 1993.

15. "A Viscoplastic Theory with Thermodynamic Considerations," Acta Mech., Vol. 90, pp. 155–174, 1991.

16. "Viscoplastic Model Development with An Eye Towards Characterization," submitted to ASME J. Eng. Mat. Tech., 1992.

17. "Asymptotic Integration Algorithms for First-Order ODEs with Application to Viscoplasticity," NASA TM 105587, 1992.

18. "From Differential to Difference Equations for First-Order ODEs with Application to Viscoplasticity," NASA TM 104530, 1991.

19. "An Overview of Self-Consistent Methods for Fiber Reinforced Composites," NASA TM 103713, 1991.

20. "Investigation of Effective Material Properties for Viscoplastic Fibrous Composites Using the Self-Consistent and Mori-Tanaka Methods," in **High Temperature Constitutive Modeling—Theory and Application**, Editors: A.D. Freed and K.P. Walker, Book No. H00667, pp. 439–449, 1991.

21. Co-editor with A.D. Freed of **High Temperature Constitutive Modeling—Theory and Application**, ASME Book No. H00667, 1991.

22. "A New Uniformly Valid Asymptotic Integration Algorithm for Elasto-Plastic Creep and Unified Viscoplastic Theories Including Continuum Damage," Int. J. Num. Methods Eng., Vol. 32, pp. 385–418, 1991.

23. "A Viscoplastic Model with Application to LiF–22%CaF_2 Hypereutectic Salt," NASA TM 103181, 1991.

24. "Model Development in Viscoplastic Ratchetting," NASA TM 10259, 1990.

25. "Ratchetting Behavior in Viscoplasticity. A Technical Note," Eur. J. Mech., A/Solids, Vol. 12, No. 1, pp. 1–6, 1993.

26. "Three-Dimensional Deformation Analysis of Two-Phase Dislocation Substructures," Scripta Metallurgica et Materialia, Vol. 27, pp. 233–238, 1992.

27. "Dislocation Substructure Viscoplasticity," to be presented at the Seventh Japanese Institute of Metals International Symposium (JIMIS–7) **Aspects of High Temperature Deformation and Fracture in Crystalline Materials**, to be held in Nagoya, Japan on July 28–31, 1993.

28. "Stress Versus Temperature Dependence of Activation Energies for Creep," ASME J. Eng. Mat. Tech., Vol. 114, pp. 46–50, 1992.

29. "Accuracy of the Generalized Self-Consistent Method in Modelling the Elastic Behavior of Periodic Composites," American Society of Mechanical Engineers, AMD-Vol. 150/AD–Vol. 32, **Damage Mechanics in Composites**, Editors: D. H. Allen and D. C. Lagoudas, Book No. G00752, pp. 107–131, 1992. An expanded version is in press, in Phil. Trans. R. Soc. Lond., Series A, 1993.

30. "Fourier Integral Representation of the Green Function for an Anisotropic Elastic Half-Space," in press, in Proc. R. Soc. Lond., Series A, 1993.

31. "Extending the Theory of Creep to Viscoplasticity," under review, in ASME J. Press. Vessel Tech., 1993.

FULLY PLASTIC FRACTURE MECHANICS FOR PLANE STRAIN CRACK GROWTH

F.A. McClintock, Y.J. Kim, and D.M. Parks
Massachusetts Institute of Technology
Cambridge, Massachusetts 02139, U.S.A.

ABSTRACT

A theoretical framework is given for designing possibly cracked structures to remain ductile under accidental overloads. For non-hardening, fully-plastic plane strain crack growth in a number of geometries and loadings, near tip fields are characterized by three parameters: the slip line angle θ, and the normal stress σ, and shear displacement δu, across the slip line. These parameters are found in terms of the far-field geometries and loadings through slip line fields or least upper bound analyses based on circular arcs. Then the crack growth criterion in terms of the crack tip opening angle ($CTOA$) is proposed as a function of near tip parameters and material properties. Experiments are suggested to determine the dependence of the $CTOA$ on those variables.

INTRODUCTION

Under monotonic loading, structures should ideally be ductile, in order to provide both a warning before initial crack growth and continued resistance during crack growth. Such fully plastic behavior is of interest in design against collisions, tank car accidents, earthquakes, and ship groundings.

For brittle structures in tensile (Mode I) loading across a crack, only a criterion for initial growth is needed, because the crack is immediately unstable. The criterion is based on the discovery in the 1950's that there can be a region around the crack tip, large compared to either a plastic zone or to the microstructural fracture process zone, and small compared to the distance to the next nearest boundary, in which the stress and strain are uniquely defined in terms of a single parameter, the stress intensity factor K_I (see [1]). At a critical value for a given material, K_{IC}, the crack begins to grow unstably. (At lower values of K_I, the growth is negligible unless loading is repeated thousands of times as in fatigue.) The value of the applied K_I is determined from the far-field geometry and loading [2,3]. Thus for a brittle structure (one with a crack tip plastic zone small compared to any characteristic dimension of the part or to a crack in it), unstable crack growth occurs under the local condition

$$K_I(\text{geometry and loading}) \geq K_{IC}(\text{material}). \tag{1}$$

For more extensive plastic flow around a crack in a structure, it was found in the 1960's that for power-law strain hardening with $\sigma = \sigma_1 \epsilon^n$ and with a sufficiently high strain hardening exponent n, the stress and strain fields around a crack tip are characterized by another coefficient J, such that stable crack growth occurs under the local condition

$$J_I(\text{geometry, loading}, \sigma_1, n) \geq J_{IC}(\text{material}). \tag{2}$$

For crack growth large compared to the region in which a J-field dominates, the J-concept is no longer valid because it would have to be based on the current crack tip, and would not include the prior history which has left residual stresses and strain-hardening.

Asymptotic solutions have been found for an elastic-plastic growing crack, but the region in which the fracture strain dominates the yield strain turn out to be of sub-atomic size for the low strength alloys of interest here (see [4]).

For initial growth, the singular expansions giving the first-order coefficients K and J have been extended to higher stress levels (toward general yield) by including second-order coefficients T or Q [5,6], but the difficulties with finite crack growth remain.

For fully plastic flow in the limiting case of a vanishingly small strain hardening exponent n, the governing equations become hyperbolic, unique singular solutions do not exist, and the effects of far-field loading and geometry penetrate all the way to the crack tip in many cases [7]. For ductile alloys, elastic strains are negligible, and the fields of strain increments and stress for growing cracks are the same as for stationary cracks. The strain fields are then found by superposition of the strain increments for successive crack tip positions. Thus the known slip line fields for stationary cracks are applicable to growing cracks. The distortion of non-hardening fields by strain hardening is less in growing than in stationary cracks, because the advance of the fields through the material smooths out the discontinuities. Even in annealed aluminum, with a ratio of tensile to yield strength of 2.5, the deformation field around a growing crack (shear bands around a rigid wedge in front of the crack) shows a strong resemblance to the non-hardening field (see [8], p. 378).

Here we review the extension of fracture mechanics to the limiting case of non-hardening, plane strain crack growth. It turns out that for Mode I loading, many of the infinite variety of non-hardening stress and strain fields can be usefully approximated by just three parameters. (For unsymmetrical fields, see [9].) While three parameters are more than for brittle structures or for the ductile initiation of crack growth discussed above, this theory should provide a guide for the design of crack-resistant structures of common low-strength alloys.

NEAR-TIP FIELD CHARACTERIZATION FROM SLIP LINE FIELD ANALYSIS

Fields of stress and displacement increments for cracked structures of rigid-plastic, non-hardening materials have been found for a variety of geometries and loadings (see [7,10]). At the crack tip, a number of these fields consist simply of a pair of slip lines surrounded by rigid regions, e.g., the single-face-cracked specimens under bending (Fig. 1a). Other fields consist of a pair of deforming fans surrounded by regions with less concentrated plastic flow, e.g., the doubly grooved specimens under tension (Fig. 1b). To simplify the problem, regard the deformation in the fan at the crack tip as being concentrated on a single slip line which is surrounded by rigid regions.

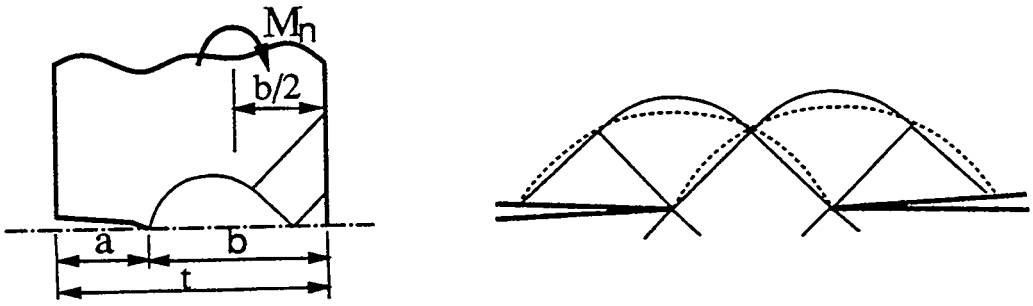

Fig. 1. Slip line fields (a) for a deep, single-face-cracked plate under pure bending, and (b) a symmetric doubly-cracked plate in tension.

For symmetric geometry and loading, the near tip fields are now characterized by just three parameters: the slip line angle θ_s and the normal stress σ_s and shear displacement δu_s across the slip line. This three-parameter characterization of near tip fields in fully plastic fracture crack

growth mechanics presents a contrast to the one-parameter (K) in elastic fracture mechanics or the two-parameter (K or J and T or Q) characterization in linear or non-linear elastic fracture mechanics.

If pairs of slip lines are available for the problem at the hand, they describe a local field, (as does K) as a function of loading and geometry:

$$\left\{ \begin{array}{c} \theta_s \\ \sigma_s \\ \delta u_s \end{array} \right\} = \left\{ f \right\} (\text{far-field geometry, loadings, and their increments}). \tag{3}$$

Now consider forms of (3) for cases in which the slip line fields are not available or are more complicated than pair of slip lines.

NEAR-TIP FIELD CHARACTERIZATION FROM LEAST UPPER BOUND ANALYSIS

Finding θ_s and δu_s

The least upper bound (LUB) field with a circular arc provides an estimate not only of the limit load, but also of the slip plane angle θ_s and displacement δu_s, all in terms of far-field geometry and loadings. For example, consider a single-face-cracked plate with shear strength k, subject to combined bending and large tension (Fig. 2a). For given net section shear $V_n(=0)$ and tension N_n, the LUB to the moment M_n can be found by minimizing M_n determined from relative sliding along the circular arc with respect to two independent arc parameters, α and β. The yield locus from the LUB analysis is shown in Fig. 2b, including that where slip line fields are known [11]. Figure 2b also includes results from finite element limit analysis by Lee and Parks [12]. For predominant bending ($0 \leq N_n/(2kb) < 0.55$), FEM results are consistent with the SLF solutions. For combined bending with large tension ($0.55 \leq N_n/(2kb) \leq 1.0$), the locus from the LUB analysis is no more than 3% above the FEM results.

The LUB field also provides δu_s (or the crack tip opening displacement increment $\delta CTOD$) in terms of far field increments of displacement δu and rotation $\delta\theta$ (Fig. 2a):

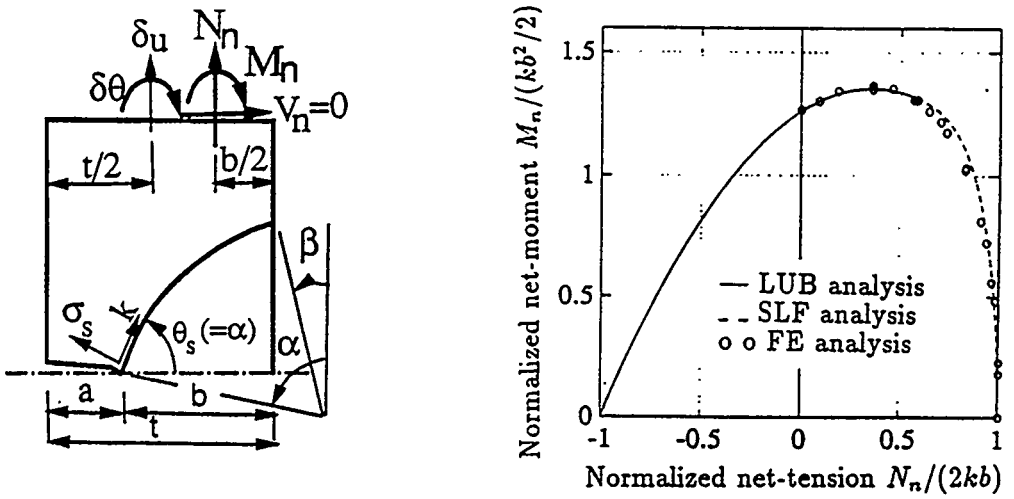

Fig. 2. (a) Circular arc for an upper bound in a deep, single-face-cracked specimen under combined bending and large tension, and (b) limit loads from the least upper bound field and FEM results.

$$\delta u_s \left(= \frac{\delta CTOD/2}{\sin\theta_s} \right) = \frac{1}{\sin\theta_s} \left[\delta u + (\frac{t}{2} - a)\delta\theta \right]. \tag{4}$$

Finding σ_s

It is very difficult to glean information on the local stress from lower bound stress fields satisfying equilibrium, the yield condition, and traction boundary conditions. We show here a new method of approximating σ_s from the least upper bound.

Consider rigid-body rotation across a circular arc extending from a crack tip across a ligament of width b in a plate with shear strength k (Fig. 3), subject to general loading with three components: V, N, and M. Suppose that two loading components are specified and that the circular arc for the LUB to the unspecified loading component has been found. Along the arc, the shear component of traction is k. Then the following theorem holds, as proven in [13].

Assume that the normal component of traction, σ, on the LUB arc satisfies the first Hencky equation of equilibrium with one unknown (the reference stress σ_r) evaluated at $\psi = 0$:

$$d\sigma = 2kd\psi \quad or \quad \sigma = \sigma_r + 2k\psi. \tag{5}$$

Then if σ_r is chosen to satisfy force equilibrium in any other than the chordal direction (the 1-direction in Fig. 3), the tractions on the LUB arc satisfy global equilibrium.

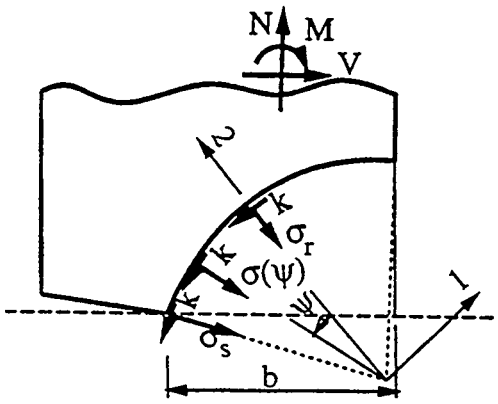

Fig. 3. Kinematically admissible plane strain deformation field consisting of rigid-body rotation across a circular arc in a cracked plate.

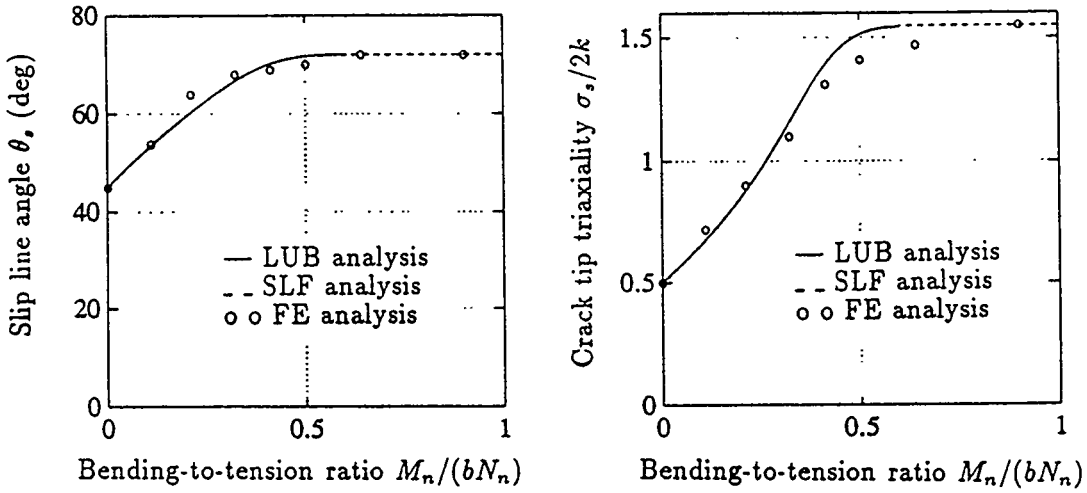

Fig. 4. Near tip slip angle θ_s and crack tip stress triaxiality $\sigma_s/(2k)$ for deep, single-face-cracked plates under combined bending and tension.

The normal stress across the LUB arc at the crack tip, σ_s, can be approximated from the Hencky equation (5) with the determined reference stress σ_r. Therefore the LUB arc provides an approximation to the stress and deformation fields at a crack tip, consistent with global equilibrium.

To test accuracy with an example, consider again the single-face-cracked plate under combined bending and large tension (Fig. 2a), for which exact slip line field solutions are not known but finite element results are available [12]. (As shown in Fig. 4 for various bending-to-tension ratios, at the ends of the curves where SLF results are available, θ_s and $\sigma_s/2k$ are consistent with the SLF values, except that $\sigma_s/2k$ is 5% low at $M_n/(bN_n) = 0.64$.) For bending with large tension, the LUB values of θ_s and $\sigma_s/2k$ appear accurate within 5%. The accuracy of the third parameter, δu_s, is not available from the FEM results, but for pure tension and for the modified Green and Hundy field with $M_n/(bN_n) = 0.60$, δu_s from the LUB is exactly that from the SLF. (This agreement is somewhat coincidental, because for pure bending δu_s from the LUB is 1.4 times that from the SLF.)

The accuracy of the LUB analysis has also been considered for three cases with known SLF [13]. For a single-face-cracked plate in pure shear, θ_s from the LUB analysis is zero compared to $\pm 8.2°$ from the SLF analysis; $\sigma_s/2k$ is zero compared to ± 0.14, and δu_s is exact. For a three-point bend plate with a total length to ligament ratio of 6, θ_s from the LUB analysis is 56° compared to 68°; $\sigma_s/2k$ is 1.06 compared to 1.22, and δu_s is 2.4 times the SLF value for the same end displacements. As here, the agreement is worst with fields involving constant state regions or fans. For the classical double-face-cracked plate in tension, the fan runs from 45° to 135° with $\sigma_s/2k$ falling from 2.1 to 0.5; θ_s from the LUB analysis comes in at a reasonable $\theta_s = 68°$, but $\sigma_s/2k$ is high at 2.54, δu_s is low by a factor of 0.5 to 0.67, depending on whether the Prandtl, Hill, or Neimark displacement field is used for comparison. In this case, improved agreement would require more parameters in the fracture criterion. In other cases, values from the LUB analysis might be improved by extend the LUB fields to include constant deformation fields, as well as arcs.

CRACK GROWTH CRITERION

With the local field characterized by θ_s, σ_s, and δu_s, we turn to the response of the material by crack growth δa in terms of those parameters. The response can be expressed in terms of the crack tip opening angle $CTOA$:

$$\delta a(\theta_s, \sigma_s, \delta u_s) = \frac{\delta u_s \sin\theta_s}{\tan(CTOA/2)}, \quad \text{where } CTOA(\theta_s, \sigma_s, \text{material}). \tag{6}$$

The functional form of $CTOA$ should ultimately be determined by experiment, just as is K_{IC}. Such experiments are outlined below, but for insight, first consider a micromechanical model.

A sliding off and shear-cracking model for a growing crack

Consider zig-zag crack growth, sliding off by s and cracking by c along a shear band before changing direction (Fig. 5). The geometry gives the form of $CTOA$ in terms of θ_s and s/c:

$$\tan\left(\frac{CTOA}{2}\right) = \frac{s\sin\theta_s}{(c+c+s)\cos\theta_s} = \frac{1}{2(c/s)+1}\tan\theta_s. \tag{7}$$

Geomtery also gives the relation between the fracture shear strain in the band γ_f, and s and c:

$$\gamma_f = \frac{s}{(s+c)\sin 2\theta_s}. \tag{8}$$

Eliminating (c/s) in (7) with (8) gives

$$\tan\left(\frac{CTOA}{2}\right) = \frac{1}{[2/(\gamma_f \sin 2\theta_s) - 1]}\tan\theta_s. \tag{9}$$

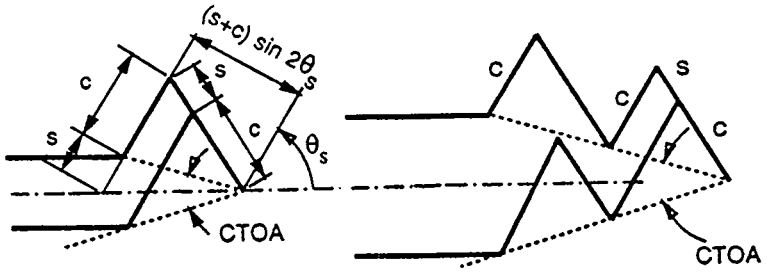

Fig. 5. Sliding off and shear cracking model for a growing crack.

Equation (9) gives the $CTOA$ in terms of θ_s and γ_f. The fracture strain γ_f will depend on the mean normal stress in the shear band, σ_s, and on material properties such as hardening and an initial volume fraction of holes, which will be discussed next.

Fracture strain in the shear band

Accounting for micromechanisms for crack growth such as hole nucleation, hole growth, and linkage by localization or fine cracking, McClintock et al. [4] proposed

$$\gamma_f = \frac{(1-n)A}{\sinh[(1-n)\sigma_s/k]} + B(\sigma_s), \tag{10}$$

where A and B are parameters and n is the strain hardening exponent in $k = k_o\gamma^n$ with k_o=constant. The first term on the RHS of (10) can be viewed as a strain for hole growth to linkage by localization or by fine cracking [14]. The second term, $B(\sigma_s)$, can be viewed as a strain for hole nucleation, which is generally a function of mean normal stress [15]. For preliminary insight, assume the nucleation strain is negligible ($B = 0$). Figure 6a shows an inverse exponential dependence on σ_s/k for non-hardening ($n = 0$) flow and for typical values of A, ranging from 0.2 to 1.2, along with limited available experimental data on $CTOA$ from the literature [16,17]. Hancock et al. [18] performed fully plastic (crack initiation and growth) tests providing a wide range of crack tip triaxiality: three point bending, compact tension, and center cracked panel (CCP) test. (Their CCP test specimens did not meet plane strain requirements, so the resulting crack tip triaxiality would be lower than that for single-face-cracked specimens in tension.) Their results also showed a dramatic decrease in $CTOA$ with increasing σ_s/k as in Fig. 6a. Figure 6b shows a higher order parabolic dependence on θ_s ($45° \leq \theta_s \leq 72°$) for non-hardening ($n = 0$) and for two values of $A = 1.0, 0.5$. Therefore, to a first order for small n, (9) with (10) suggests that the $CTOA$ has inverse exponential dependence

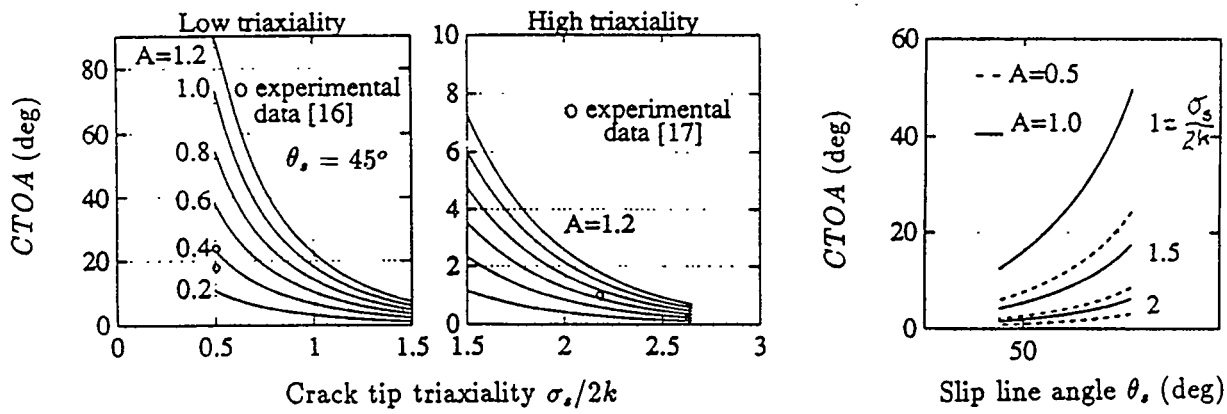

Fig. 6. Dependence of the estimated crack tip opening angle ($CTOA$) on $\sigma_s/(2k)$ and θ_s. Equation (9) and (10) with $n = 0$ and $B = 0$.

on σ_s/k and higher order parabolic dependence on θ_s for $45° \leq \theta_s \leq 72°$.

Note that (10) is analogous to K_{IC}(material), and therefore the parameters A and B in (10) reflect material properties and should be found from fully plastic crack growth experiments, as follows.

Suggested experimental determination of CTOA

The functional dependence of $CTOA(\theta_s, \sigma_s)$, on the parameters A and B of the fracture criterion of (9) with (10), can be found by fully plastic crack growth tests. For example, at $\theta_s = 45°$, $\sigma_s/2k$ can be increased from 0.5 to 1.547 in the unequally grooved specimens of Fig. 7a by decreasing the back-angle 2ϕ from 180° to 60° [7]. Solving (9) with (10) from the experimental data would allow fitting the constants A and B. For higher values of θ_s, consider the 4-point bending specimen of Fig. 7b. According to the SLF analysis [19], decreasing the back-angle 2ϕ from 180° to 90° would increase $\sigma_s/2k$ from 1.177 to 1.543 with θ_s nearly constant in the range from 67° to 72°. The constants A and B found from fitting these data should be the same as those from the unequally grooved tensile tests.

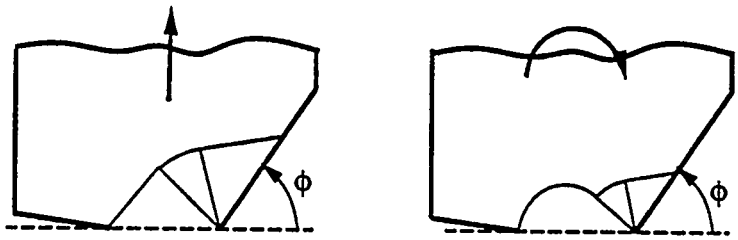

Fig. 7. Slip line fields for unequally grooved specimens (a) under pure extension, and (b) under pure bending.

CONCLUSION

For designing possibly cracked structures that must remain ductile under accidental overloads, we present a practical theory for fully plastic, plane strain crack growth. The one or two parameter characterization in linear or nonlinear elastic fracture mechanics must be extended to three parameters for the near tip fields of a growing crack in fully plastic, plane strain conditions: the slip line angle θ_s and the normal stress σ_s and shear displacement δu_s across the slip line. These parameters are found for the geometry and loading condition either from slip line field analysis or from least upper bound analysis based on a circular arc using only a programmable calculator. This is analogous, for example, to the K_I(geometry and loadings) of linear elastic fracture mechanics.

The material function analogous to K_{IC}(material) is expressed as the dependence of the crack tip opening angle ($CTOA$) on σ_s, θ_s and material properties. This dependence should be determined from fully plastic crack growth tests, which are suggested.

ACKNOWLEDGEMENT

This work was supported by the Office of Basic Energy Sciences, Department of Energy, under Grant DE-FG02-85ER13331 to M.I.T. and Contract DE-AS07-761D01670 with the Idaho National Energy Laboratory.

REFERENCES

1. M.F. Kanninen and C.H. Popelar, *Advanced Fracture Mechanics*, Oxford University Press, New York (1985).

2. H. Tada, P.C. Paris and G.R. Irwin, *The Stress Analysis of Cracks Handbook*, Paris Productions Inc., Saint Louis, MO (1985).

3. Y. Murakami, *Stress Intensity Factors Handbook*, Pergamon Press, Oxford (1987).

4. F.A. McClintock, Y.J. Kim and D.M. Parks, "Criteria for Fully Plastic, Plane Strain Crack Growth", *Int. J. Fracture* (submitted for publication).

5. D.M. Parks, "Advances in Characterization of Elastic-Plastic Crack-Tip Fields", in *Topics in Fracture and Fatigue*, Springer-Verlag, 59 (1991).

6. N.P. O'Dowd and C.F. Shih, "Family of Crack-Tip Fields Characterized by A Triaxiality Parameters - II. Fracture Application", *J. Mech. Phys. Solids* 40, 939 (1992).

7. F.A. McClintock, "Plasticity Aspects of Fracture", in *Fracture Vol. 3*, Academic Press, New York 47 (1971).

8. F.A. McClintock and A.S. Argon, *Mechanical Behavior of Materials*, Addison Wesley (1966).

9. F.A. McClintock, "Reduced Crack Growth Ductility Due to Asymmetric Configurations", *Int. J. Fracture* 42, 357 (1990).

10. B.B. Hundy, " Plane Plasticity", *Metallurgia* 49, 109 (1956).

11. M. Shiratori and B. Dodd, "Effect of Deep Wedge-Shaped Notches of Small Flank Angle on Plastic Failure," *Int. J. Mech. Sci.* 22 127, (1980).

12. H. Lee and D.M. Parks, "Fully Plastic Analyses of Plane Strain Single Edge Cracked Specimens Subject to Combined Tension And Bending", *Int. J. Fracture* (submitted for publication).

13. Y.J. Kim, F.A. McClintock and D.M. Parks, "Global Equilibrium of the Least Upper Bound Circular Arcs and its Application to Fracture Mechanics", *J. Mech. Phys. Solids* (submitted for publication).

14. F.A. McClintock, S.M. Kaplan and C.A. Berg, "Ductile Fracture by Hole Growth in Shear Bands", *Int. J. Fract. Mech.* 17, 201 (1966).

15. A.S. Argon, J. Im and R. Safoglu, "Distributuion of Plastic Strain and Negative Pressure in Necked Steel and Copper Bars", *Metallurgical Transcations*, 6A 815 (1975).

16. G.A. Kardomateas and F.A. McClintock, "Shear Band Characterization of Mixed Mode I and II Fully Plastic Fracture", *Int. J. Fracture* 40, 1 (1989).

17. F.A. McClintock and S.J. Wineman, "A Wedge Test for Quantifying Fully Plastic Fracture", *Int. J. Fracture* 33, 285 (1987).

18. J.W. Hancock, W.G. Reuter and D.M. Parks, "Constraint and Toughness Parameterized by T", to appear in *ASTM STP on Constraint Effects in Fracture, Proc. ASTM Symposium*, Indianapolis, IN (1991).

19. Y.J. Kim, "Modeling Fully Plastic Plane Strain Crack Growth", Ph.D. Thesis, Department of Mechanical Engineering, MIT, Cambridge, MA (in progress).

FRACTURE TOUGHNESS AS A FUNCTION OF CONSTRAINT FOR SIMULATED WELDMENTS

W. G. Reuter, W. R. Lloyd, and J. S. Epstein

Idaho National Engineering Laboratory
Idaho Falls, Idaho 83415 U.S.A.

ABSTRACT

One of the primary needs in structural design is the ability to predict structural integrity using fracture toughness data obtained from small, standard test specimens. Sufficient understanding of the fracture process in homogeneous, isotropic materials has been gained to extend the research into weldments, which are considered to be the primary region of fracture for structural components. Weldments have a great many parameters that influence fracture, and it is very difficult to isolate their effects on the fracture process. Specimens of a "model system" were fabricated to reduce this complexity. This paper provides preliminary results of fracture toughness testing of these simulated weldments.

INTRODUCTION

Fracture mechanics technology may be used in alloy development, in improving fabrication procedures, as a basis for purchasing materials, and to predict structural integrity. Predicting structural integrity is the purpose of the research described in this paper. Methods have been developed to predict some of the fracture process (crack growth initiation, subsequent crack growth, and failure) for homogeneous, isotropic materials. A schematic of the fracture process is shown in Figure 1. Structural design criteria may be based on one of these stages of fracture, such as initiation of crack growth (Point C); conditions associated with subcritical crack growth, e.g. the crack penetrating the wall thickness (in Region B); or failure (Point X). For each stage, very complex issues must be addressed, such as identifying the critical parameters that describe the fracture process and developing the ability to normalize these parameters as a function of specimen size, configuration, and loading.

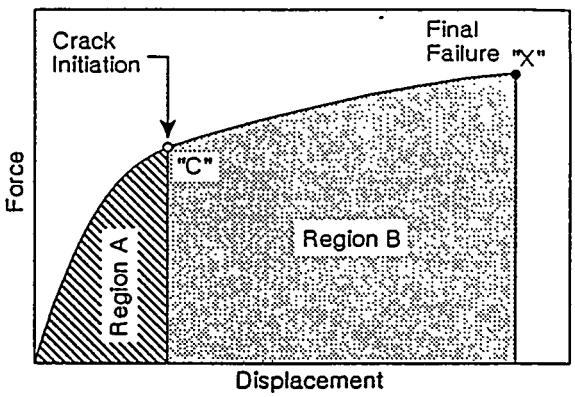

Figure 1 Schematic of Fracture Process

Research in this Idaho National Engineering Laboratory (INEL)/Massachusetts Institute of Technology (MIT) program has led to numerical capabilities, verified by experiment, for predicting crack growth initiation for a structural component based on test data generated from small, standard fracture toughness specimens.[1] Sufficient understanding of the fracture process in homogeneous, isotropic materials, as well as capabilities in both numerical analysis and experimental techniques, has been developed to extend the research into weldments. Weldments often contain defects and residual stresses and are considered to be the primary region of failure for structural components.

Weldments consist of a base metal, heat affected zone (HAZ), and a fusion zone, see Figure 2. These three regions each contain different microstructures; furthermore, the microstructure of the HAZ will range from coarse grained adjacent to the fusion line to fine grained near the base metal. Local changes in microstructure also occur due

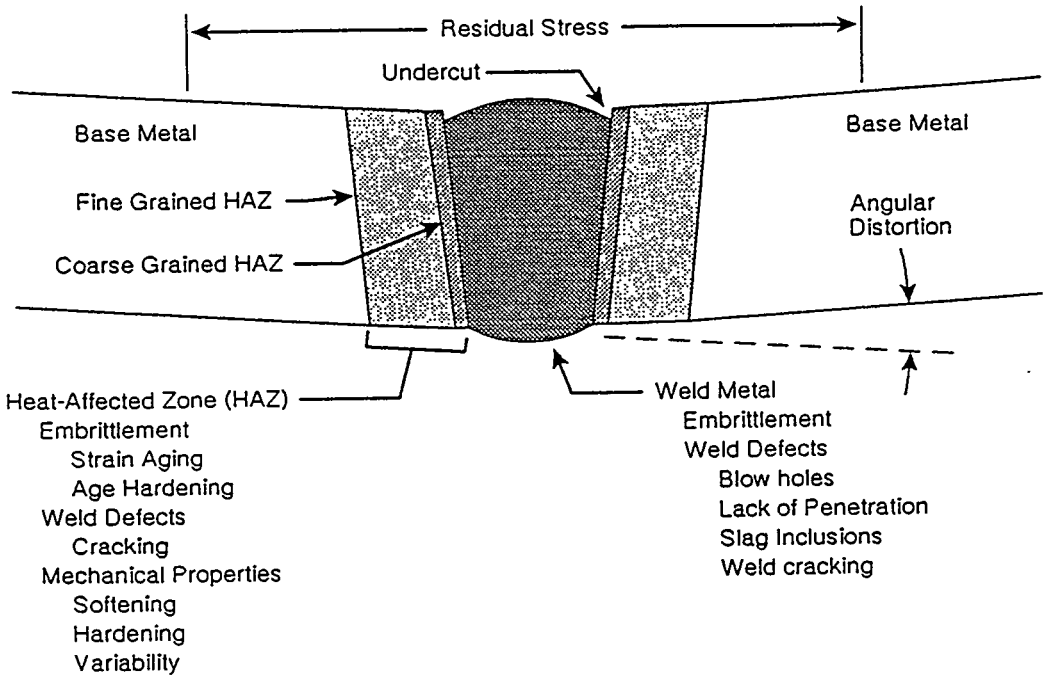

Figure 2 Diagram of a Weldment

to subsequent passes in a multipass welding process. The different microstructures generally exhibit different mechanical properties. Their nonhomogeneous nature puts weldments outside the realm for which fracture mechanics concepts have been developed. Some of the technology developed for homogeneous, isotropic base metal can be extended to weldments, but it is necessary to identify its limits of applicability.

Fracture toughness testing of as-welded Type 304 stainless steel (SS) was attempted at the INEL, but difficulties were experienced in producing acceptable fatigue precracks (too much crack front curvature), in placing the tip of the fatigue precrack in the microstructure of interest, and in performing single specimen unloading tests to measure J_{Ic}. (Various complications associated with fracture toughness testing of real weldments of Type 304 SS are reported in Graham et al.[2]) It was obvious that many parameters could influence the test results and that it would be very difficult to isolate their effect on the fracture process in weldments. Therefore, a model system of Ti-6Al-4V diffusion bonded to commercially pure Ti (CP Ti) was chosen for study. This paper provides preliminary results of fracture toughness testing of these simulated weldments.

EXPERIMENTAL APPROACH

Pieces of CP Ti 3.2, 6.4, or 12.7 mm thick were sandwiched between two pieces of Ti-6Al-4V and diffusion bonded. The mechanical properties of the two titanium alloys after the diffusion bonding cycles are provided in Table 1. Because the two materials have essentially the same elastic constants, it is assumed that very little residual stresses were generated during diffusion bonding. There are only very narrow zones at the interfaces where elements could diffuse; therefore, the "HAZ" in these simulated weldments is nonexistent. However, the yield strength of the weld metal is less than that of the base metal, so these specimens simulate "undermatched" welds.

SE(B) specimens, shown schematically in Figure 3, were machined from the diffusion-bonded pieces. The crack was located in the center of the weld. These specimens were tested using four-point bending to quantify the effect of constraint on the load-displacement curve, apparent J_{Ic} and dJ/da, and the extent of stable crack growth. The constraint has not yet been quantified for any specimen, but is assumed to range from a high for the "thinnest weld" (H = 3.2 mm, see Figure 3) to a low for the "thickest weld" (H = 12.7 mm). The constraint is due to the Ti-6Al-4V behaving as an elastic body that limits the ability of the CP Ti to deform.

Table 1

Mechanical Properties of Titanium Used for Diffusion Bonding[a]

	CP Ti	Ti 6Al-4V
Coefficient of thermal expansion, CTE (21 to 871°C)	10.3 x 10^{-6}/°C	10.3 x 10^{-6}/°C
Modulus of elasticity, E	112 GPa	123 GPa
0.2% offset yield strength, σ_o (also called σ_{ys})	366 MPa	886 MPa
Ultimate tensile strength, σ_{uts}	486 MPa	925 MPa
Strain-hardening coefficient, n	7.8	15
J_{Ic}	110 kJ/m^2	63 kJ/m^2

a. 3.45 MPa pressure at 870 to 900°C for 60 min in argon, followed by furnace cooling.

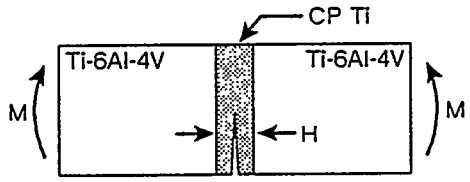

Figure 3 Schematic of Simulated Weldment Specimens

Moiré interferometry techniques were used to measure the displacement fields at the crack tip as a function of the applied load. These data will be compared with results of finite-element analyses.

TEST RESULTS AND DISCUSSION

Plots of moment versus bend angle (four-point bend test) are presented in Figure 4 for the three specimens tested to date. The specimen with H = 3.2 mm was able to carry the maximum load, which may be beneficial for a structural design controlled by plastic collapse. The J-Δa plots are summarized in Figure 5 and the estimated values of J_{Ic} and dJ/da are summarized in Table 2. The magnitude of the tunneling observed for all three specimens is such that test standards ASTM E 813 and E 1152 are not satisfied and a valid J_{Ic} cannot be measured, thus the energy density values given in Figure 4 and Table 2 are based on specimen dimensions and the total area under the applied moment versus bend angle curve. Although these energy density values are not true "J" values (based on ASTM E 813-89) and cannot be directly compared to J_{Ic} for the component materials, they are useful for comparison of the behavior of the three different specimens. It is expected that the tunneling will not have a significant effect on J_{Ic} but will affect dJ/da. Additional problems were encountered in identifying the appropriate flow stress for use with each constraint condition. It is apparent that for a thinner weld zone (H), "J_{Ic}" is lower, dJ/da is lower, and there is less stable crack growth. The decrease in J_{Ic} with increasing constraint is consistent with Reference 1. For a design based on fracture mechanics, the use of the smallest weld width is not considered to be beneficial.

Work of McClintock et al.[3] and of Kim et al.[4] shows a basis for concern about the ability of dJ/da to describe the crack growth process. This is especially true when Δa is greater than 2 to 3 times CTOD. Therefore, the fracture surfaces of the test specimens were examined using microtopography, a technique developed at the INEL to reconstruct the fracture process. With microtopography, CTOD at initiation of crack growth and CTOA as a function of crack growth (Δa) can be measured. The values of CTOD are presented in Table 2.

The increase in constraint due to reducing weld width led to: (1) a substantial increase in the load carrying capability, (2) a decrease in "J_{Ic}" and "$CTOD_{init}$", and (3) a significant reduction in dJ/da and in Δa associated with failure (or significant pop-in). For engineering applications, the reduction of the width of the weld metal may provide

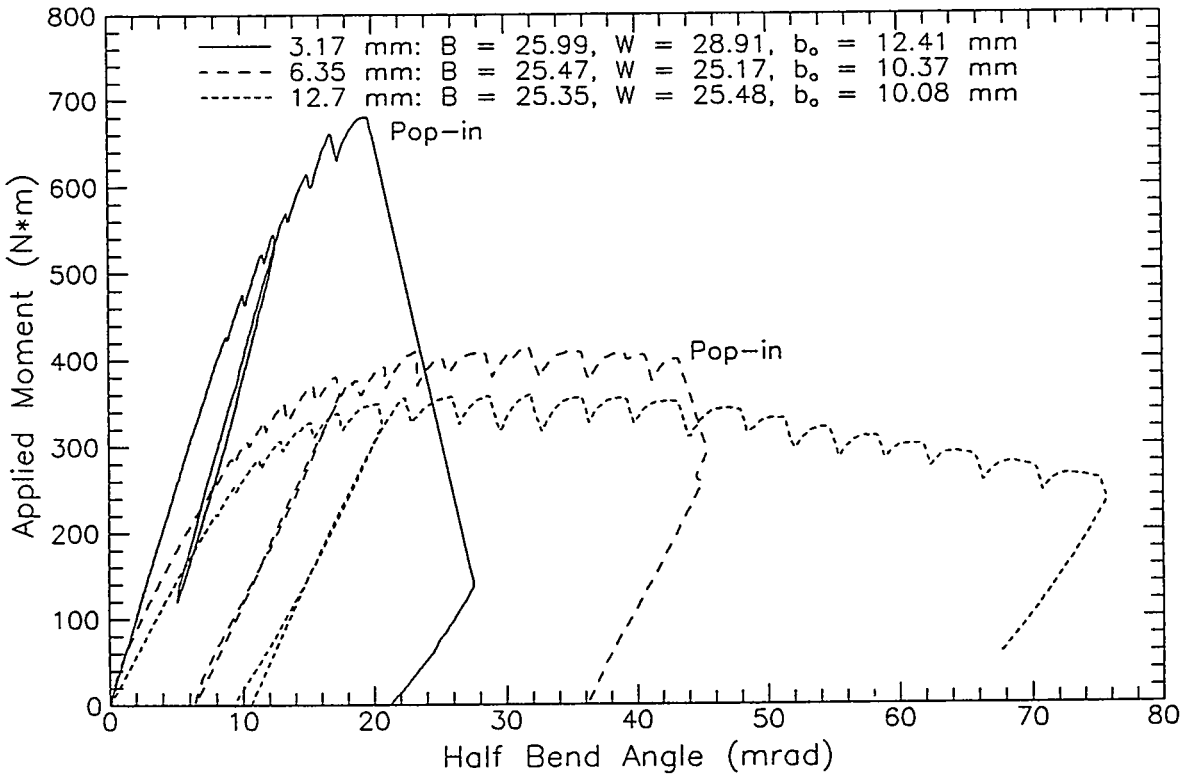

Figure 4 Moment vs. Bend Angle

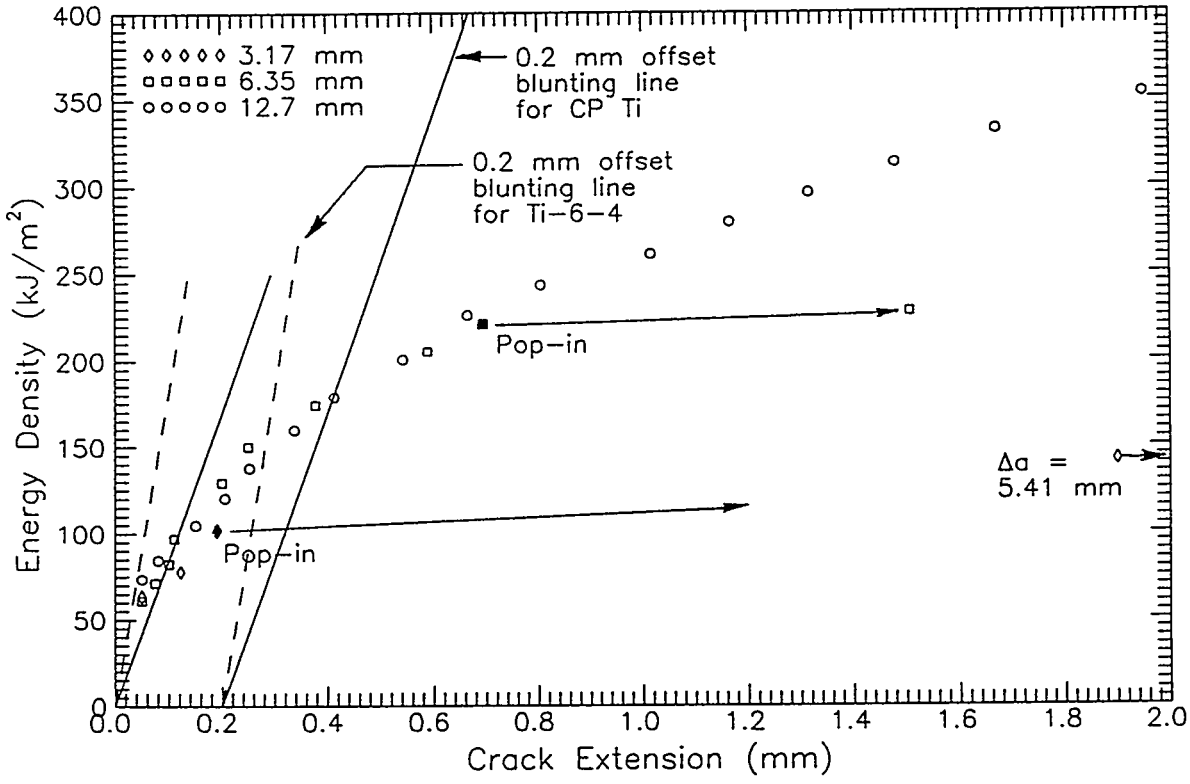

Figure 5 Crack Growth Resistance

Table 2

Summary of Test Results for Simulated Weldments

Weld thickness, H (mm)	J_c[a] (kJ/m^2)	dJ/da[b] (kJ/m^3)	Δa (mm)	$CTOD_{init}$ (mm)
3.2	95	≈0	0.18	0.10-0.12
6.4	175	≈105 000	0.68	Not determined
12.7	≈175	105 000	>2.0	0.18-0.2

a. Estimated values based on area under M-θ plot (Figure 4).

b. Estimated by drawing straight line on plots in Figure 5.

a way to obtain a stronger, though more brittle, weld. It is conceivable that an optimum "weld" width may be developed by combining the requirements for strength and fracture toughness.

CONCLUSIONS

- J_{Ic} decreased with increasing constraint and Δa (prior to failure) decreased with increasing constraint (Table 2).
- dJ/da decreased with increasing constraint. The dJ/da data did not satisfy E 813 or E 1152, which means that comparisons can only be made on a qualitative basis.
- CTOD for crack initiation decreased with increasing constraint.
- Reduction of the width of the weldment results in an increase in the load carrying capability.

ACKNOWLEDGMENT

This work was supported by the U.S. Department of Energy, Office of Energy Research, Office of Basic Energy Sciences, under DOE Idaho Field Office Contract DE-AC07-76ID01570.

REFERENCES

1. J. W. Hancock, W. G. Reuter, and D. M. Parks, "Constraint and Toughness Parameterized by T," ASTM STP 1171, March 1993.

2. S. M. Graham, W. G. Reuter, W. R. Lloyd, "The Validity of Standard Test Methods for Characterizing Weld Fracture," *Transaction of the ASME, 114*, 1992, pp. 16-21.

3. F. McClintock et al., "Criteria for Plane Strain, Fully Plastic, Quasi-Steady Crack Growth," submitted to *Int. J. Fracture* (1993).

4. Y.-J. Kim et al., "Global Equilibrium of the Least Upper Bound Circular Arcs and Its Application to Fracture Mechanics," submitted to *J. Mech. Physics Solids* (1993).

MEASUREMENTS OF THE ELASTIC CONSTANTS OF SUPERLATTICE FILMS BY LINE-FOCUS ACOUSTIC MICROSCOPY

J. D. Achenbach, J. O. Kim, and Y.-C. Lee

Center for Quality Engineering and Failure Prevention
Northwestern University
Evanston, Illinois 60208

ABSTRACT

The effective elastic constants of single-crystal TiN/NbN (001) superlattices have been determined using line-focus acoustic microscopy. Two independent procedures to determine the elastic constants of the superlattices are discussed. The first procedure calculates the effective elastic constants of the TiN/NbN superlattices from the elastic constants of the constituent TiN and NbN layers and verifies the calculated elastic constants by comparing the corresponding calculated SAW dispersion curves with measured dispersion curves. In the second procedure the effective elastic constants of the TiN/NbN superlattices are determined from the measured SAW dispersion data of the superlattices deposited on MgO substrates. The accuracy of each constant is estimated by considering the sensitivity of the dispersion curves to changes of each constant. The results of the two procedures are compared and advantages and disadvantages of each procedure are discussed.

INTRODUCTION

A superlattice film consists of a number of alternating thin layers of different elastic constants with period Λ, as shown in Figure 1. It has been shown that transition-metal nitride superlattice films, such as TiN/NbN, exhibit much higher hardness than homogeneous nitride films and show hardness peaks at particular values of the period Λ [1]. It has been suggested that the hardness peaks may be correlated with peaks in the elastic moduli, the so-called supermodulus effect [2]. A supermodulus effect, if present, is anomalous since analytical expressions for the elastic moduli of superlattices show that these quantities are independent of Λ. Recent Brillouin scattering measurements for TiN/NbN superlattices did not show a dependence of the Rayleigh wave velocity on Λ [3]. While these results show no anomaly, a more complete set of experimentally-determined superlattice elastic moduli is required to dismiss the possibility of elastic anomaly effects.

In the quantitative mode of acoustic microscopy the velocity of surface acoustic waves (SAWs) is measured [4]. Unlike point-focus acoustic microscopy, by which the velocity of SAWs averaged over all directions is measured, line-focus acoustic microscopy allows the measurement of the SAW velocity in a prescribed direction [5]. Hence line-focus acoustic microscopy has been used to measure the elastic properties of anisotropic materials. Measurements of anisotropic SAW dispersion curves for single-crystal thin films deposited on single-crystal solids have been reported in Ref. [6]. Recently, this technique has been applied to determine the elastic constants of single-crystal transition-metal nitride films [7] and amorphous carbon films [8]. The technique has also been used to verify the effective elastic constants of TiN/NbN superlattice films calculated from the elastic constants of the constituent layers [9].

In the present paper, a complete set of the effective elastic constants of TiN/NbN (001) superlattice films are determined by two independent procedures. Figure 2 is a flow chart of these procedures. Both

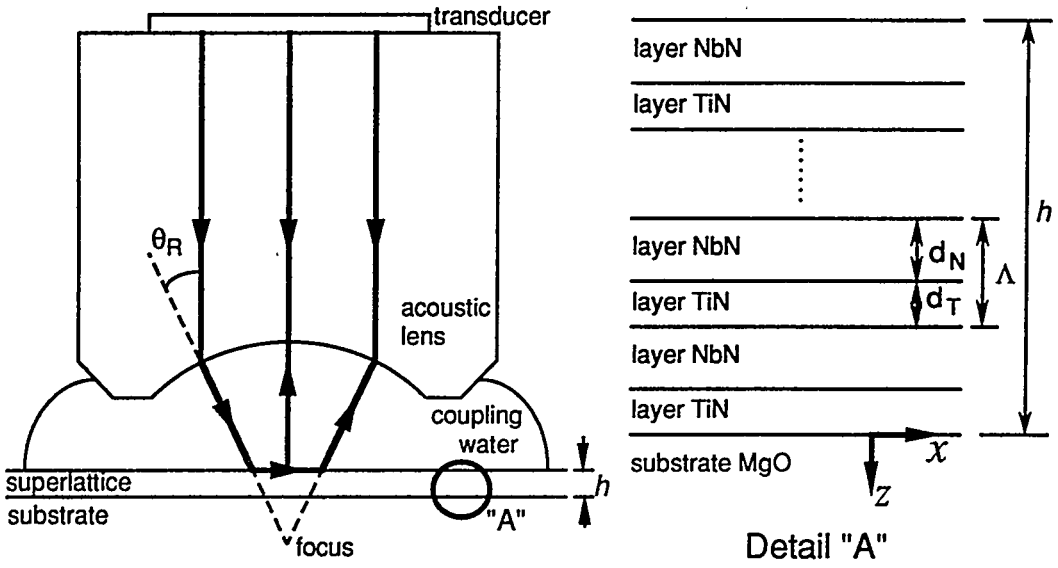

Figure 1. Schematic diagram of a line-focus acoustic lens and a TiN/NbN superlattice specimen. A number of alternating TiN and NbN layers were epitaxially grown on a cubic-crystal MgO substrate.

procedures are based on the SAW dispersion data obtained by line-focus acoustic microscopy for the films deposited on substrates.

The first procedure (referred to as Calculation Procedure) consists of several steps. The elastic constants of homogeneous TiN and NbN films deposited on MgO are determined from measured SAW dispersion data, according to the inversion method of Ref. [10]. From the so-obtained elastic constants of single-crystal TiN and NbN, the effective elastic constants of TiN/NbN superlattices are calculated. The calculated effective elastic constants are subsequently verified by comparing the corresponding calculated SAW dispersion curves with measured dispersion data for the TiN/NbN superlattice films deposited on MgO substrates.

In the second procedure (referred to as Measurement Procedure) the effective elastic constants of the TiN/NbN superlattices are determined directly from the measured SAW dispersion data of the superlattices deposited on MgO substrates. The inversion method is similar to but slightly modified from the method discussed in Ref. [10]. The accuracy of each constant is estimated by considering the sensitivity of the dispersion curves to changes of that constant.

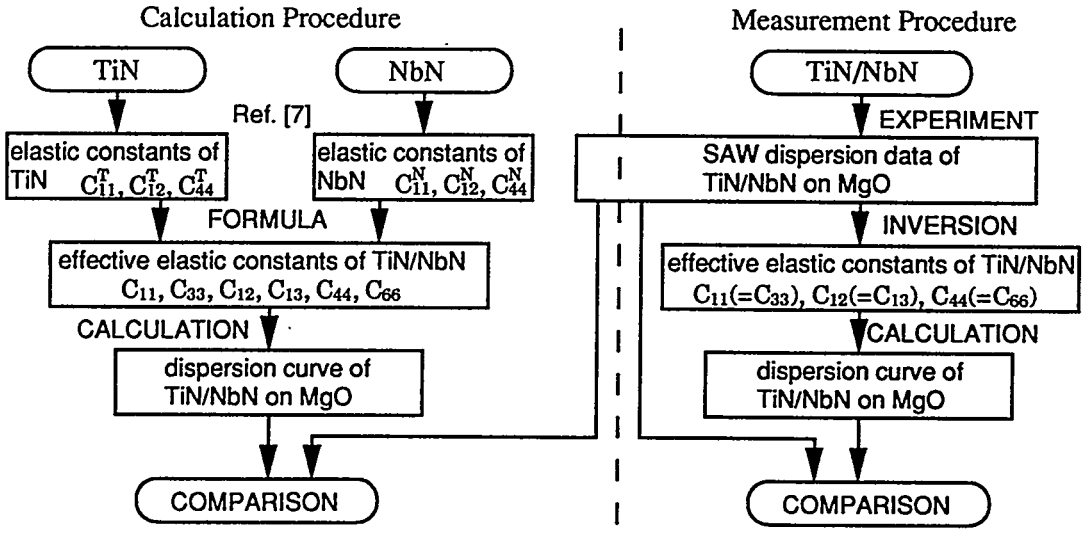

Figure 2. Two procedures to determine the effective elastic constants of single-crystal TiN/NbN (001) superlattices.

The results obtained by these two procedures are compared. Advantages and disadvantages of each procedure are discussed.

EXPERIMENTS

The TiN/NbN superlattice films were deposited on cubic-crystal MgO substrates using an ultra-high vacuum reactive magnetron sputtering system [11]. In-situ low energy electron diffraction from the specimens yielded spot patterns, indicating that epitaxial films were grown [1]. The period Λ was extracted from the x-ray diffraction results and when multiplied by the number of periods, yielded an estimate of the film thickness h. The film thickness h and the superlattice period Λ of the specimens used for the experiments are listed in Table 1. The fraction of the TiN layer thickness d_T to the period Λ is constant ($d_T/\Lambda = 0.3$) for all superlattice specimens.

The experimental results reported in this paper were obtained with a Honda AMS-5000 ultrasonic measurement system. The principle of this system and its hardware have been described in detail by Kushibiki and Chubachi [5]. The acoustic probe is schematically shown in Figure 1. The frequency of operation is around 225 MHz. The quantitative mode of acoustic microscopy is based on the measurement of the V(z) curve, which is a record of the transducer voltage output V with the variation of the distance z between the focal line of the acoustic lens and the surface of the specimen. The V(z) curves display oscillations due to interference between the specular reflection of the incident waves from the surface of the specimen and radiation of leaky surface waves generated by critical-angle-incident rays,.

The surface wave velocity v has a functional relationship to the spacing Δz of the valleys of the V(z) curve [12], which is given by the following equation [5,13]:

$$v = v_w \Big/ \left[1 - \left(1 - v_w/2f\Delta z\right)^2\right]^{1/2} = \left(v_w \cdot f \cdot \Delta z\right)^{1/2} \Big/ \left(1 - v_w/4f\Delta z\right)^{1/2} \qquad (1)$$

where v_w is the wave velocity in the coupling water and f is the wave frequency. The spacing Δz, and thus the SAW velocity of the specimen, is obtained by processing the V(z) data. The processing procedure consists of three main steps: subtraction of the geometric effect of the acoustic lens from the V(z) data, a digital low-pass filtering to reduce the component of high frequency noise, and fast Fourier transform analysis.

SAW velocities were measured on the (001) plane along wave propagation directions varying incrementally from the [100] to the [010] directions. The diamond-shaped symbols in Figure 3 are the results for 0.43, 0.91, 1.37 and 2.36 μm TiN/NbN superlattice films, as well as for bare MgO, measured at 225 MHz. The angle represents the direction relative to the [100] crystalline axis. Figure 3 shows the anisotropic dependence of the SAW velocities on the propagation direction for TiN/NbN (001) superlattice films epitaxially deposited on cubic-crystal MgO substrates. The results represented by solid lines and dashed lines (with circles) in Figure 3 are discussed in the next section.

CALCULATION OF THE EFFECTIVE ELASTIC CONSTANTS

Effective Elastic Constants Formula

The effective elastic constants of a superlattice film have been derived in terms of the elastic constants of the constituent layers. The effective elastic constants of a superlattice composed of isotropic layers can be found in Ref. [14]. For the more general case, i.e. a superlattice composed of single-crystal layers, the effective elastic constants were derived by Grimsditch [15].

Consider a superlattice which consists of cubic-crystal layers, all with the same orientation. The superlattice is considered to be tetragonal-symmetric because the properties along the direction vertical to the layer planes may be different from those along the layer planes. For an anisotropic material of tetragonal symmetry the stress-strain relations are

Table 1. Film thicknesses and superlattice periods of the TiN/NbN superlattice specimens.

Specimen number	Film thickness h (μm)	Period Λ (nm)
1	0	-
2	0.43	9.46
3	0.83	2.37
4	0.91	4.14
5	1.37	8.37
6	2.36	36.3
7	2.50	2.62
8	3.41	5.5
9	3.79	18.9

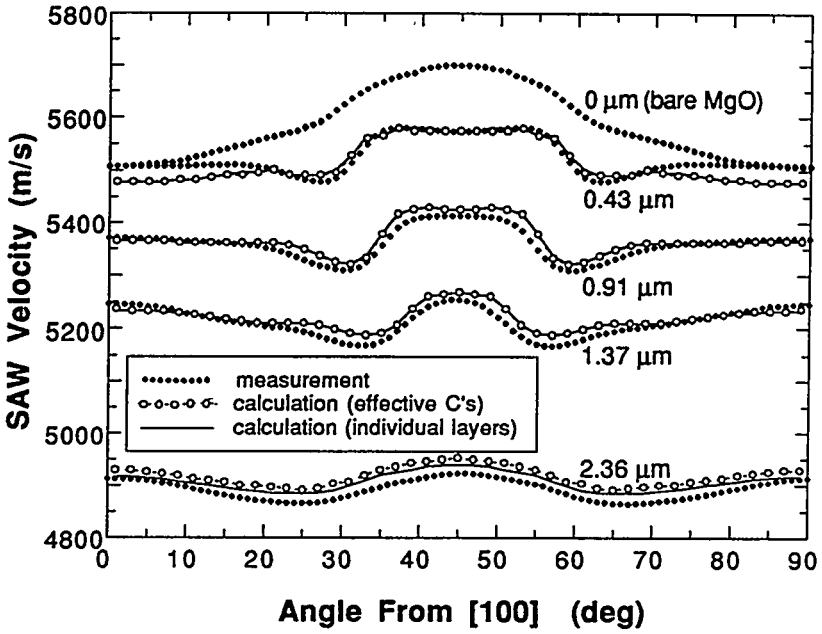

Figure 3. Anisotropic dependence of the SAW velocity at 225 MHz for the TiN/NbN (001) superlattices on MgO substrates.

$$\begin{Bmatrix} \sigma_x \\ \sigma_y \\ \sigma_z \\ \tau_{yz} \\ \tau_{zx} \\ \tau_{xy} \end{Bmatrix} = \begin{bmatrix} c_{11} & c_{12} & c_{13} & 0 & 0 & 0 \\ c_{12} & c_{11} & c_{13} & 0 & 0 & 0 \\ c_{13} & c_{13} & c_{33} & 0 & 0 & 0 \\ 0 & 0 & 0 & c_{44} & 0 & 0 \\ 0 & 0 & 0 & 0 & c_{44} & 0 \\ 0 & 0 & 0 & 0 & 0 & c_{66} \end{bmatrix} \begin{Bmatrix} \varepsilon_x \\ \varepsilon_y \\ \varepsilon_z \\ \gamma_{yz} \\ \gamma_{zx} \\ \gamma_{xy} \end{Bmatrix} \tag{2}$$

As shown in Figure 1, the thicknesses of the TiN and NbN layers are d_T and d_N, respectively, and the fractions of TiN and NbN are

$$\bar{d}_T \equiv d_T/(d_T + d_V) = d_T/\Lambda \qquad \text{and} \qquad \bar{d}_V \equiv d_V/(d_T + d_V) = d_V/\Lambda\,. \tag{3a,b}$$

The formulas to calculate the effective elastic constants of the tetragonal-symmetric superlattice can be obtained from Grimsditch's general results as:

$$c_{11} = \frac{1}{\dfrac{\bar{d}_T}{c_{11}^T} + \dfrac{\bar{d}_N}{c_{11}^N}} + \frac{(c_{11}^T - c_{11}^N)^2 - (c_{12}^T - c_{12}^N)^2}{\dfrac{c_{11}^T}{\bar{d}_T} + \dfrac{c_{11}^N}{\bar{d}_N}}, \qquad c_{33} = \frac{1}{\dfrac{\bar{d}_T}{c_{11}^T} + \dfrac{\bar{d}_N}{c_{11}^N}},$$

$$c_{12} = \frac{\dfrac{c_{12}^T}{c_{11}^T}\dfrac{c_{12}^N}{c_{11}^N}}{\dfrac{\bar{d}_T}{c_{11}^T} + \dfrac{\bar{d}_N}{c_{11}^N}} + \frac{(\bar{d}_T c_{12}^T + \bar{d}_N c_{12}^N)\left(\dfrac{c_{11}^T - c_{12}^T}{\bar{d}_T} + \dfrac{c_{11}^N - c_{12}^N}{\bar{d}_N}\right)}{\dfrac{c_{11}^T}{\bar{d}_T} + \dfrac{c_{11}^N}{\bar{d}_N}}, \qquad c_{13} = \frac{\dfrac{\bar{d}_T c_{12}^T}{c_{11}^T} + \dfrac{\bar{d}_N c_{12}^N}{c_{11}^N}}{\dfrac{\bar{d}_T}{c_{11}^T} + \dfrac{\bar{d}_N}{c_{11}^N}},$$

$$c_{44} = \frac{1}{\dfrac{\bar{d}_T}{c_{44}^T} + \dfrac{\bar{d}_N}{c_{44}^N}}, \quad \text{and} \quad c_{66} = \bar{d}_T c_{44}^T + \bar{d}_N c_{44}^N, \tag{4a-f}$$

where ($c_{11}^T, c_{12}^T, c_{44}^T$) and ($c_{11}^N, c_{12}^N, c_{44}^N$) are the elastic constants of the constituent layers of cubic symmetry. The effective mass density of the superlattice is

$$\rho = \bar{d}_T \rho_T + \bar{d}_N \rho_N . \quad (5)$$

Equations (4a-f) predict that the effective elastic constants do not depend on the superlattice period but do depend on the fraction of the two constituent layers.

The elastic constants of cubic-crystal TiN and NbN films have been determined from measured SAW dispersion data, according to the inversion method, and have been obtained as $c_{11}^T = 625$, $c_{12}^T = 165$, and $c_{44}^T = 163$ GPa for TiN and $c_{11}^N = 556$, $c_{12}^N = 152$, and $c_{44}^N = 125$ GPa for NbN [7]. The mass density of TiN is 5.39 g/cm^3 and that of NbN is 8.43 g/cm^3 [16]. The TiN fraction of the superlattices used in the experiment is $d_T/\Lambda = 0.3$. The effective elastic constants of TiN/NbN superlattices ($d_T/\Lambda = 0.3$) calculated using Equations (4a-f) are $c_{11} = 577$, $c_{33} = 575$, $c_{12} = 156$, $c_{13} = 156$, $c_{44} = 134$, and $c_{66} = 136$ GPa. The effective mass density of the superlattice obtained by Eq. (5) is 7.52 g/cm^3.

Verification of the Calculated Constants

As discussed in Ref. [6], the theoretical SAW velocities can most easily be compared with the measurements along the [100] and [110] directions. The velocity of SAWs propagating along a symmetry axis, either the [100] or the [110] direction, on the (001) plane of a tetragonal-symmetric film deposited on a cubic-symmetric substrate, can be calculated by equations presented in Ref. [9]. The measurements were carried out for the specimens of various thicknesses as listed in Table 1 at 195, 225, and 255 MHz. The SAW velocities calculated and measured for the various values of the film thickness and the frequency have been displayed in Figure 4 as functions of the normalized film thickness h/λ_s, where h is the film thickness and λ_s is the wavelength of a transverse wave in the substrate. Since the thicknesses of the films are much smaller than the SAW wavelength (~20 μm), the surface wave penetrates through the film into the substrate.

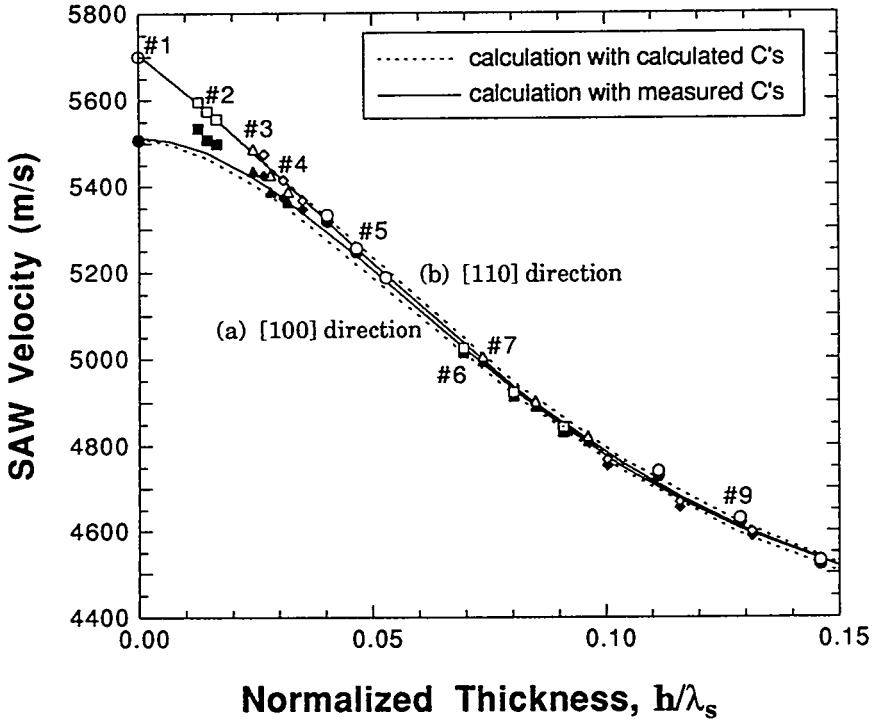

Figure 4. Dispersion curves of SAWs propagating along the [100] and [110] directions on the TiN/NbN (001) superlattice films deposited on MgO substrates. Specimen numbers are as shown in Table 1.

The results in Figure 4 show the effect of dispersion, i.e., the dependence of the velocity on the film thickness normalized by the wavelength of the transverse wave in the substrate. The dashed lines in Figure 4 are the dispersion curves for a TiN/NbN superlattice film deposited on an MgO substrate, calculated from the elastic constants and the mass density of the superlattice film determined in this section and the known elastic properties of the MgO substrate. The symbols are the measured SAW velocities. The experimental results show good agreement with the calculated results.

The SAW velocities for the superlattice films used in this work have also been calculated from the analysis of the V(z) curves in Ref. [17]. Solid lines in Figure 3 represent the results calculated using the effective elastic constants obtained above. Dashed lines with circles are the results calculated by considering the superlattice as a multilayer and using the elastic constants of the constituent TiN and NbN layers. Solid lines and dashed lines (with circles) in Figure 3 agree very well. It is, therefore, shown that the effective elastic constant approach is a sufficient accurate way to study the elastic properties of superlattice films.

MEASUREMENTS OF THE EFFECTIVE ELASTIC CONSTANTS

The Measurement Procedure determines the effective elastic constants of the superlattices from the SAW dispersion data obtained experimentally and displayed in Figure 4. However, it is not necessary to determine six independent elastic constants from the given data. Based on the calculated effective elastic constants, which yielded $c_{11} \approx c_{33}$, $c_{12} \approx c_{13}$, and $c_{44} \approx c_{66}$, it is assumed that the superlattice is a cubic-symmetric structure, which has only three independent elastic constants.

With known elastic constants and mass density of the substrate and known mass density of the superlattice, three independent elastic constants of the superlattice have been determined from the inversion of the experimental SAW dispersion data displayed by symbols in Figure 4. The inversion procedure consists of seeking a set of the constants that minimizes the sum of the squares of the deviations between measured and calculated velocities of SAWs propagating in TiN/NbN superlattice films deposited on MgO substrates. The sum is given as a function of c_{11}, c_{12} and c_{44}, as follows:

$$y = \sum_{q=1}^{N} \left[\left(V^{A}_{m,q} - V^{A}_{c,q} \right)^2 + \left(V^{B}_{m,q} - V^{B}_{c,q} \right)^2 \right], \tag{6}$$

where $V_{c,q} = V(\bar{h}_q, c_{11}, c_{12}, c_{44})$ and $\bar{h}$ is the normalized film thickness h/λ_s. The superscripts A and B refer to the [100] and [110] directions, respectively, the subscripts m and c denote measured and calculated results, and N is the number of data points for each direction. With initially estimated values of the elastic constants of the superlattice, the velocities of SAWs propagating either in the [100] or the [110] direction on the (001) plane of a cubic-symmetric film epitaxially deposited on a cubic-symmetric substrate, are calculated by the equations presented in Ref. [6]. The iterative calculation for minimizing the sum y is carried out by a systematic function minimization algorithm known as the simplex method [18].

The elastic constants of TiN/NbN superlattices have been determined by this procedure as $c_{11} = c_{33} = 587$, $c_{12} = c_{13} = 127$, and $c_{44} = c_{66} = 135$ GPa. These measured elastic constants are compared with the calculated elastic constants in Table 2 and discussed in the following section. The dispersion curves calculated from the effective elastic constants determined in this section are displayed by solid lines in Figure 4. They show good agreement with the measured dispersion data.

DISCUSSION

Accuracy

It is desirable to investigate the influence of each elastic constant on the SAW dispersion curves. The influence of the elastic constants determined in the previous section on the SAW dispersion curves for the TiN/NbN superlattices deposited on MgO substrates is shown in Figures 5(a) and 5(b). In Figure 5(a) the wave propagation direction is [100] while it is [110] in Figure 5(b). Figures 5(a) and 5(b) display the dispersion curves for the cases that one of the elastic constants is increased by 10%. It is observed that all elastic constants contribute to the change of the dispersion curves (a) and/or (b). It is, however, noted that

Table 2. The elastic properties of TiN, NbN, and TiN/NbN ($d_T/\Lambda = 0.3$).

		Effective elastic constants (GPa)						mass density (g/cm^3)
		c_{11}	c_{33}	c_{12}	c_{13}	c_{44}	c_{66}	
TiN	(Ref. [7])	625		165		163		5.39
NbN	(Ref. [7])	556		152		125		8.43
TiN/NbN	(calculation)	577	575	156	156	134	136	7.52
	(measurement)	587	587	127	127	135	135	
	(discrepancy, %)	(+2)	(+2)	(-19)	(-19)	(+1)	(-1)	

the dispersion curve is more sensitive to changes of c_{11} and c_{44} and less sensitive to changes of c_{12}. Inversely the calculated values of c_{12} may, therefore, be less accurate than the calculated values of the other constants.

Comparison of the Calculation and Measurement Procedures

The Calculation Procedure can determine six independent elastic constants of tetragonal-symmetric superlattices. This procedure consists, however, of several steps, and the accuracy of the measured elastic constants of the constituent layers affects the accuracy of the effective elastic constants of the superlattices. The procedure also depends on the validity of the formulas for the effective elastic constants. For example, if the interfaces between the layers are not perfect, the calculation of the effective elastic constants may not be accurate.

The Measurement Procedure can be used only when the symmetry of the superlattice is similar to the symmetry of the individual layers. If this assumption is valid, this procedure can determine the effective elastic constants of the superlattices more simply than Calculation Procedure.

The results of these procedures are compared in Table 2. It appears that the values of c_{11}, c_{33}, c_{44} and c_{66} obtained by the two procedures show agreement within 2% deviation. The values of c_{12} and c_{13} obtained by the procedures show, however, deviations of about 20%. These larger deviations are consistent with the anticipated inaccuracy of these constants for the individual layers as discussed above.

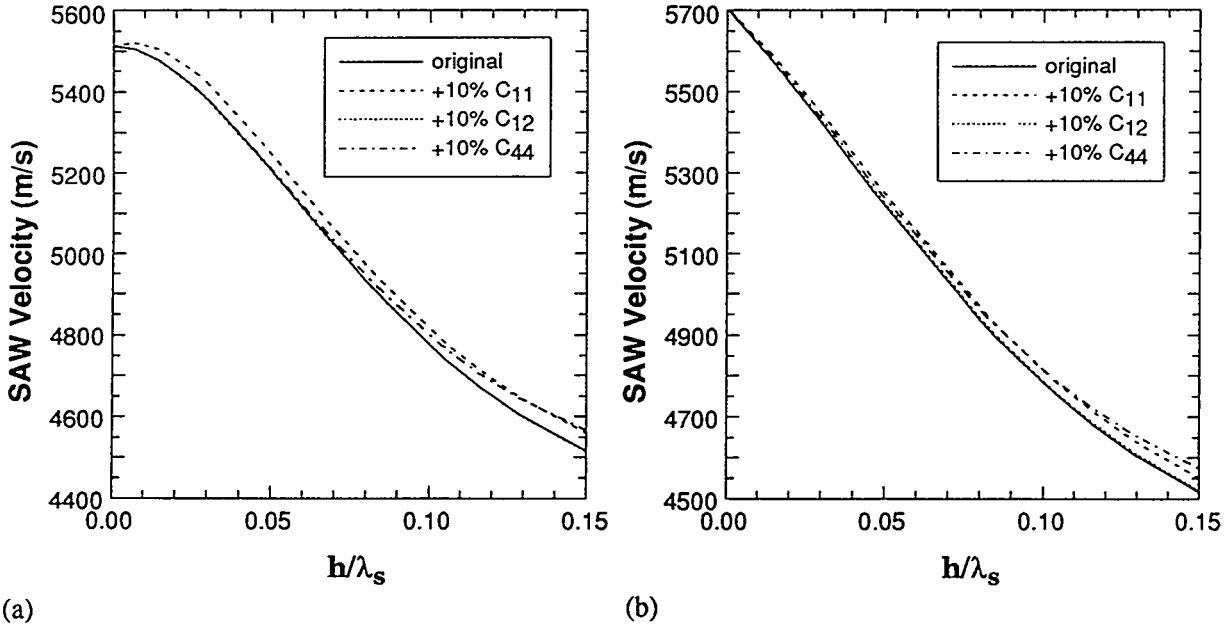

Figure 5. Influence of changes of c_{11}, c_{12}, and c_{44} of TiN/NbN on the SAW dispersion curves of the superlattice films on the MgO substrates: (a) the [100] direction, (b) the [110] direction.

SUMMARY AND CONCLUSION

The effective elastic constants of single-crystal superlattices have been determined by using SAW dispersion data obtained by line-focus acoustic microscopy. Two different procedures to obtain the elastic constants have been described. The first procedure calculates the effective elastic constants of the superlattices from the elastic constants of the constituent layers and verifies the calculated elastic constants by comparing the corresponding calculated SAW dispersion curves with measured dispersion curves. The second procedure determines the effective elastic constants from the measured SAW dispersion data of the superlattices deposited on substrates. Advantages and disadvantages of each procedure have been discussed. The accuracy of each constant has been estimated by considering the sensitivity of the dispersion curves to changes of that constant. The results for c_{11}, c_{33}, c_{44} and c_{66} obtained by the two procedures show good agreement with each other, while the results for c_{12} and c_{13} show significant deviations.

ACKNOWLEDGMENTS

This work was carried out in the course of research sponsored by the Department of Energy under Contract No. DE-FG02-86ER13484. The authors are pleased to acknowledge the help of Professor S. A. Barnett and Dr. M. Shinn for providing superlattice specimens.

REFERENCES

1. M. Shinn, L. Hultman, and S. A. Barnett, "Growth, structure, and microhardness of epitaxial TiN/NbN superlattices", *J. Mater. Res.* 7, 901 (1992).
2. U. Helmersson et al., "Growth of single-crystal TiN/VN strained-layer superlattices with extremely high mechanical hardness", *J. Appl. Phys.* 62, 481 (1987).
3. P. B. Mirkarimi et al., "Elastic Properties of TiN/(V_xNb_{1-x})N superlattices measured by Brillouin scattering", *J. Appl. Phys.* 71, 4955 (1992).
4. R. D. Weglein, "A model for predicting acoustic material signatures", *Appl. Phys. Lett.* 34, 179 (1979).
5. J. Kushibiki and N. Chubachi, "Material characterization by line-focus-beam acoustic microscope", *IEEE Trans. Sonics Ultrason.* SU-32, 189 (1985).
6. J. O. Kim and J. D. Achenbach, "Line-focus acoustic microscopy to measure anisotropic acoustic properties of thin films", *Thin Solid Films* 214, 25 (1992).
7. J. O. Kim et al., "Elastic constants of single-crystal transition-metal nitride films measured by line-focus acoustic microscopy", *J. Appl. Phys.* 72, 1805 (1992).
8. J. O. Kim and J. D. Achenbach, "Line-focus acoustic microscopy measurements of thin-film elastic constants", in *Review of Progress in Quantitative NDE*, Vol. 12, edited by D. O. Thompson and D. E. Chimenti, Plenum, New York, in press (1993).
9. J. O. Kim et al., "Effective elastic constants and acoustic properties of single-crystal TiN/NbN superlattices", *J. Mater. Res.* 7, 2248 (1992).
10. J. D. Achenbach and J. O. Kim, "Inversion of surface acoustic wave data to determine the elastic constants of nitride films", in *Proc. of IUTAM Symposium on Inverse Problems in Engineering Mechanics*, Springer-Verlag, in press (1993).
11. P. B. Mirkarimi, M. Shinn, and S. A. Barnett, "An ultrahigh vacuum, magnetron sputtering system for the growth and analysis of nitride superlattices", *J. Vac. Sci. Technol. A* 10, 75 (1992).
12. W. Parmon and H. L. Bertoni, "Ray interpretation of the material signature in the acoustic microscope", *Electron. Lett.* 15, 684 (1979).
13. R. D. Weglein, "Acoustic micro-metrology", *IEEE Trans. Sonics Ultrason.* SU-32, 225 (1985).
14. J. D. Achenbach, *A Theory of Elasticity with Microstructure for Directionally Reinforced Composites*, Springer-Verlag, New York (1975), pp. 21-38.
15. M. Grimsditch, "Effective elastic constants of superlattices", *Phys. Rev. B* 31, 6818 (1985).
16. H. Holleck, "Material selection for hard coatings", *J. Vac. Sci. Technol. A* 4, 2661 (1986).
17. Y.-C. Lee, J. O. Kim, and J. D. Achenbach, "V(z) curves of layered anisotropic materials for the line-focus acoustic microscope", *J. Acoust. Soc. Am.*, in press (1993).
18. J. A. Nelder and R. Mead, "A simplex method for function minimization", *Computer J.* 7, 308 (1965).

SUPERCONDUCTING PROPERTY MEASUREMENTS IN TAPE GEOMETRY

K. L. Telschow
Idaho National Engineering Laboratory
EG&G Idaho, Inc., P.O. Box 1625
Idaho Falls, ID 83415-2209

ABSTRACT

Fabrication of the new high T_c superconductor materials into useable long-length wires or tapes has proven difficult, often resulting in low critical currents. The ability to measure critical currents in high T_c superconducting tapes on a local scale can be valuable for assessing the microstructure resulting from the fabrication process. This paper describes the results of research on using induced currents from a small noncontacting electromagnetic probe to determine the critical current density in high T_c tapes on a local scale. The technique forces full-field penetration into the tape locally and infers the local critical current density from the "critical state" model for flux penetration. Difficulties encountered with the tape geometry and demagnetization effects are overcome by an analysis procedure that provides comparative measurement of the critical current density with the contacting DC transport probe method. Results for several tapes with different critical currents are discussed.

INTRODUCTION

The new high T_c materials are extreme type II superconductors where, in the presence of an external magnetic field and/or a transport current, magnetic flux exists in the material in the form of flux lines distributed on a lattice [1]. Individual flux lines are pinned at microstructural inhomogeneities such that only under a sufficient force, caused by locally high current flows, will they become depinned and flow throughout the material. The value of local current density at which depinning occurs, the microscopic critical current density (J_c), is directly proportional to the pinning force strength. Intergrain junctions form the weakest spots in polycrystalline samples. Flux penetrates the sample relatively easily along the intergrain junctions, and these pinning sites are responsible for the low critical currents observed to date in macroscopic tapes. The critical state model [2] describes the pinned flux line distribution within the material quasistatically, assuming the equilibrium distribution is achieved at each value of the externally applied field on a time scale that is short compared to experimental times. Flux lines penetrate the material to a flux front boundary, which eventually penetrates the sample completely at a particular value of the external field (H*). Ampere's law relates the full-field penetration value H* at the surface to the critical current density and layer thickness (d) by $H^* = J_c d/2$ for a layer superconducting geometry in a parallel applied field.

This paper describes noncontacting AC measurements of H* in a set of 12 tapes of $(Bi,Pb)_2Sr_2Ca_2Cu_3O_x$ with silver cladding produced with varying pressing parameters. The tapes exhibit a variety of critical currents resulting from various microstructural defects. The measurement results presented can be described in terms of the single parameter H*, which is a function of tape thickness,

temperature, and microstructure. An analysis procedure is described to quantitatively compare the AC induction results with contact DC transport measurements.

EXPERIMENTAL RESULTS

A set of 12 Ag-clad $(Bi,Pb)_2Sr_2Ca_2Cu_3O_X$ (2223 phase) tapes, fabricated from polyphase 2212/2201 starting powder, were used for this study [3]. The tapes were approximately 1 cm wide by 3 cm long, with thicknesses of about 0.1 mm each for the superconducting and silver layers. The composition of these tapes has been previously described [4]. Local magnetization was measured with small concentric solenoidal coils. The drive field coil had a radius of 1.25 mm and was wound with 12 turns of #38 wire; balanced pickup coils were wound over the drive coil with 5 turns each. The calculated peak magnetic field strength parallel to and at the sample surface ranges from approximately 350 A/m, in the absence of a sample, to 700 A/m with a fully superconducting sample, for an excitation current of 100 Ma. Response of the induced current was recorded by a lockin amplifier at a frequency of 1 KHz. Measurement geometry and cryostat have been previously described [5,6]. The coil position was fixed at approximately the center of the sample surface at an elevation of 0.1 mm to the lowest winding. The probe was used by increasing the AC excitation field until full penetration of the critical state region through the tape was achieved locally under the coil. The effect of the eddy currents induced in the silver coating was subtracted by an external signal dividing circuit balanced at 120 K, well above the onset of superconductivity of about 110 K found for these samples.

AC measurements described are similar to laboratory AC magnetic susceptibility measurements that are performed with cylindrically shaped samples in parallel externally applied magnetic fields. However, in the geometry employed for the tape measurements, the externally applied field is nonuniform, and significant demagnetization effects occur. Figure 1 shows the AC signal response for four representative tape samples. The measured DC transport critical currents for the sample set ranged from 520 A/cm^2 for #4A to 2,200 A/cm^2 for #4C, all at 77 K and the earth's magnetic field. Results shown in Figure 1 are very similar to those obtained from the laboratory AC susceptibility measurements, except that the demagnetization effects preclude quantitative comparison between theory and experiment using the critical state model. The same features caused by intergrain and intragrain critical currents are observed both in the demagnetizing geometry and in the laboratory geometry. In particular, all samples show a transition temperature of about 110 K, where the inductive (imag) signal drops abruptly due to the onset of superconductive shielding currents developed within grains of the material. This initial drop is followed by a more gradual drop, with temperature caused by the onset of intergranular shielding currents. When 70 K is reached, all samples provided essentially complete shielding due to both intergranular and intragranular currents. Samples with the highest critical currents at 77 K also exhibited the most rapid drop in inductive signals with temperature as illustrated in Figure 1.

A great deal of information about a sample is contained in the data of Figure 1. However, for nondestructive evaluation of tape processing, measurements are needed as a function of position along the tape while the tape is at one temperature. These measurements are most conveniently taken at liquid nitrogen temperature, with the tape submerged and with a small local probe that can be scanned along the tape. The AC susceptibility measurements described can be used in this manner [5,6]. Probe coils are small and can be easily scanned along the tape surface. The task of determining the local critical current density then can be performed by varying the excitation field and recording the change in response of the tape as the critical state penetrates the tape thickness. Figure 2 shows the AC signal magnitude as a function of the excitation coil current for the four samples considered. Results shown are for sample temperatures from 30 to 110 K. The applied field has been subtracted by the balanced coils, such that the net sample magnetization signal magnitude is shown. At the lowest temperature, the response for the best samples (1A and 4C) is proportional to the excitation field (or AC current) and corresponds with that for a completely shielded sample, i.e., the basic probe response. These results are independent of the sample, since fields applied are much less than the upper critical field at this temperature. Figure 2 also shows results for varying penetrations of the flux line lattice into the sample that occur as the temperature is changed.

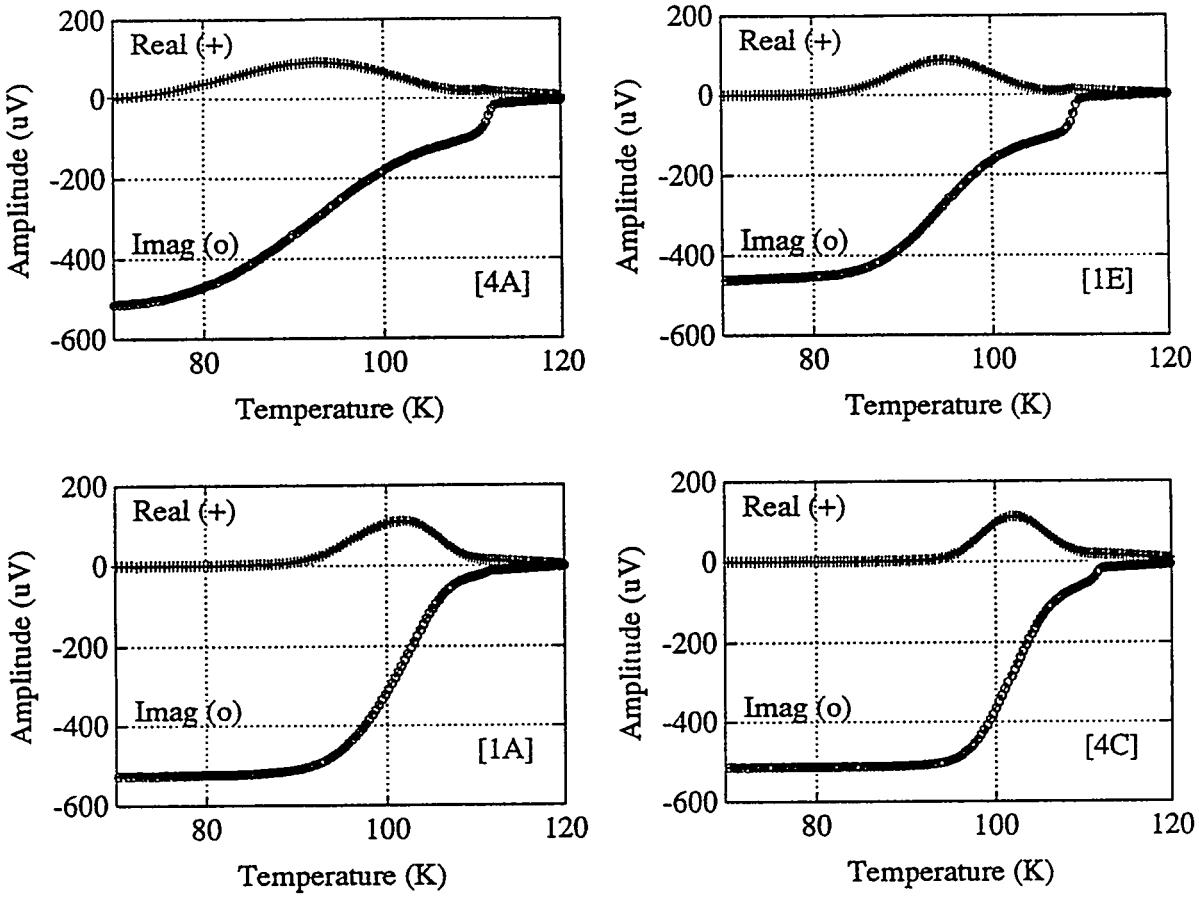

Figure 1. AC Measurements of Four Tape Samples with Critical Current Densities at 77 K of 520 A/cm^2 [4A], 873 A/cm^2 [1E], 1,133 A/cm^2 [1A], and 2,200 A/cm^2 [4C]

H* DATA ANALYSIS

To use the results of Figure 2 for quantitatively determining the local critical current, the critical state model is invoked to obtain the local full penetration field strength. The basic probe response was eliminated by dividing the results by the data at the lowest temperature. This yields the normalized results of Figure 3 for the temperatures where the sample was superconducting. The critical state model prediction for flux penetration is a geometric calculation based on one parameter: the full-field penetration value, H*. For the given probe/sample geometry, there is a well-defined H*(T,d), which depends on sample microstructure, temperature, and layer thickness. In principle, H* can be calculated directly; however, this calculation has proved amenable only in situations where the externally applied field is uniform and the sample shape is sufficiently simple that no demagnetization effects are present [7,8]. Calculations of References 7 and 8 are for a slab geometry in a parallel field where the demagnetizing factor is zero and assume a $1/H_{LOCAL}$ dependence of the local critical current density. Results reported here are very similar, even though the geometry is more complex. Recently, calculations have been reported for sample shapes (sphere and cylinder) exhibiting demagnetization effects in a uniform field [9,10]. The geometry used here is that most practical for actual measurement on tapes; it uses a source coil producing a nonuniform field throughout the sample exhibiting demagnetizing effects. At the present time an acceptable method for calculating the extent of the critical

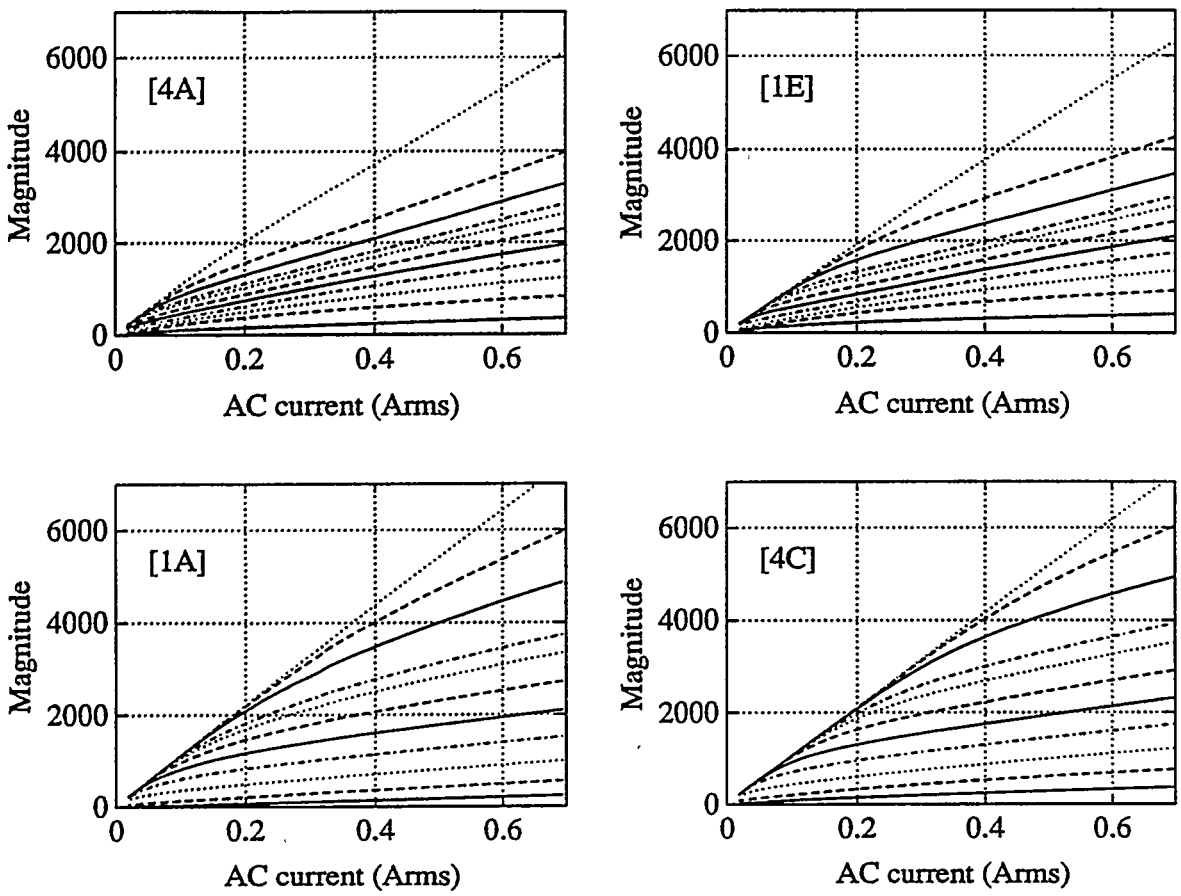

Figure 2. AC Response for the Four Sample Tapes of Figure 1 as a Function of the Excitation Field (AC Current) and for Temperatures Ranging from 30 to 110 K

state region in geometries with nonuniform external fields has not been developed. With an appropriate model, the complete signal response could be calculated and an accurate determination of H* obtained directly from the measurements. In the absence of this calculational approach, an empirical approach was taken to provide the required normalization [11]. Since the critical state model suggests the response should be a function of only one intrinsic parameter, H*, all results should scale with this value at a given temperature and sample thickness.

Figure 3 shows the data of Figure 2 redrawn at scaled drive current values such that all the data overlap on one curve, a reference curve shown in Figure 3 for sample 4A. The reference curve was obtained from the data of sample 1A and accounts for the probe/sample geometry. The reference curve also provides a method with which to compare data for other temperatures and samples in a quantitative manner to that of sample 1A. Scaling factors for the current that align the data depict the ratio between the full-field penetration values for a given sample to that of the reference. Results of Figure 3 show that the scaling renormalization works best for samples with high critical currents. This was generally found for the entire sample set. Low critical currents are caused by poor intergrain junctions, nonalignment of the grains, variation in layer thickness, and impurities. All of these characteristics are present in these tape samples to some degree and have been previously described [4]. Presenting the data in the form of Figure 3 appears to more selectively illustrate samples with these problems than presenting the data in the form of Figure 2. Most deviations of Figure 3 occur for the higher external fields, when the critical state is extending throughout the tape and reaching the lower layer boundary.

To obtain the critical current value for any other sample, the relationship between H* and $J_c d$ must be known quantitatively. This relationship can be obtained through measuring critical current and

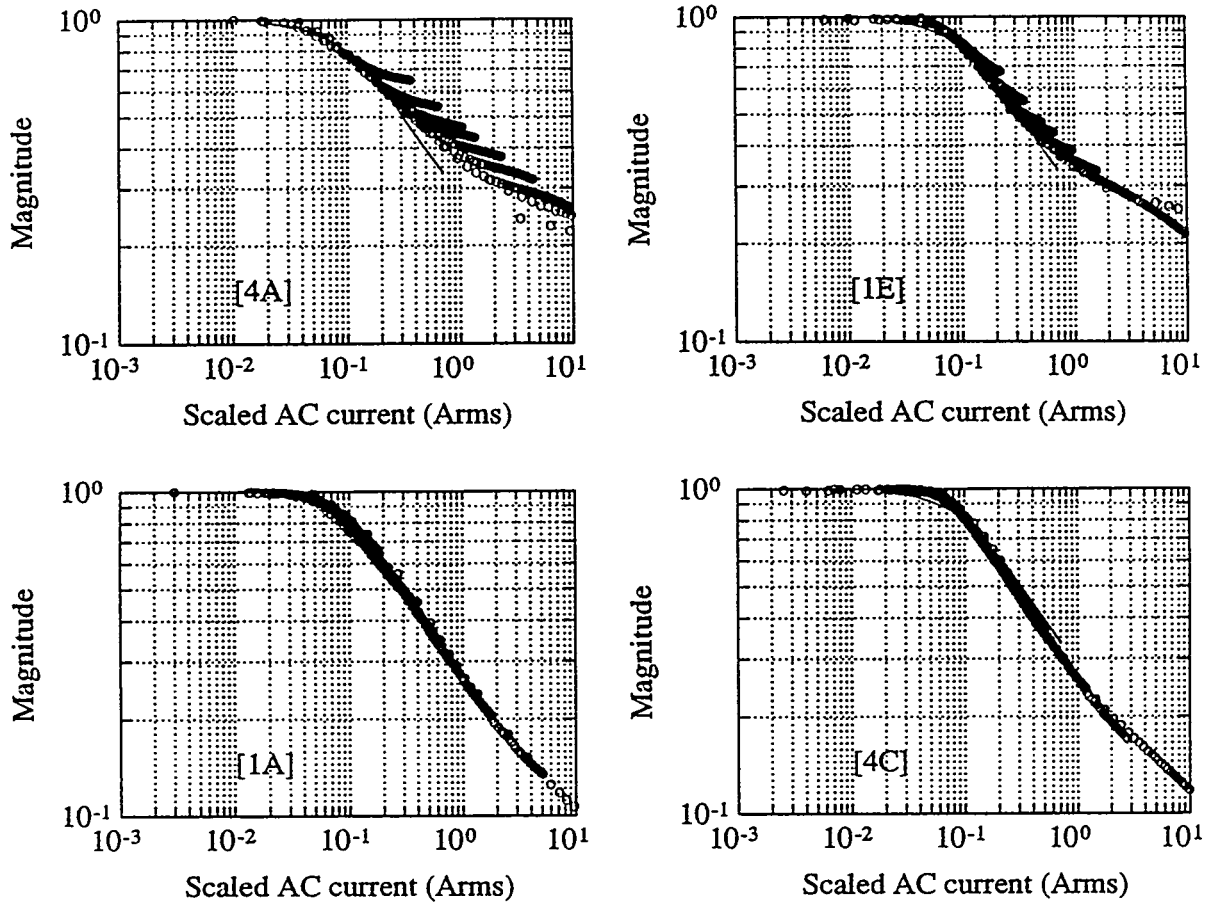

Figure 3. Normalized AC Signals for the Four Samples of Figure 1 as a Function of the Scaled Excitation Coil Current

layer thickness - J_{c0} and d_0 for one sample at some known temperature, T_0, by the DC transport technique and by measuring AC probe results, compared to the reference curve as before, $H^*(T_0)/H^*(T_R)$. The critical current for the unknown sample is then given by:

$$\frac{J_c(T)\,d}{J_{c0}(T_0)\,d_0} = \frac{H^*(T)/H^*(T_R)}{H^*(T_0)/H^*(T_R)}$$

Figure 4 shows the resulting scale factors for the entire set of 12 samples at 77 K. The scaling factors are proportional to the full-field penetration value (H*) for that sample. Data from sample 1A at T_R = 91 K was used as the reference curve. Theoretically, there should be a linear relationship between critical current density (J_c) and full-field penetration value (H*). Results in Figure 4 are shown compared to a least squares fit straight line, which serves as a guide to the eye. There are several reasons why there may be considerable scatter in the results. The critical current densities were obtained by the contact DC transport method, which averages more than at least 1 cm of tape length, whereas the AC probe is more local. The two measurements were not taken at exactly the same location along the tape, as the samples tested here are cuttings from a longer tape. Also, the superconducting tape thickness used to determine the DC transport critical current density could only be approximated by taking one-third of the total tape thickness, since there was no way to obtain this value without

sectioning the tape samples. Results are better correlated when one sample is used to find comparative values of J_c at different temperatures.

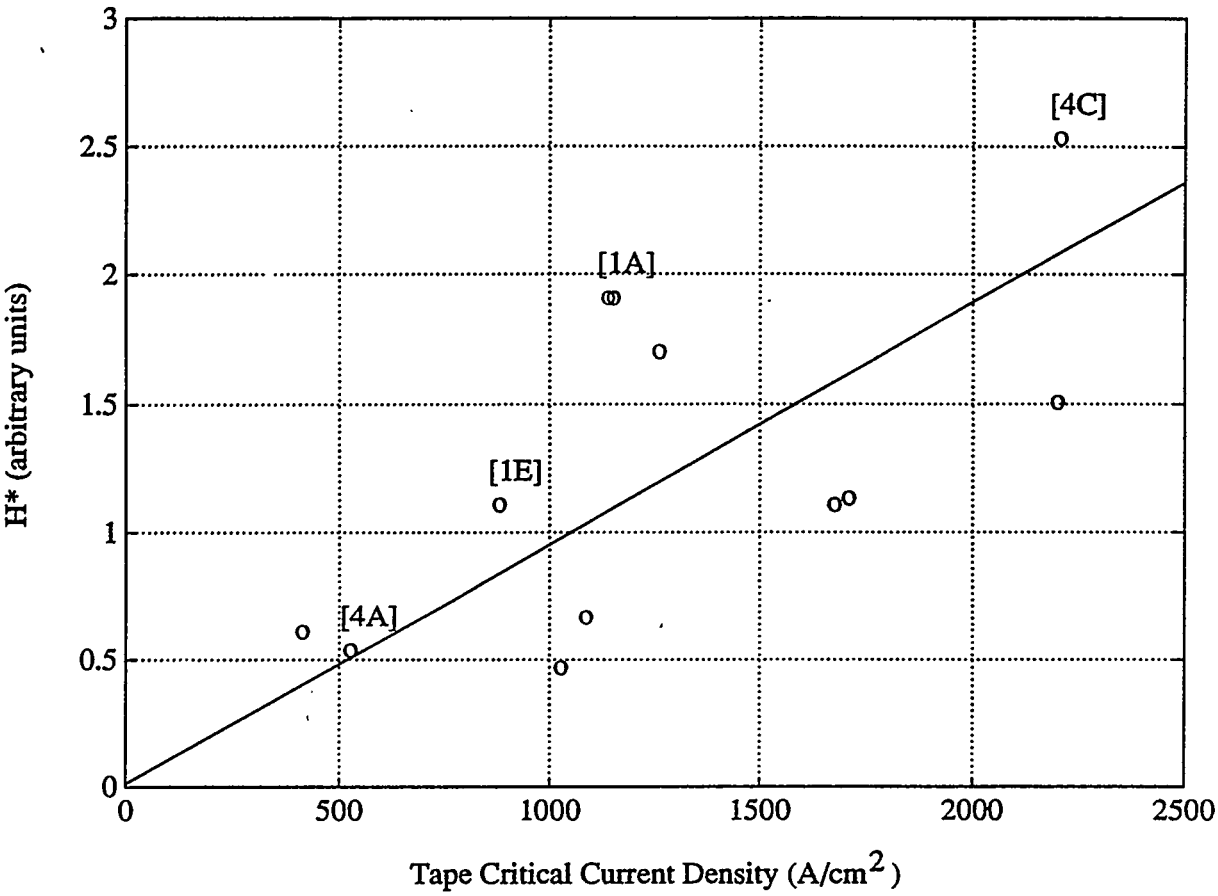

Figure 4. Results for the Entire Set of 12 Samples Comparing the Full-Field Penetration Values Obtained from the Scaling Factors Used in Figure 3 with the Independent DC Transport Critical Current Density Measurements at 77 K

SUMMARY

This paper described a procedure, using induced screening currents, to measure the transport critical current in high T_c superconductors. The method is quantitative and applicable to practical geometries, such as tapes. Data shown are consistent with the DC transport results and illustrate how the local AC probe can be used to compare various locations along a given tape or to compare different tapes. Either a full analytical determination of the critical state response in the probe/sample geometry or a normalization with a DC transport J_c measurement of a reference sample is required. The small size of the probe allows spatial measurements within a resolution determined by coil size. The utility of the method was demonstrated by measuring a set of 12 samples prepared by the powder-in-tube method using varying pressing parameters.

ACKNOWLEDGMENTS

The author would like to thank M. T. Lanagan and D. Y. Kaufman at Argonne National Laboratory for providing the high T_C tape samples and the DC transport critical current density results. Efforts of T. K. O'Brien in obtaining measurement results are appreciated. This work was supported by the U.S. Department of Energy, Office of Energy Research, Office of Basic Energy Sciences, under DOE Idaho Field Office Contract DE-AC07-76ID01570.

REFERENCES

1. A. M. CAMPBELL and J. E. EVETTS, *Critical Currents in Superconductors*, London: Taylor & Francis Ltd., 1972.

2. C. P. BEAN, "Magnetization of High-Field Superconductors," *Rev. Mod. Phys.*, 36, pp. 31-39, January 1964.

3. Tape samples and DC transport critical current measurements were provided by M. T. LANAGAN at Argonne National Laboratory.

4. K. L. TELSCHOW et al., "Local Critical Current Measurements on BiSrCaCuO/Ag Tape with an Electromagnetic Probe," to be published in *IEEE Transactions on Superconductivity*, and presented at the 1992 Applied Superconductivity Conference, August 23-28, Chicago.

5. K. L. TELSCHOW and T. K. O'BRIEN, "Noncontacting Alternating Current Surface Probe Measurements of Transport Critical Current in a Slab Geometry," *Appl. Phys. Lett.*, 59, pp. 730-732, August 1991.

6. K. L. TELSCHOW and T. K. O'BRIEN, "Critical Current Measurements of High T_C Superconductors in a Scanning Low-Temperature Cryostat," *in Reviews of Progress in Quantitative NDE*, Bowdoin, ME, July 1991, Vol. 11B, pp. 1,853-1,859.

7. L. JI et al., "Critical-State Model for Harmonic Generation in High-Temperature Superconductors," *Phys. Rev.*, B40, pp. 10,936-10,945, December 1989.

8. T. ISHIDA and R. B. GOLDFARB, "Fundamental and Harmonic Susceptibilities of $YBa_2Cu_3O_{7-X}$," *Phys. Rev.*, B41, pp. 8,937-8,948, May 1989.

9. K. V. BHAGWAT and P. CHADDAH, "Magnetization Curves of Hard Superconductor Samples with Non-Zero Demagnetization Factor," *Pramana-J. Phys.*, 33, 4, pp. 521-540, October 1989.

10. R. NAVARRO and L. J. CAMPBELL, "Magnetic-Flux Profiles of High T_C Superconducting Granules: Three-Dimensional Critical-State-Model Approximation," *Phys. Rev.*, B44, pp. 10,146-10,157, November 1991. (See also P. CHADDAH and K. V. BHAGWAT, *Phys. Rev.*, B46, p. 14,926, December 1992, and R. NAVARRO and L. J. CAMPBELL, *Phys. Rev.*, B46, p. 14,927, December 1992.

11. K. L. TELSCHOW, "Single Parameter Analysis of Hysteretic Magnetic Flux Trapping in High T_C Superconductor Ribbon," in *Reviews of Progress in Quantitative NDE*, D. O. Thompson and D. E. Chimenti (eds.), Plenum Press, New York, 1993, to be published.

Photothermal Measurements of Superconductors

G. S. Kino, X. D. Wu, A. Kapitulnik, and I. Fishman

Edward L. Ginzton Laboratory
Stanford University
Stanford, CA 94305-4085

ABSTRACT

We have developed a new photothermal technique to investigate electronic phase transitions of high temperature superconductors. The phase shift of the thermal wave yields the anisotropic thermal diffusivity coefficient of the sample. The amplitude of the photothermal signal is sensitive to electronic phase transitions of the second kind. The technique is completely noncontacting and nondestructive, and is well suited to measure small and fragile single-crystal high-T_c superconductors. The measurements give good agreement with fluctuation theory near the transition temperature. We have studied diffusion in and superconducting fluctuations of single crystals of $YBa_2Cu_3O_{7-\delta}$ and $Bi_2Sr_2CaCu_2O_8$. Both systems show fluctuation effects beyond Gaussian fluctuations. While $YBa_2Cu_3O_{7-\delta}$ behaves as a three-dimensional anisotropic superconductor, results on $Bi_2Sr_2CaCu_2O_8$ indicate strong two-dimensional effects.

INTRODUCTION

High quality single crystal specimens of the newly discovered high-temperature superconductors are small. Their anisotropic thermal properties are often difficult to measure with standard bulk techniques, and the effect of electronic phase transition on the thermal properties is often masked by the dominant thermal properties of the bulk material. Therefore, a method that can measure thermal properties on a very small scale, and is sensitive to electronic phase transitions, is desired.

In this paper, we describe a new photothermal technique that has the following capabilities:

1) It can measure anisotropic thermal diffusivity within an area of ~20 μm^2.
2) It can measure a quantity that is proportional to the specific heat; hence, it can provide useful information about the specific heat anomaly through the transition.

The photothermal technique uses a modulated focused light beam to periodically vary the temperature of a superconductor on which the beam impinges. The thermal waves excited, periodically vary the refractive index, and hence the optical reflectivity R, of the sample. The rate of change of optical reflectivity with temperature $\partial R/\partial T$ of the sample is detected with a second focused light beam. From the phase of the thermal wave, we can directly determine the anisotropic diffusion coefficient of the material. Since the light couples energy directly to the electrons in the material at the probe spot, the amplitude of the reflected probe beam is sensitive to the electron den-

sity of the sample. This makes photothermal microscopy an extremely useful technique to investigate directly the thermodynamic fluctuations of the electron density and density correlation near a phase transition. The periodically-varying amplitude of the reflected detecting beam shows a large peak near the critical temperature T_c, and this amplitude can be shown to be proportional to the singular part of the specific heat. The results can then be compared with the Ginzburg-Landau fluctuation theory for phase transitions of superconductors.

The technique is completely noncontacting and nondestructive. More importantly, since we focus light down to spot sizes of $2\ \mu m$ in diameter, with a $10\text{-}15\ \mu m$ separation between the heating spot and probing spots, we can measure directional thermal diffusivity locally within one domain of a single-crystal high-T_c superconductor. Similarly, the fluctuation measurements are made in a very small region, a few cubic micrometers in extent.

DIFFUSION THEORY

In an anisotropic medium, if we align the coordinate axes along the principal axes so that the anisotropic thermal diffusivity $\kappa_{ij} = 0$ for $i \neq j$, the homogeneous diffusion equation becomes:

$$\kappa_{ii} \frac{\partial^2 T}{\partial x_i^2} = \rho C \frac{\partial T}{\partial t}$$

where T is the temperature, ρ is the density, and C is the heat capacity. This equation can be written in a familiar isotropic form by changing the independent variables to $x'_i = x_i \sqrt{\kappa / \kappa_{ii}}$

$$\sum_{i=1}^{3} \frac{\partial^2 T}{\partial x_i'^2} = \frac{1}{D} \frac{\partial T}{\partial t}$$

where $D = \kappa/\rho C$ is defined as the isotropic thermal diffusivity in the new coordinate system. For a periodic temperature variation, $\exp j\omega t$, the solutions for a point excitation are in the form of damped thermal waves: $(1/r')\exp -(1+j)r'\sqrt{\omega/2D}$. If the phase delay $\Delta\phi_i$ of the temperature variation at a distance Δx_i away from the excitation source is measured along the ith direction, the thermal diffusivity can be determined along this direction by writing $D'_{ii} = (\omega/2)(\Delta x_i / \Delta\phi_i)^2$. To account for the finite size of the heating and probe beams, we have used a full three-dimensional model with a Gaussian beam excitation to solve for the temperature variation, using the primed coordinate system defined above. However, with a spot size of $2\ \mu m$, and separation distances between the exciting and detecting beams over $12\ \mu m$ apart, the simple approximation of a point source and point detector beam yields results very close to the full three-dimensional solution.

EXPERIMENT

The experimental set-up is shown in Fig. 1. An argon laser beam (514 nm) is acousto-optically modulated at a frequency of a few kiloherz and focused onto a sample; this beam periodically modulates the temperature of the sample and excites a thermal wave with a diffusion length of the order of $10\text{-}40\ \mu m$. At a known distance away, typically $10\text{-}15\ \mu m$, another infrared semiconductor laser (780 nm) is focused onto the sample and is used as a probe beam; a semiconductor laser is chosen because of its low noise. The reflected infrared laser light is selected with a dichroic filter and beamsplitter and impinges on a PIN photodiode whose output signal is measured with a lock-in amplifier. The amplitude of the detected signal is proportional to dR/dT, where R is the reflectivity of the sample and the phase relative to the modulation of the incident beam is the result of thermal wave propagation from the heating spot to the probe beam spot.. As already discussed, we use the phase information to determine the anisotropic diffusion constant of the sample in the direction

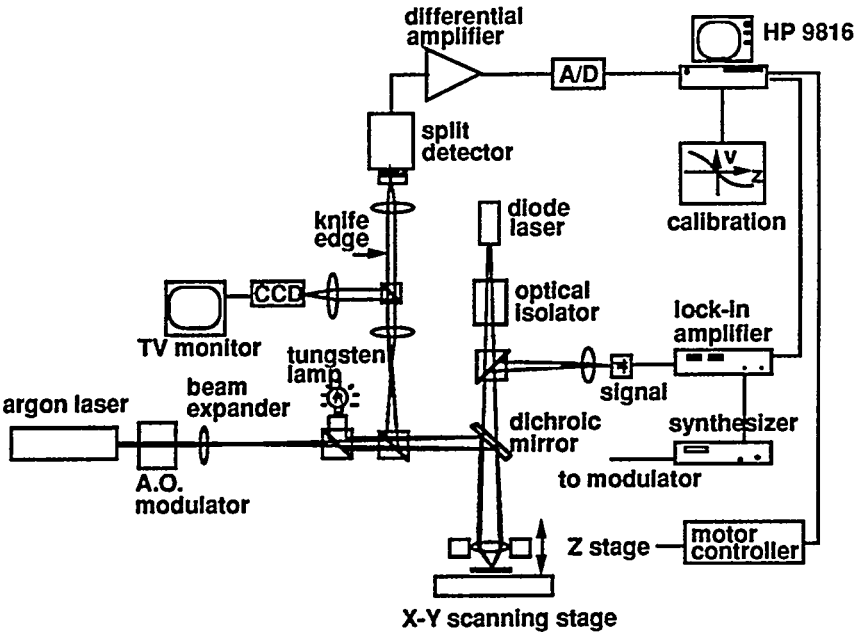

Fig. 1. Experimental setup for photothermal measurement of high-T_c superconductors.

between the two laser spots. Phase measurement has the great advantage for this purpose that it is independent of the incident signal amplitude or the reflectivity of the sample.

To measure the amplitude and phase of the output signal as a function of temperature, the sample is mounted on a cold finger in a cryostat. The pressure inside the cryostat is kept below 2×10^{-7} torr to limit the ice build-up on the surface of the sample. The optical beams are focused by a 0.33 NA long working distance lens onto the sample through a 100 μm thick sapphire window, made this thin to minimize aberrations of the focused beams.

During the cooling or heating process, the tip of the cold finger tends to move as a result of mechanical contraction or expansion. Therefore, an autofocusing mechanism is employed to adjust the z-position of the objective to ensure that the surface of the sample is always in focus. A focusing error of ±1 μm , well within the depth of focus (5 μm) of the focused beam, is easily achieved in our measurements . The photothermal microscope is also used as a conventional microscope. A tungsten lamp is added to the optical path of the system to illuminate the sample surface, and a high-pass filter is placed in front of the lamp to reduce its heating effect on the sample, which is imaged with a CCD camera. This makes it possible to compensate manually for the movement of the sample in the x- and y-directions with a motorized stage, and to select a crack-free region of the sample for the measurement.

To ensure an accurate temperature measurement of the sample, we reduce the static heating effect of the lasers. The laser power of both the heating and probe lasers is limited to only a few microwatts. The optical beams are focused to spots of 2 microns in diameter. A three-dimensional theoretical simulation indicates that the temperature rise due to heating by the beams is less than 1 K . The temperature reading of a silicon sensor attached to the sample mount is verified with an in-situ magnetic susceptibility measurement. As shown in Fig. 2, two coils are embedded inside the sapphire sample mount underneath the sample. The larger coil is driven with an ac current and the induced voltage in the smaller coil is measured with a lock-in amplifier. At the transition temperature T_c , a sharp change in the induced voltage is observed.

The measured temperature dependence of the thermal diffusivities along the Cu-O plane and the c-axis of an 87 K phase of $Bi_2Sr_2CaCu_2O_8$ is shown in Fig. 3 . The superconducting transition appears in the ab-plane diffusivity as a large change in the slope with temperature.[1] Very little change in the diffusivity along the c-axis is observed, and the diffusivity in this direction is much

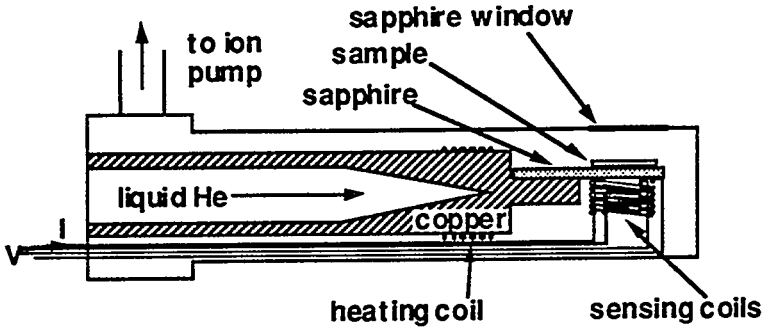

Fig. 2. Schematic of the cryostat used in the measurement. Two coils are placed underneath the sample inside the sapphire mount to conduct an in-situ susceptibility measurement of the sample to calibrate the temperature reading of a silicon diode.

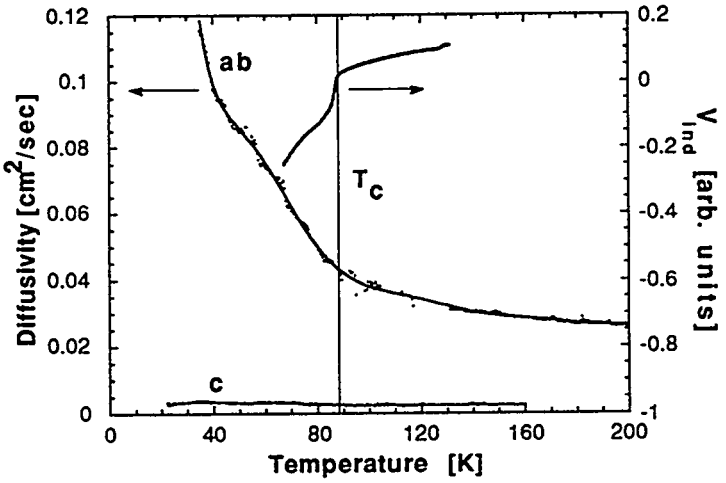

Fig. 3. Thermal diffusivity measurements of single-crystal $Bi_2Sr_2CaCu_2O_8$ along the Cu-O plane and the c-axis. The heavy line shows the in-situ measurement of the induced voltage in the pick-up coil underneath the 87 K crystal. The sharp transition in the induced voltage indicates the superconducting transition.

smaller than along the a-b plane. These are the first direct measurements of diffusivity rather than thermal conductivity in these materials. Such measurements are convenient as a check on the theory, since they are not dominated, as the thermal conductivity measurements are, by the rapid decrease of heat capacity below T_c. The increase in the thermal diffusivity below T_c is caused by a drop in electron-phonon scattering as the electrical carriers condense into superconducting pairs, since estimates based on electrical resistivity measurements and the Wiedemann-Franz Law indicate that the major part of the heat flow is transmitted by the lattice. Therefore, the loss of the electronic component of diffusivity below T_c more than offsets the bulk diffusivity and contributes substantially to the increase in the phonon mean-free path. Further discussion of these results is given by Wu et al.[1]

Another set of measurements of the diffusion as a function of temperature in $YBa_2Cu_3O_{7-\delta}$ is shown in Fig. 4. A major advantage of measuring within a small volume is demonstrated by these results, where the diffusivity measurements were conducted for a 10 μm spacing between the excitation and the probe areas in a single YBCO domain, and across the twin boundary. For comparison, the diffusivity measurements for thin YBCO films using another optical technique, the transient grating method, in a region 200 μm across, are also shown. It will be seen that, above the transition

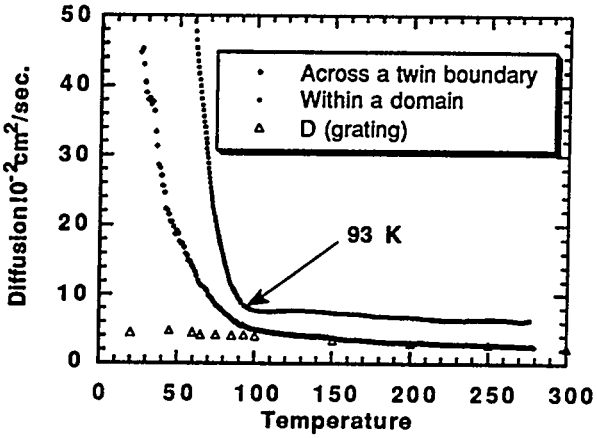

Fig. 4. Measured diffusion in $YBa_2Cu_3O_{7-\delta}$.

temperature, the thermal diffusivity decreases slowly with temperature. The diffusivity measured over large-area thin film samples (200 μm across), and across a grain boundary, agree with bulk measurements, but the diffusivity measured within a grain is approximately twice as large as the measured value across a grain boundary. This result indicates that there must be a large change in temperature across the grain boundary, and tends to indicate that phonons (presumably optical phonons) and normal electrons (which contribute to diffusion) are reflected at the grain boundary.[2] Further measurements with variable spacing between the two beams confirm this hypothesis.

Below T_c, the data for different samples differs dramatically. For the single domain for $T < T_c$, diffusivity increases sharply over two orders of magnitude. This diffusivity enhancement can be explained only by removal of free carriers from the conducting state into the superconducting condensate. For samples of lower quality, the enhancement is less sharp, especially for the thin film sample where the superconducting transition has almost no effect upon the diffusivity. The measurement through the twin boundary is intermediate between the other two curves. The twin boundary, though thin compared to the beam spacing, creates significant additional resistance for heat transfer. The diffusivity enhancement is evidence of the phonon mechanism of heat transfer inside a single domain. In thin films, scattering by point defects independent of the free carrier density probably dominate. We have shown[2] that the experimental results indicate that the scattering rate of phonons is proportional to the number density of normal electrons at temperatures below T_c. Furthermore, the number density of normal electrons varies with temperature, much like the predictions of BCS theory, although there are considerable experiment-theory differences near T_c.

Figures 5 and 6 show raw data for the measured dR/dT of a $YBa_2Cu_3O_{7-\delta}$ and $Bi_2Sr_2CaCu_2O_8$ crystals, respectively. Both figures clearly indicate a sharp divergence of the amplitude of the photothermal signal at the superconducting transition above a slowly-varying background amplitude, as indicated by the accompanying inductive measurements.

The optical method described below has the advantage that it measures a volume small enough, typically much smaller than a single crystallite, to avoid gross inhomogeneities. Following our analysis of the nature of the divergence, we conclude that for $YBa_2Cu_3O_7$, Gaussian fluctuations are observable for a temperature range as wide as ± 35 K around T_c, while close to the transition critical fluctuations are observed. The critical region is established to be of the order of $(T - T_c)/T_c \sim 0.05$, in good agreement with other published data. For $Bi_2Sr_2CaCu_2O_8$, the result is more consistent with quasi two-dimensional behavior, similar to that in thin superconducting films.

Using Ginzburg-Landau theory, with Gaussian fluctuations as the first correction, we expect the excess specific heat to diverge as $C_{\pm}[(T - T_c)/T_c]^{-\alpha}$, where $\alpha = (4-d)/2$, the + and - signs denote above and below the transition, respectively, and d is the dimensionality of the interaction.

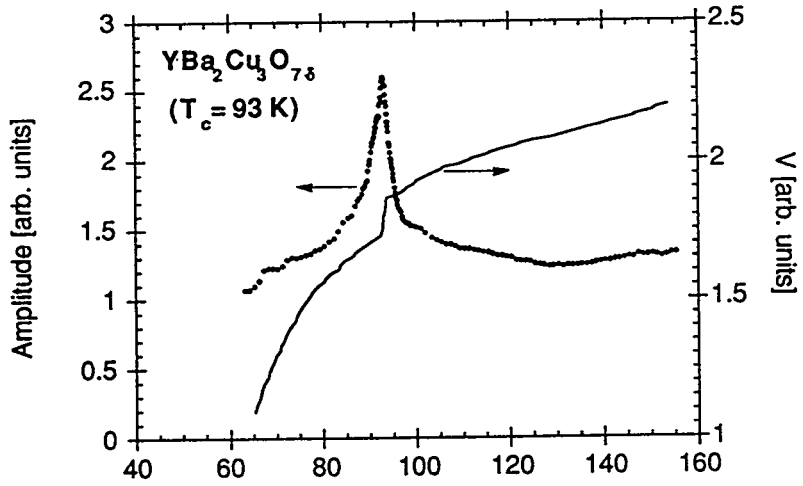

Fig. 5. Amplitude response of the photothermal signal measured on a 93 K phase single-crystal $YBa_2Cu_3O_{7-\delta}$ superconductor. The full line is the induced voltage of the ac in-situ susceptibility measurement.

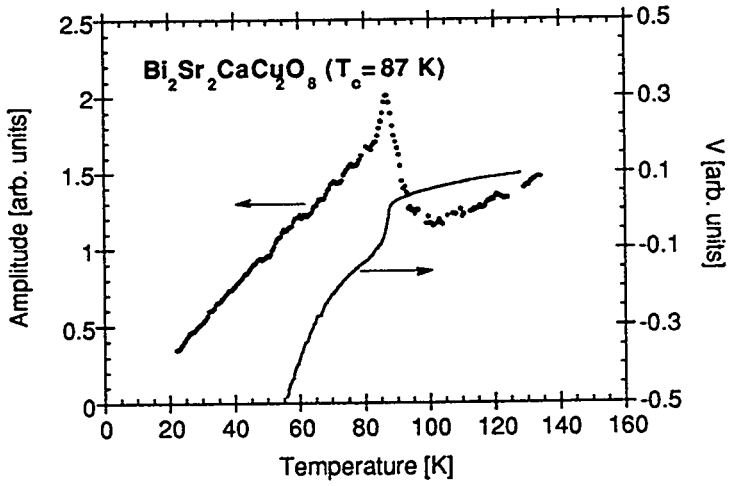

Fig. 6. Amplitude response of the photothermal signal measured on an 87 K single-crystal $Bi_2Sr_2CaCu_2O_8$ superconductor. The full line is the induced voltage of the ac in-situ susceptibility measurement.

The amplitude of the fluctuating specific heat obeys $C_+/C_- = 2^{-d/2}n$, where n is the number of components of the order parameter.

We have argued above that the intensity of the reflected light is proportional to dR/dT, where R is the reflectivity of the sample. In general we can write:

$$\frac{dR}{dT} = \frac{\partial R}{\partial \chi}\frac{d\chi}{dT} + \frac{\partial R}{\partial \sigma}\frac{d\sigma}{dT} \quad ,$$

where $\chi = \chi_n + \chi_s$ and $\sigma = \sigma_n + \sigma_s$, χ and σ are the dielectric response and the electrical conductivity, respectively, and the subscripts n and s, denote normal electrons and superconducting electron pairs, respectively. Assuming that χ_n and σ_n are smooth functions of temperature, we have shown that at optical frequencies the dominant singular term is:

$$\frac{dR}{dT} \propto \frac{d\chi_s}{dT} \propto |(T - T_c)/T_c|^{-\alpha} \quad ,$$

which indicates that dR/dT diverges at the phase transition in the same way as the specific heat.

The above simple analysis is the basis of our understanding of the diverging part of the photothermal data. However, the amplitude response we measure is not entirely due to fluctuation effects. Note that in both Figs. 5 and 6 there is a well behaved background above T_c which is clearly not associated with superconductivity, resulting from some temperature-dependent material properties in the normal state. Figure 7 shows the amplitude response for YBCO with a linear background, as extrapolated from high temperatures, subtracted from the curve of Fig. 5. The result indicates a very broad temperature range from 45 K below the transition up to 60 K above T_c where fluctuations are detected.

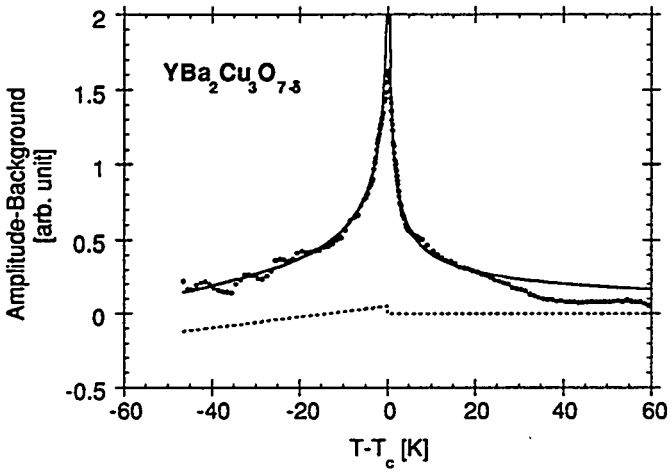

Fig. 7. Amplitude response of photothermal signal measured on a 93 K phase single-crystal $YBa_2Cu_3O_{7-\delta}$ superconductor with a linear background subtracted. The solid lines are power-law fit with C_+/C_- set as 0.7 . The dashed line indicates the mean-field step jump needed for the best fit.

For $YBa_2Cu_3O_{7-\delta}$, with a dimensionality of $d = 3$, fitting the data to the above relation, we find that, as in specific heat measurements, a small background jump ΔC must be subtracted from the total value of C . The solid line in Fig. 6 represents the best fit for $n = 2$, allowing the background to have a different slope below and above T_c . Closer to T_c , the data indicate that a different, weaker, divergence has to be involved. In fact, by using a slowly-varying parabolic background, we can fit the data to a logarithmic function of reduced temperature. The fit is good over a decade in reduced temperature (from 0.005 to 0.05), especially for data above the transition. The crossover to the critical region occurs within about 5 K around T_c, in good agreement with simple estimates based on material properties.[3]

There is a qualitative difference in the raw data between $YBa_2Cu_3O_{7-\delta}$ and $Bi_2Sr_2CaCu_2O_8$ (Figs. 5 and 6). The divergence is weaker for $Bi_2Sr_2CaCu_2O_8$, although the onset is much steeper for this crystal. Since the $Bi_2Sr_2CaCu_2O_8$ system is much more anisotropic, we expect two-dimensional behavior in all of the accessible temperature range near T_c and, in fact, can fit the data away from the peak with a value of $d = 2$ and an amplitude that varies as $1(T - T_c)$ using similar procedures to those already described. An analysis of the data indicates good agreement with theory for the specific heat of Rickayzen et al,[4] which solves the Ginzburg-Landau Hamiltonian for the two-dimensional case. Figure 8 shows the data of Fig. 6, now the normalized amplitude divided by the temperature, is plotted against temperature. The solid line is a good fit to Rickayzen's theory. Note that the data indicates a slightly sharper feature than the theoretical one.

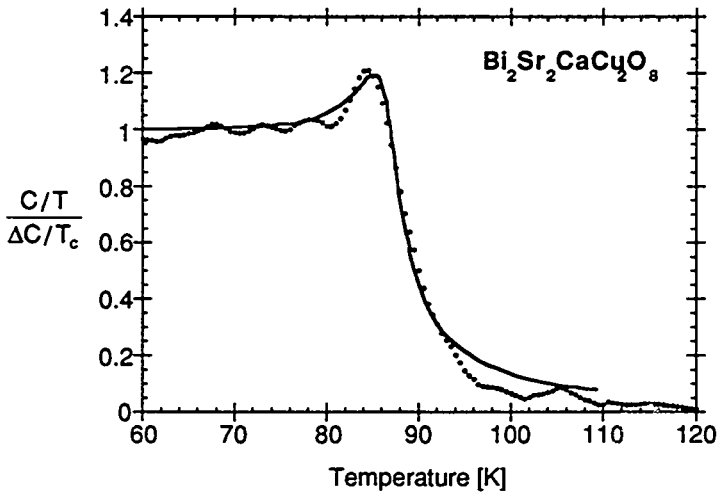

Fig. 8. Amplitude response for $Bi_2Sr_2CaCu_2O_8$ divided by temperature. The solid line indicates a fit to theory for the 2D superconductor (see text).

CONCLUSIONS

We have described a photothermal microscope that can measure anisotropic thermal diffusivity and investigate diffusion and electronic phase transitions of high-temperature superconductors. Since we use focused laser light to excite and detect thermal waves, the technique is completely noncontacting, nondestructive and well suited for small high-T_c samples.

We have made the first measurements of thermal diffusivities along the Cu-O superconducting plane and the c-axis within one domain of single-crystal samples of $Bi_2Sr_2CaCu_2O_8$ and $YBa_2Cu_3O_{7-\delta}$. The ab-plane diffusivity undergoes a sharp increase below the transition, which is evidence of the decoupling of electrons and phonons. A similar effect is not observed along the c-axis. Since thermal diffusivity near T_c is a direct measurement of the electron-phonon scattering process, accurate measurement of thermal diffusivity without the interference of grain boundaries can supply important information about the superconductivity mechanism.

The amplitude of the photothermal signal shows a strong divergence at the superconducting transition. This divergence in the modulated signal above T_c is a direct observation of the thermodynamic fluctuations of the electron density and density correlation. We have shown that the amplitude signal diverges in the same way as the electronic specific heat. We have seen similar effects at the charge density wave phase transition in $NbSe_2$. It is apparent that photothermal microscopy can also be used to observe other electronic phase transition processes with unique sensitivity and selectivity.

This work was supported by the Department of Energy (DOE) under Contract No. DE-FG03-90ER14157.

REFERENCES

1. X. D. Wu, J. G. Fanton, G. S. Kino, S. Ryu, D. B. Mitzi, and A. Kapitulnik, "Thermal Diffusivity of $Bi_2Sr_2CaCu_2O_8$ Single Crystals," Accepted for publication, Physica C.
2. I. M. Fishman, G. S. Kino, and X. D. Wu, "Density of Normal Carriers Below T_c and Thermal Resistance of Twin Boundaries in $YBa_2Cu_3O_{7-\delta}$ Single Crystals," Submitted to Phys. Rev. Letters.
3. A. Kapitulnik, M. R. Beasley, C. Castellani, and C. Di Castro, Phys. Rev. **B 37**, 537 (1988).
4. G. Rickayzen and A. J. Bray, J. Phys. F **3**, L134 (1973).

DIELECTRIC STUDIES OF FLUIDS WITH REENTRANT RESONATORS

A.R.H. Goodwin and M.R. Moldover

Thermophysics Division,
National Institute of Standards and Technology,
Gaithersburg, MD 20899, U.S.A.

ABSTRACT

We have used a reentrant radio-frequency (rf) cavity as a resonator operating near 375 MHz to measure changes in the dielectric constant of fluids within it. The utility of these measurements was demonstrated by determining the dipole moment of 1,1,1,2,3,3-hexafluoropropane, a candidate replacement refrigerant (denoted R236ea) and by detecting the phase boundaries in the mixture $\{(1-x)C_2H_6 + xCO_2\}$, for the mole fraction $x = 0.492$. The densities of the coexisting phases of the mixture were determined using the Clausius-Mossotti relation which has errors on the order of 0.5 % in this application. To test the accuracy of the present techniques, the rf resonator was calibrated with helium and then used to redetermine the molar polarizability A_ε of argon. The results were in excellent agreement with published values. Our design of the reentrant resonator makes it suitable for use with corrosive fluids at temperatures up to 400°C.

1. INTRODUCTION

In the present work, we are extending techniques for measuring the dielectric constants of fluids at radio frequencies (rf). The primary objective is to develop a versatile, reliable, automated method of detecting the density changes associated with the onset of phase transitions in fluid mixtures. Such a method would be an economical alternative to those tedious conventional experimental investigations of dew and bubble curves that rely on visual observation of the first onset of liquid or vapor. Conventional investigations often involve sample volumes on the order of 500 cm^3 and suffer uncertainties arising from "dead" volumes. Sometimes, these apparatus use mercury to vary the volume. If so, they cannot be used at high temperatures. The methods developed here use samples on the order of 60 cm^3 and are applicable to high temperatures.

Capacitors that can be easily filled with various test fluids have a capacitance of no more than a few hundred picofarads in vacuum. Thus, at audio frequencies, they are high-impedance electrical sources (typically 0.1 - 1 MΩ). It follows that the measurement of the dielectric constant at audio frequencies puts great demands on the insulators that are used to maintain the stable mechanical spacing between the conducting plates. Furthermore, even the slight conductivity that results from polar impurities in normally insulating fluids may interfere with the measurements. As the temperature is raised, the conductivity of most fluids increases and the difficulties in measuring the dielectric constant at audio frequencies increases.

At rf and microwave frequencies, the source impedance of capacitors is much lower; therefore, a greater parallel conductivity can be tolerated. Furthermore, as shown below, rf capacitors can be designed that do not have insulators in critical locations. This avoids metal-insulator joints that are often troublesome when they are subjected to stresses from either thermal expansion or applied pressure.

2. REENTRANT CAVITIES

Reentrant rf cavities have been used to accurately measure the dielectric constant and losses of solid insulators [1,2] at frequencies of 50 - 1000 MHz. They have been used by Van Degrift as pressure sensors and he proposed that they be used as thermometers, accelerometers, and liquid-level indicators. [3,4].

In a first approximation, reentrant cavities function as a parallel *LCR* network with a resonant frequency given by

$$2\pi f = (LC)^{-1/2}, \qquad (1)$$

where L is the inductance and C is the capacitance. For a resonator constructed from non-magnetic materials, both L and C are determined by the geometry of the cavity and by the electrical properties of the fluid within it. L is proportional to the relative permeability μ_r of the fluid and C is proportional to the dielectric constant of the fluid ε_r. For almost all fluids, $(\mu_r\text{-}1) << (\varepsilon_r\text{-}1)$; therefore, the changes in f are dominated by the changes in the capacitance. {As an example, we mention difluorodichloromethane at 298 K and 0.1 MPa for which $(\mu_r\text{-}1) \approx 1\times10^{-8}$ [5] and $(\varepsilon_r\text{-}1) \approx 3\times10^{-3}$} Thus, the problem of measuring changes in the dielectric constant is reduced to the easier problem of measuring changes in a resonance frequency.

A cross-section of one reentrant resonator used in this work is shown in Fig. 1. Most of the resonator was comprised of two metal parts. The lower part was a hollow cylinder closed at the bottom. It had an internal radius $b = 25$ mm and a wall thickness of 10 mm. The upper part of the resonator served as a lid to the cylinder and had a bulbous coaxial extension into the cavity. Near its top, the extension to the lid had an outer radius $c = 5$ mm and an effective length $l = 18.5$ mm. The bulbous portion of the extension had an outer radius $a = 24$ mm and a length $M = 20$ mm. The assembled resonator had an internal volume of approximately 60 cm^3.

When the resonator was assembled, an annular gap 1 mm wide separated the bulbous extension of the lid from the inner surface of the cylinder. To a first approximation, we measured the dielectric constant ε_r of the fluid in this gap. The capacitance of the gap was estimated from

$$C \approx \varepsilon_0\, \varepsilon_r\, 2\pi M / \ln(b/a) \approx 27 \text{ pF}, \qquad (2)$$

where ε_0 is the permittivity of vacuum. This estimate for C is approximately 10% too small because it neglects the capacitance of the volume beneath the bulbous extension. The inductor L was formed by the upper part of the cavity and has the approximate value:

$$L \approx \mu_0\, \mu_r\, l \ln(b/c) / (2\pi) \approx 5.96 \text{ nH}, \qquad (3)$$

where μ_0 is the permeability of vacuum.

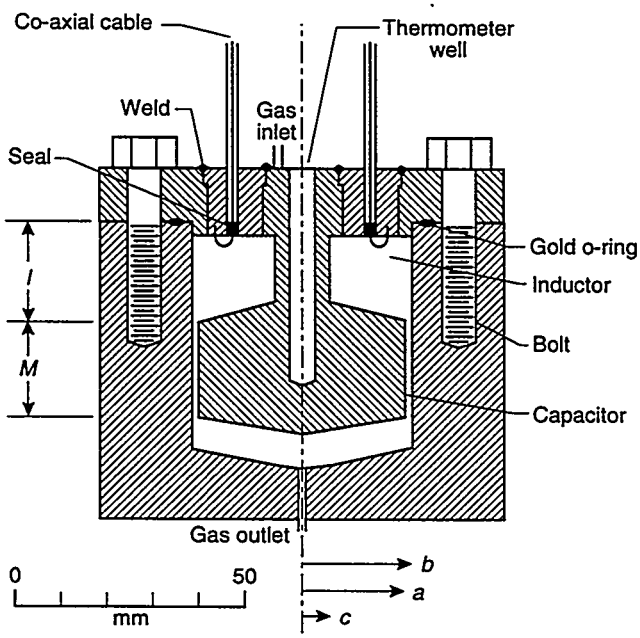

FIGURE 1. Cross-section of the reentrant cavity.

The amplitudes of the rf fields decay exponentially within the metal walls of the resonator. At 375 MHz, the decay length is:

$$\delta = (\pi\, \mu_0\, \mu_r\, \sigma f)^{-1/2} \approx 6.8\ \mu\text{m}, \qquad (4)$$

where μ_r and σ are the magnetic permeability and the conductivity of the wall, respectively. For the brass resonator, we used the electrical resistivity from [6].

The resistance R that appears in series with the inductor and in parallel with the capacitor was estimated from

$$R = \frac{1}{2\pi\delta\sigma}\left\{\frac{l'}{c} + \frac{l''}{b} + 2\ln(c/b)\right\} \approx 12\ \text{m}\Omega. \qquad (5)$$

Here $l' = 17$ mm was the length of the inductor at its inner radius c and $l'' = 40$ mm was the sum of the length of the inductor at its outer radius b and a length M to account for the effective current path in the capacitor.

The resonance frequency predicted by Eq. (1) is 394 MHz; however, it was found to be 375 MHz. This 5% difference is not surprising because the dimensional measurements and the model for the reentrant resonator represented by Eqs. (1) - (5) are very crude in comparison with the precision of the frequency measurements. Furthermore, we expected corrections to C on the order of 5% resulting from fringing fields [$(b - a)/M \approx 0.05$] and comparably sized corrections from the volume below the gap. Corrections to L and C from the rf decay length are on the order δ/(dimensions of the cavity). For the smallest dimension of the capacitor they are $\delta/(b\text{-}a) \approx 7\ \mu$m/1 mm = 0.007. There are also corrections to Eq. (1) on the order of $1/Q^2$, depending on how the resonance is excited and detected.

In the simple model presented here, the quality factor for the brass resonator at 375 MHz is estimated to be:

$$Q = 2\pi f L / R = 1155. \qquad (6)$$

The measured value of Q was only 604. Some of the excess loss was traced to excessive coupling of the rf out of the resonator. The coupling loops in the prototype resonator were approximately semicircles 5 mm in diameter and in a plane through the axis of the resonator. In future work, the coupling will be reduced by rotating the planes of the loops.

Both parts of our first reentrant resonator were machined from a single cylindrical billet of yellow brass (65% copper, 35% zinc). The parts met at an interlocking step. The step ensured accurate concentric alignment of the parts when they were bolted together. The assembled resonator was sealed with a gold O-ring; thus, its outer shell acted as a pressure vessel. The data reported below were obtained this brass resonator. Subsequently, we have manufactured a resonator from Inconel 625 [7] for use at high temperatures.

In the prototype resonator, the two electrical feedthroughs were formed from stainless-steel, PTFE-insulated, coaxial cables that were sealed into the lid with high-pressure conical fittings machined from nylon. In the high temperature version of the resonator shown in Fig. 1, special high-temperature coaxial cables were welded into plugs that were themselves welded into the lid of the resonator. The seals in the high-temperature cables are the *only* insulators in that resonator. Such seals are often used in high vacuum systems which are baked at 450°C. In the rf resonator, the electrical resistance of the seals can be much smaller than the resistance required of spacers used in capacitors at audio frequencies. Furthermore, the dimensional stability of the seals is not critical.

In our prototype work, the resonance frequencies f and quality factors Q were measured with a network analyzer. When the network analyzer excited the resonator at 0 dBm, the signal detected at resonance was -14 dBm. The complex transmission coefficient S_{21} was measured at a series of frequencies near the resonance at 375 MHz and the data were fitted to determine f and Q. Typically, the standard deviation of the fit was fractionally $5\text{x}10^{-8}\text{x}f$, and f and Q were determined with precisions of approximately 10^{-7} and 10^{-4}, respectively. The next higher frequency resonance was a microwave mode near 2.1 GHz; its overlap with the 375 MHz rf mode was negligible.

During future routine applications, we anticipate that the reentrant resonator will be used as the frequency-determining element in an oscillator and that a comparatively inexpensive frequency counter will be used to monitor changes in the fluid's dielectric constant.

3. EXPERIMENTAL PROCEDURES AND MATERIALS

3.1 Gas handling procedures: Measurements on the pure fluids discussed below were obtained along isotherms. To obtain phase boundaries of a fluid mixture under precisely controlled conditions, the following operations were used: (1) The resonator and capillary filling lines were baked at 360 K under vacuum; (2) the homogeneous sample was slowly expanded into the cavity; (3) when the required pressure had been attained the resonator was sealed and its contents remixed until the frequency f and pressure p had been stable to within pre-set limits; (4) the apparatus was cooled to within ≈ 5 K of the known phase envelope, and the isochore commenced; (5) at each of the 0.25 K temperature steps the frequency, temperature, and pressure was measured; (6) after the phase transition had been determined, the cell was returned to a temperature ≈ 20 K above the transition, and the sample was heated asymmetrically to remix it convectively; (7) when the sample was homogeneous, as indicated by f and p, a small quantity of fluid was expanded out of the resonator; and (8) steps 4 through 7 were repeated until data were obtained.

3.2 Additional capacitance measurements: The phase boundaries of the mixture $\{(1\text{-}x)C_2H_6 + xCO_2\}$ (with $x = 0.492$) that were determined with the reentrant resonator were compared with additional capacitance measurements that used a conventional capacitor and a capacitance bridge operating at 1 kHz. The capacitor used for these additional measurements had been constructed by Younglove and Straty [8]. The electrodes were coaxial cylinders held in place by cones at each end and insulated with a 12 μm thick Kapton [7] polymer sheet.

3.3 Thermostat and thermometry: The entire resonator as well as the valve used to seal the test gas within it, were suspended inside a stirred fluid bath that was thermostatted to 1 mK. The temperature of the sample was determined with an industrial-grade stainless-steel-sheathed platinum resistance thermometer and is reported on ITS-90. As indicated in Fig. 1, a blind hole was drilled into the lid of the resonator to accept the thermometer. Resistances were measured with a d.c. digital multimeter operating at a current of 1 mA, with a resolution of 0.1 mΩ and a fractional accuracy of 4.5×10^{-5}. When the current was reversed, no differences were observed in the multimeter reading. The short term accuracy of the multimeter was continually determined by comparison with a standard resistor.

3.4 Pressure measurement: Two pressure gages were used for these measurements. For the dielectric constant measurements, pressures were measured with a fused-quartz bourdon-tube differential pressure gage. The manufacturer's calibration data indicated that the gage had a full scale of 10 MPa and was linear to 1×10^{-5}. However, the zero pressure indication of the gages varied by up to 1 kPa between checks. The reference port of the gage was continuously evacuated by a mechanical vacuum pump and monitored with a thermocouple vacuum gage. For the phase boundary measurements another quartz pressure gage was used. It had a precision of 0.01 kPa and the manufacturer stated that its accuracy was 0.3 kPa. It was mounted in the thermostat fluid with the sensing element in the same plane as the center of the capacitor. When we compared this device to the fused-quartz bourdon-tube differential pressure gage, we found differences of 4.29 kPa at pressures between 0.1 MPa and 6 MPa. When this offset was accounted for, the discrepancies were reduced to less than 0.1 kPa, a level more than adequate for our purpose and well within the manufacturer's quoted accuracy.

3.5 Characterization of gases: The gaseous mixture $(1\text{-}x)C_2H_6 + xCO_2$ with x=0.492 was prepared gravimetrically by Magee [9] and was used by him for specific heat measurements and by Weber [10] for equation-of-state measurements. We used a diaphragm pump to compress this sample from its low-pressure (≈700 kPa) storage containers into a 1000 cm^3 vessel at a pressure greater than 9 MPa. During the compression, the temperature of the gas manifold was maintained at least 20 K above the cricondentherm. After pumping, the mixture was convectively remixed. The carbon dioxide and ethane were both research grade materials supplied by Matheson Gas Products, Inc. [7] with a stated minimum mole fraction purity of 0.99995 and 0.9996, respectively.

The sample used to determine the dipole moment of R236ea was supplied by PCR Inc. [7] which claimed that it had a minimum purity of 0.995 on a mole fraction basis. No information was provided

concerning possible water and air impurities. We analyzed the manufacturer's sample with a gas chromatograph fitted with a thermal conductivity detector and 3 m column packed with Carbopack and 5% Fluorcal [7] as the stationary phase operating at a temperature of 383 K. Four impurities were detected: one was air with a mole fraction of 0.025 and the remaining three were not identified. Presumably they were other halogenated hydrocarbons. The ratio of the area of the unidentified peak to that of the sample was 0.0013. Before use, the sample was degassed by vacuum sublimation and dried over 0.4 nm molecular sieve.

During the course of a set of measurements on each isotherm, aliquots of R236ea were cryo-pumped from the reentrant resonator into an ampoule. The sample recovered from the ampoule at the conclusion of the experiment was analyzed with the same gas chromatographic techniques described above and no air was detected in it.

4. RESULTS AND ANALYSIS

4.1 The empty reentrant resonator: When the prototype reentrant resonator was assembled in ambient air, its quality factor Q was approximately 400. At this stage the surfaces of the cavity had turning marks left from the machining process. The interior surfaces of the resonator were then polished with successively finer grades of emery paper and cutting oil and finally a commercially available brass polish. After polishing, most of the tooling marks had been removed and the Q had increased to approximately 600. We then determined the resonance frequency of the evacuated resonator $f(p=0,T)$ at 13 temperatures between 280 K and 340 K. The results can be represented as a function of the Celsius temperature t by:

$$f(p=0,t) = (374.9679 \pm 0.0004)\ \text{MHz} \times [1 + (19.04 \pm 0.07)\times10^{-6}t - (5.8 \pm 0.9)\times10^{-9}t^2] \qquad (7)$$

The linear coefficient of thermal expansion, 19.04 ± 0.07, was in excellent agreement with a value from the literature [11]. Measurements obtained while increasing and decreasing the temperature differed by less than 2×10^{-6} demonstrating the short-term mechanical stability of the resonator. However, measurements of $f(p=0)$ following application of pressure to the resonator differed from Eq. (7) by as much as 45 ppm (parts per million). Presumably, a steel resonator would have less hysteresis.

4.2 Calibration of the resonator with helium: The capacitance associated with the rf resonance is determined by the small gap in the reentrant resonator; thus, it is particularly sensitive to the dilation of the resonator that occurs when unequal pressures are present inside and outside the resonator. The pressure dependence of the capacitance $C(t,p)$ was determined from measurements of f with helium in the resonator at pressures spanning the range 10 kPa to 300 kPa at 7 temperatures between 280 K and 340 K. For this analysis, we used the dielectric constant of helium from measurements of the temperature and pressure by using the virial equation of state together with the expansion of the molar polarizability P in terms of the density:

$$P = (\varepsilon_r - 1)/[(\varepsilon_r + 2)\rho] = A_\varepsilon + B_\varepsilon\rho + C_\varepsilon\rho^2 \cdots, \qquad (8)$$

We used the value $A_\varepsilon = (0.5196 \pm 0.0002)\ \text{cm}^3\cdot\text{mol}^{-1}$ from [12] and the value $B = 11.59\times10^{-6}\ \text{m}^3/\text{mol}$ from [13] for the second virial coefficient of helium. The results of the calibration were expressed as a calibration factor α:

$$\alpha(t,p) = C(t,0)/C(t,p) = [1 + 5.463\times10^{-10}(p/\text{Pa}) \times (1 + 4.48\times10^{-4}t)]. \qquad (9)$$

For subsequent measurements with other gases, the dielectric constant ε_r was deduced by multiplying the square of the resonance frequency ratio $f^2(t,0)/f^2(t,p)$ by $\alpha(t,p)$. We compared Eq. (9) with a simple model for the resonator that used the elastic constants of brass [14]. The model overestimated the pressure dependence of $\alpha(t,p)$ by 30%.

4.3 **Dielectric constant of argon:** We measured the dielectric constant of argon on 6 isotherms at temperatures between 280 K and 330 K and pressures spanning the range 20 kPa to 280 kPa. For these measurements we used Eq. (9) to account for the resonator's dilation and redetermined $f(T,p=0)$ on each isotherm. Fig. 2(a) shows the dielectric constant of argon as a function of density ρ. As expected, ε_r is a linear function of ρ and independent of temperature. The 52 measurements of ε_r were fitted by Eq. (8) with the result $A_\varepsilon = (4.1350 \pm 0.0004)$ cm$^3 \cdot$mol^{-1}. For the fit, the density was calculated correct to the third virial coefficient with values obtained from [13]. Our results are illustrated in Fig. 2(b) as deviations from this fit. Our value of A_ε is 0.11% smaller than the value (4.1397 ± 0.0006) cm$^3 \cdot$mol^{-1} reported by Bose and Cole [15]. We expect that a more sophisticated model for the resonator will resolve the difference.

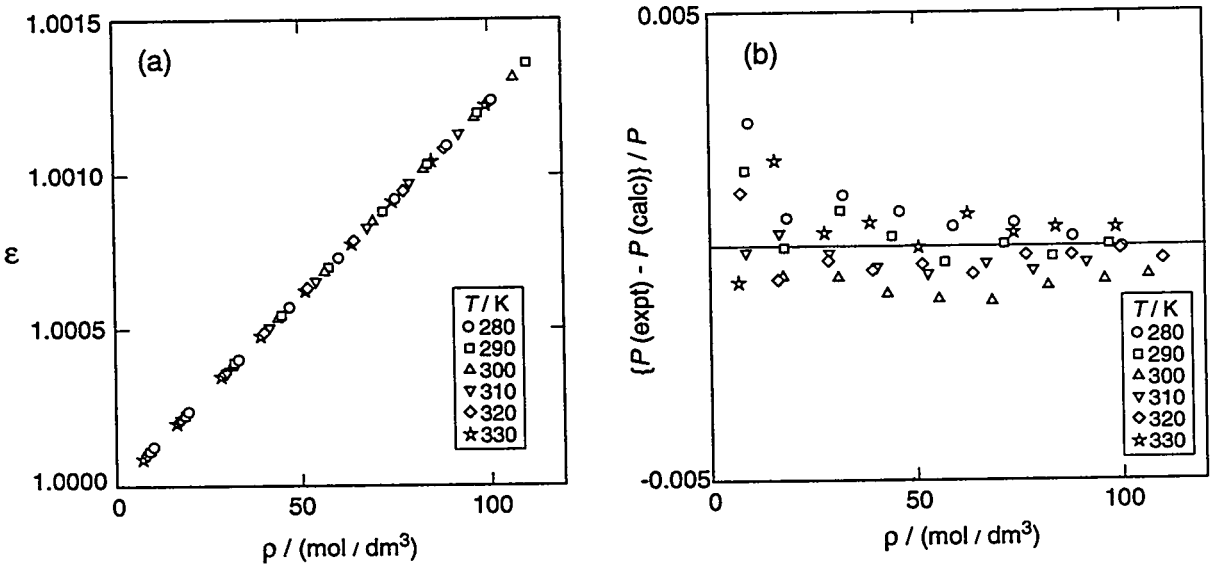

FIGURE 2. (a) Measurements of the dielectric constant ε_r for argon as a function of density ρ. (b) Fractional deviations of the measured total polarizability P from the value 4.135 cm^3/mol.

4.4 **Dielectric constant of R236ea:** The reentrant resonator was used to measure the dielectric constant of R236ea at nine temperatures between 273.2 K and 350 K. The greatest pressures were restricted to 0.6 times the vapor pressure to avoid the effects of precondensation; none was observed. The results are shown in Fig. 3(a). The data for R236ea reveal temperature-dependent ε_r in contrast with the data for argon. Molecules such as R236ea have several conformal isomers with different dipole moments. The populations of the isomers vary with temperature leading to a temperature-dependent dipole moment $\mu(T)$. We deduced $\mu(T)$ from the Debye equation

$$A_\varepsilon = A_\varepsilon(\text{atom.}) + A_\varepsilon(\text{elec.}) + [4\pi N_0/\{9(4\pi\varepsilon_0)k\}]\mu^2(T)/T \quad , \tag{10}$$

where A_ε(atom.) and A_ε(elec.) are the atomic and electronic contributions to the molar polarizability, N_0 is Avogadro's constant, and k is Boltzmann's constant. We obtained the value A_ε(elec.) = 15.9 cm$^3 \cdot$mol^{-1} from measurements of the refractive index n of *liquid* R236ea using methods and an apparatus that has been described in detail elsewhere [16]. The measured refractive index was corrected to zero frequency using the empirical observation [17] that $n(f=0) \approx 0.99n(f)$ to obtain $n = 1.2359$. Then A_ε(elec.) was deduced using the Lorentz-Lorenz relation

$$(n^2 - 1)/(n^2 + 2) = \rho(p,T)A_\varepsilon(\text{elec.}) \tag{11}$$

together with a measurement of the molar density of liquid R236ea reported by others [18]. In the absence of spectroscopic information with which to determine A_ε(atom.), we resorted to the observation

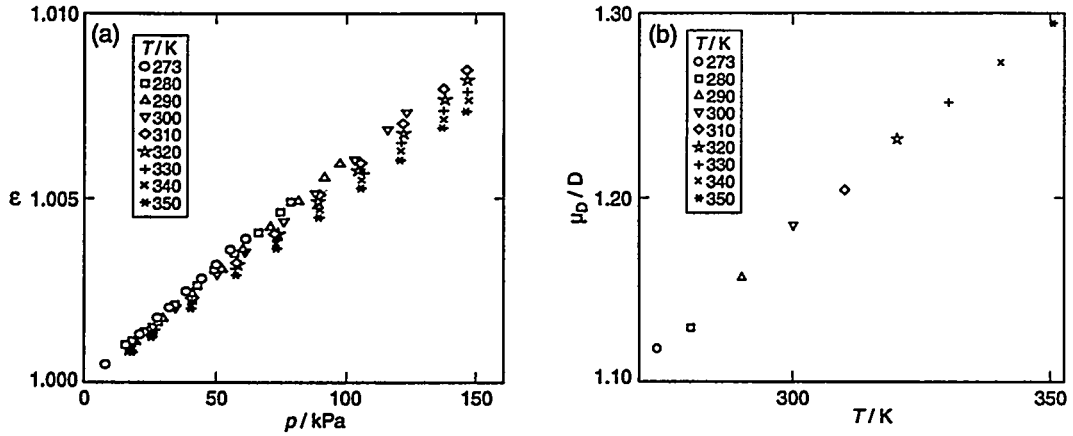

FIGURE 3. (a) Measurements of the dielectric constant ε_r for R236ea as a function of density ρ. (b) Dipole moment μ for R236ea as a function of the temperature T.

that A_e(atom.) ≈ 0.17A_e(elec.) [17]. For R236ea, A_e(atom.) contributes less than 6 % to A_e and a 5 % error in A_e(atom.) would lead to a fractional error in μ of only 0.001 in the worst case. The values of the dipole moment $\mu(T)$ are shown in Fig. 3(b).

The dielectric constants of polar molecules such as R236ea are frequency-dependent. To estimate the scale of this effect, we remeasured the dielectric constant of 2-(difluoromethoxy)-1,1,1-trifluoroethane (E245). At 335.84 K and 33.3 kPa, we obtained the value ε_r = 1.002512 at 377 MHz. This value is 0.000048 smaller than the value ε_r = 1.00256 obtained at 1 kHz under similar conditions [19]. The difference is 2.4 times the uncertainty in the 1 kHz value and has the sign expected of dielectric relaxation. If extremely accurate values of ε_r are required near zero frequency, attention should be paid to dielectric relaxation.

4.5 Phase diagram for the mixture (0.508 C_2H_6 + 0.492 CO_2): To detect the onset of phase separation in mixtures, we confined each sample to the resonator and monitored the resonance frequency as the temperature was reduced. To a good approximation, the density of the sample (and the resonance frequency) did not change until a second phase (either a bubble or a drop) formed. The formation of a second phase was accompanied by flow of some of the parent phase into or out of the capacitor.

Fig 4(a) shows the results for the binary mixture (0.508 CO_2 + 0.492 C_2H_6) when the density was 4.687 mol/dm^3 and when the temperature was in the vicinity of a dew point at which a droplet of liquid formed in the resonator, presumably near its bottom. As the temperature was reduced in steps of 0.25 K, each lasting one hour, the droplet grew and the density of the remainder of the sample, including the sample within the annular capacitor, decreased. The frequency increased as the capacitance decreased. The onset of condensation was determined with a precision of ± 0.06 K. (At the phase transition $df/dT \approx -1$ MHz·K^{-1}, and the fractional precision in each frequency measurement was about 5x10^{-8}.) At precisely the same temperature that df/dT had a discontinuity, the derivative of the half-width of the resonance frequency dg/dT also had a discontinuity. The half-width is a function of the rf decay length δ which itself depends upon the frequency through Eq. (4) and through other effects.

The values of f near a bubble point at a density of 12.508 mol·dm^3 are shown in Fig. 4(b). They provide further evidence for the extraordinary precision with which phase changes can be detected using a reentrant resonator. At this density, $df/dT \approx 1.5$ MHz·K^{-1}.

From our measurements of ε_r and A_e for each component, and assuming $A_e(x)$ is equal to the mole fraction sum, we estimated the density ρ of the fluid within the capacitor. We used the coaxial

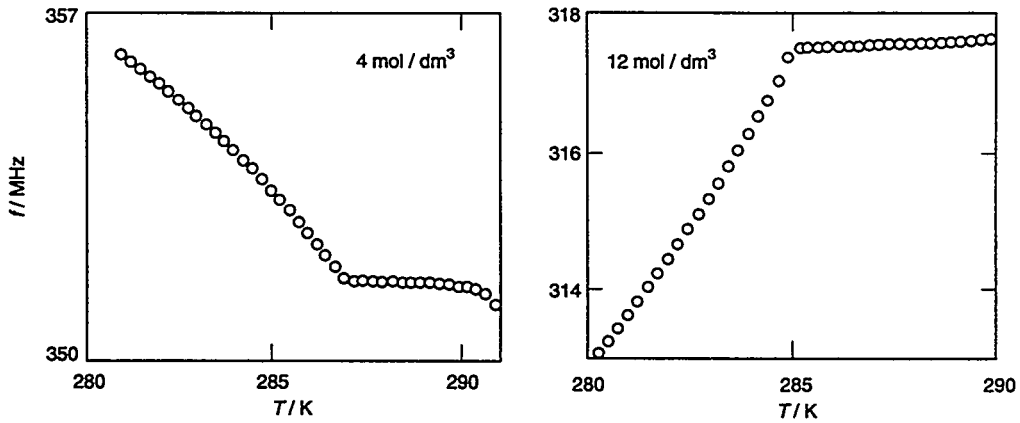

FIGURE 4. Frequency of the reentrant resonator filled with the mixture (0.508 C_2H_6 + 0.492 CO_2). Left: dew point on the isochore $\rho = 4.687$ mol·dm^{-3} where $T^d = (286.98 \pm 0.06)$ K and $p^d = (5110 \pm 8)$ kPa. Right: bubble point on the isochore $\rho = 12.51$ mol·dm^{-3} where $T^b = (285.15 \pm 0.06)$ K and $p^b = (5025 \pm 15)$ kPa.

capacitor [8] and 1 kHz bridge to determine $A_e(CO_2, 1.45$ MPa, 293.1 K) = 7344 cm^3·mol^{-1} and $A_e(C_2H_6, 2.77$ MPa, 293.1 K) = 11150 cm^3·mol^{-1}. Based on the vapor-liquid equilibria and dielectric constant measurements for helium and carbon dioxide systems of Burfield, *et al.* [20], we conclude that our values of ρ have an accuracy of approximately 0.5 %.

In Fig. 5(a) we show the experimental values of the pressure $p(T)$ at the onset of phase separation for this mixture. We have included our results obtained with the reentrant resonator and those obtained with the 1 kHz coaxial capacitor, together with those reported by Weber from conventional equation-of-state measurements [10]. Also shown are two correlations of other experimental information independent of ours based on Leung-Griffiths-type equations of state [21,22]. The level of agreement is quite remarkable. The density values are illustrated in a $\rho(T)$ projection in Fig. 5(b), along with values calculated from references [21] and [22]. Again, the agreement is very good. It demonstrates the utility of the present method as well as the accuracy of the assumption that $A_e(x)$ for this mixture is equal to the mole fraction sum.

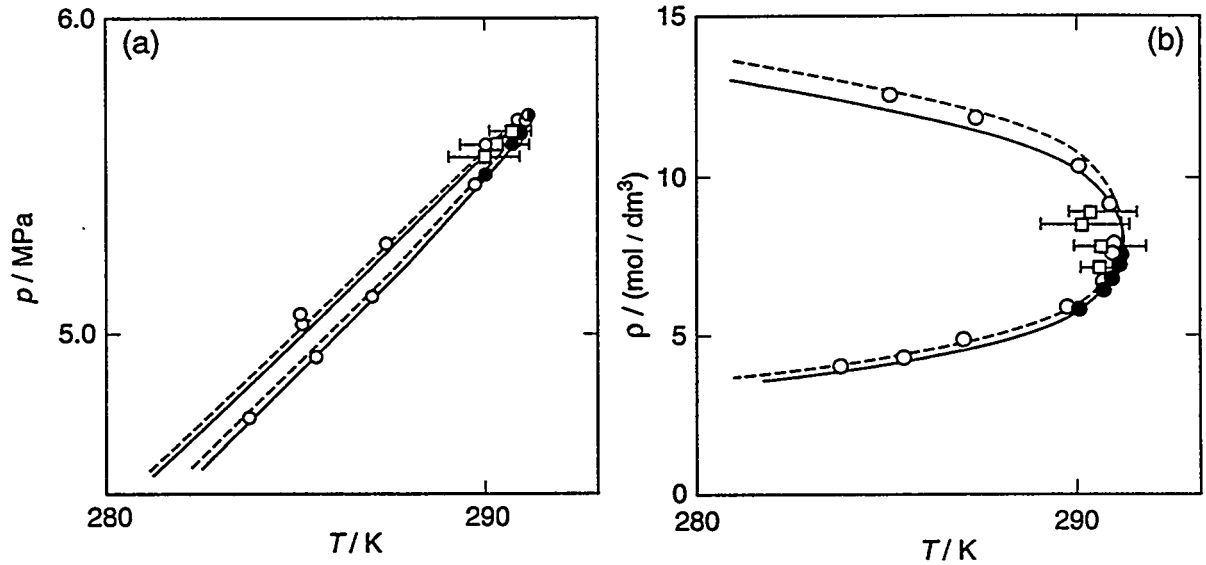

FIGURE 5. Phase borders for the mixture (0.508 C_2H_6 + 0.492 CO_2). o, This work, reentrant resonator; •, this work, concentric cylinder capacitor; □, equation-of-state measurements from [10]; ——, correlation of literature data [21]; – – –, correlation of literature data [22].

ACKNOWLEDGEMENT

This research was supported in part by the Division of Engineering and Geosciences, Office of Basic Energy Sciences, U.S. Department of Energy, under Contract DE-AI05-88ER13823.

REFERENCES

[1] C.N. WORKS, T.W. DAKIN and F.W. BOGGS, *A Resonant-Cavity Method for Measuring Dielectric Properties at Ultra-High Frequencies, Proc. I.R.E.* 33, 245 (1945).

[2] A.H. SCOTT, *Precision Measurements of Dielectric Constant Over a Wide Range of Frequencies and Temperatures, Proc. I.S.A.* 11, 2 (1956).

[3] C.T. VAN DEGRIFT, *A Sensitive Displacement Transducer Using an Extremely Reentrant 84 MHz Cavity Oscillator, Rev. Sci. Instrum.* 45, 1171 (1974).

[4] C.T. VAN DEGRIFT, *Ultra-Stable LC Oscillators and Their Applications in Metrology, Proc. 31st Symp. Freq. Control.* Atlantic City, N.J. (1977), p. 375.

[5] *Handbook of Chemistry and Physics, 54th Edition.* WEAST, R.C.:Editor, CRC Press, Cleveland, Ohio (1973), p. E127.

[6] A.F. CLARK, G.E. CHILDS and G.H. WALLACE, *Low-Temperature Electrical Resistivity of Some Engineering Alloys, Advances in Cryogenic Engineering, Vol. 15.* Timmerhaus, K.D.: Editor, Plenum Press, New York. (1970), p.85.

[7] In order to describe materials and experimental procedures adequately, it is occasionally necessary to identify commercial products by manufacturer's name or label. In no instance does such identification imply endorsement by the National Institute of Standards and Technology, nor does it imply that the particular product or equipment is necessarily the best available for the purpose.

[8] B.A. YOUNGLOVE and G.C. STRATY, *A Capacitor for Accurate Wide Range Dielectric Constant Measurements on Compressed Fluids, Rev. Sci. Instrum.* 41, 1087 (1970).

[9] J. MAGEE, to be published.

[10] L.A. WEBER, *Measurements of the Virial Coefficients and Equation of State of the Carbon Dioxide + Ethane System in the Supercritical Region, Int. J. Thermophysics* 13, 1011 (1992).

[11] R.J. CORRUCCINI and J.J. GNIEWEK, *Thermal Expansion of Technical Solids at Low Temperatures.* U.S. Natl. Bur. Stand. Monograph 29 (1961).

[12] J. HUOT and T.K. BOSE, *Experimental Determination of the Dielectric Virial Coefficients of Atomic Gases as a Function of Temperature, J. Chem. Phys.* 95, 2683 (1991).

[13] J.H. DYMOND and E.B. SMITH, *The Virial Coefficients of Pure Gases and Mixtures.* Clarendon Press, Oxford (1980).

[14] H.M. LEDBETTER, *Temperature Behavior of Young's Moduli of Forty Engineering Alloys, Cryogenics* 22, 653 (1982).

[15] T.K. BOSE and R.H. COLE, *Dielectric and Pressure Virial Coefficients of Imperfect Gases. II. CO_2-Argon Mixtures, J. Chem. Phys.* 52, 140 (1970).

[16] H.B. CHAE, J.W. SCHMIDT and M.R. MOLDOVER, *Alternative Refrigerants R123a, R134, R141b, R142b and R152a: Critical Temperature, Refractive Index, Surface Tension, and Estimates of Liquid, Vapor, and Critical Densities, J. Phys. Chem.* **94**, 8840 (1990).

[17] C.W. MEYER and G. MORRISON, *Dipole Moments of Seven Refrigerants, J. Chem. Eng. Data* **36**, 409 (1991).

[18] D.R. DEFIBAUGH, to be published.

[19] A.R.H. GOODWIN and G. MORRISON, *Measurement of the Dipole Moment of Gaseous 1,1,1-Trichlorotrifluoroethane, 1,2-Difluoroethane, 1,1,2-Trichlorotrifluoroethane and 2-(Difluoromethoxy)-1,1,1-trifluoroethane, J. Phys. Chem.* **96**, 5521 (1992).

[20] D.W. BURFIELD, H.P. RICHARDSON and R.A. GUERECA, *Vapor-Liquid Equilibria and Dielectric Constants for the Helium-Carbon Dioxide System, A.I.Ch.E. J.* **16**, 97 (1970).

[21] J.C. RAINWATER, *Vapor-Liquid Equilibrium and the Modified Leung-Griffiths Model, in Supercritical Fluid Technology: Reviews in Modern Theory and Applications*, T.J. Bruno and J.F. Ely, Editors: CRC Press, Boca Raton, Fl, U.S.A. Chapter 2, (1991), p. 57.

[22] G.X. JIN, S. TANG and J.V. SENGERS, *Thermodynamic Behavior of Fluid Mixtures in the Critical Region, Fluid Phase Equilibria*, **75**, 1 (1992).